Topics in the measurement of the electrons with the ATLAS detector at the LHC.

A Dissertation Presented

by

Moustapha Thioye

to

The Graduate School

in Partial Fulfillment of the

Requirements

for the Degree of

Doctor of Philosophy

in

Physics

Stony Brook University

May 2008

Stony Brook University

The Graduate School

Moustapha Thioye

We, the dissertation committee for the above candidate for the **Doctor of Philosophy** degree, hereby recommend acceptance of this dissertation.

Professor Michael Rijssenbeek, Thesis Advisor
Department of Physics

Professor John Hobbs, Chairman of the defense committee
Department of Physics

Professor John Smith
C. N. Yang Institute of Theoretical Physics

Professor Abhay Deshpande
Department of Physics

Dr. Isabelle Wingerter-Seez, Outside member
Laboratoire d'Annecy-le-vieux de Physique des Particules/IN2P3
Annecy, France

This dissertation is accepted by the Graduate School.

Lawrence Martin
Dean of the Graduate School

Abstract of the Dissertation

Topics in the measurement of the electrons with the ATLAS detector at the LHC.

by

Moustapha Thioye

Doctor of Philosophy

in

Physics

Stony Brook University

2008

Michael Rijssenbeek

Upon completion in 2008, the Large Hadron Collider (LHC) will accelerate and collide protons with a 14 TeV center-of-mass energy at a designed luminosity of $10^{34}\text{cm}^{-2}\text{s}^{-1}$. The LHC will also be able to accelerate and collide heavy ions (Pb-Pb) at a nucleon-nucleon center of mass of 5.5 TeV. It will be the most powerful instrument ever built to investigate particles properties.

The ATLAS (A Toroidal LHC ApparatuS) experiment is one of five experiments at the LHC. ATLAS is a general-purpose detector designed for the discovery of new particles predicted by the Standard Model (i.e Higgs boson), and of signatures of physics beyond the Standard Model (i.e supersymmetry). These discoveries require a highly efficient detection and high-resolution measurement of leptons or photons in the final state. In ATLAS, the liquid Argon (LAr) calorimeters identify and measure electrons and photons with high resolution. This dissertation reports on a study of various topics relevant to the measurement of electrons and photons with the LAr calorimeters.

We report on the design, construction, and testing of the High Voltage Feedthroughs (HVFTs). The HVFTs carry high-voltage lines to the calorimeter cells in the liquid argon, while maintaining the electrical and cryogenic integrity of the system. Seven HVFTs, including one spare, designed and built at Stony Brook are installed on the ATLAS calorimeters at CERN. It is shown that the inaccessible parts of the HVFTs are expected to operate without failures in excess of 20 years.

We also report on the description and simulation of the inactive material installed in the transition region between the barrel and the two end-cap cryostats of the LAr calorimeters. It is known that a detailed knowledge of the upstream material is required to properly calibrate the calorimeter energy measurement with electrons from well-known resonances. Simulations show that the amount of materials in the transition region is consistent with the early estimates used in the Calorimeter Performance Technical Design Report and therefore does not impact the e/γ energy resolution beyond what was predicted.

Finally we report on results of photon runs from the 2004 Combined Test Beam (CTB) and compare this data to photon simulations done with the ATLAS software.

To all the women in my life.
To my grandmothers, my mom and my aunts.
To Poupette Diagne, Baye Khaly, and Michael Salif.

Contents

List of Figures

List of Tables

Acknowledgements

I wish to thank my research advisor, Michael Rijssenbeek, for his decisive contributions to this project. Working alongside him has been a pleasure and a privilege. Many others have helped me on the project, both at Stony Brook and at CERN. I would like to mention all the senior members of the High-Energy Physics group: Rod Engelmann, Bob McCarthy, John Hobbs and Paul Grannis, for their encouragement and continuous support. Dean Schamberger deserves special mention for his extraordinary patience in helping me solve my many computer problems!

Joan Napolitano and Alice Dugan were instrumental in my "success". Moving to CERN came with impressive logistics problems that could not have been solved if it weren't for Joan and Alice. Special thanks to Jack Steffens, Kim-Kwee Ng, Peter Stephens, Pat Peiliker, Elaine Larsen, Maria Hofer, and every one else in the main office for their support over the years.

I moved to CERN in 2005 and had the pleasure to meet and work with many wonderful people. Joe Boudreau and Vakhtang Tsulaia have taught me everything I know about detector description and simulation. I had the fortuity to meet a talented team of physicists at the Laboratoire de Physique des Particules (LAPP) d'Annecy Le Vieux. Among those I would particularly like to thank are Isabelle Wingerter-Seez, Sandrine Laplace, Philippe Ghez, Fabien Tarrade, Mohamed Aharrouche, for the time spent answering my numerous physics and software questions. Ketevi Adikle Assamagan, Marco Delmastro, Andrea Disimone, Karina Loureiro, and Alex Harvey have provided much needed help with the ATLAS software as well. The last chapter of this thesis could not have been completed without Efstathios Paganis' vital contribution.

I am particularly grateful to my family for their support and encouragement. I have a really huge family! I am from Africa after all and for us family extends far beyond one's immediate relatives and includes close friends. Many of those are no longer with us. Among them I shall never forget Mame Awa Sylla, Mame Rose Jouga, Mame Mousso Gaye, Mame Thierno Sylla, Badiene Mame Yacine Thioye, Vieux Thioye, and Mariolein Rijssenbeek.

I certainly could not have made it this far without my grandmother, Fatou

Woury Diop; my mother, Ndeye Sira Gueye; my aunts, Laurence Gueye, Tante Khoudia Gueye, and Ndeye Woury Ba; and my uncle, Babacar Salif Gueye. They nurtured my love for books and of learning very early in my life and have never stopped encouraging me.

I am indebted to my wife, Fatoumata Diagne, for her love and patience over the years, and to Baye Khaly, for his love and wonderful laughter. I would also like to thank Khaly Djibril Diagne and Ndeye Khady Ndoye, for their constant love and support. Ndeye Gueye, Mame Mbodj Fall and Bineta Ndong deserve special mention for their support during my high school years.

I arrived in the US in 1993 with the hopes of achieving my dream of a higher education, but without a penny! I had no idea the ride was going to be this long. It has included stints as painter, driver, housekeeper, gardener, NYC taxi driver, waiter, and sales clerk. I have been lucky throughout all those years to have known Linda C. Davis; her husband, Tommy; and her children: Sheri, Tom, Charlie, Fred, and Ken. Linda has been my biggest fan and supporter. She took upon herself the impossible task of cheering me up and giving me hope whenever my spirits were down. Thank you Linda!

I would like thank my friends and teachers Sam and Sylvia Kaplan, John Kronholm, Parke Kunkle, Richard Pontinen, Jerry Artz, and Judy Snoke. I am grateful to have so many other wonderful friends. I would like to especially thank Elisabeth Diop and Makhtar Dione, Adja Ba and Prince Ngom, Daniel Ndiaye and Fatou “FiFi” Fall, Bacre Waly Ndiaye and Fatima Ndoye, Seynabou Thioye, Almamy Sane and Marietou Diop, Luke Marcon and family, Abdesselam Abdelouahab, Rob and Joelle Miemietz, who have always been there for me.

Before moving to CERN, I spent four great years at Stony Brook where I made what feels to me like lifelong friendships. I only have wonderful memories of the time spent with AKM Shah Newaz, Jerry Sell, Makhsiul Khan and Fahmina Islam, Radu lonas and Flaminia Talos (who gave me much needed refuge and took great care of me the past few months); Diyar Talbayev and Edwige Tamalet; Daniel Yohannes and Rama Calaga to name a few.

I cannot close this chapter of my life without mentioning my friends at CERN. I am grateful to count, Ketevi, Adam and Katie Yurkewicz, Katy Tschann-Grimm, Christine Rijssenbeek, Nino Kaldani, Jet Goodson, Rossela Romita, and Sara Diglio as my friends. Thank you all for the lovely memories.

Finally, I think I am the first in my family to have earned a PhD in any subject, but I sure won’t be the last one. My hope is this degree will serve as an example to African children that anything is possible. So, to Khaly Djibril, Isaiah, Eva Mahe, Aminata Asha, Ndeye Fatou, Nadia, Michael Salif and all the others, the bar has been raised even higher now!

Chapter 1

Introduction

1.1 CERN

Founded in 1954 and currently including 20 Member States, CERN is the European Organization for Nuclear Research, the world's largest particle physics laboratory whose site straddles the Franco-Swiss border (Fig. 1.1).

CERN's scientific and technical staff designs and builds the laboratory's intricate machinery and ensures its smooth operation. It also helps prepare, run, analyze and interpret the complex scientific experiments. In addition to the local staff, some 6500 visiting scientists, half of the world's particle physicists, come to CERN for their research in the world's most advanced physics experiments. They represent 500 universities and over 80 nationalities.

1.2 The LHC

In order to study the elementary constituents of matter and radiation, and the interactions between them, particle physicists need to build machines that can accelerate and collide particles at increasingly higher energies. The Large Hadron Collider (LHC)[1], in construction at CERN near Geneva, Switzerland, will be the most powerful instrument ever built to investigate particles properties. It is mainly a proton-proton collider with a 14 TeV center of mass energy and a design luminosity of $10^{34}\text{cm}^{-2}\text{s}^{-1}$ being installed in the 27 km LEP tunnel (Fig. 1.2), but it will also produce heavy ion collisions (Pb-Pb) at a nucleon-nucleon center of mass of 5.5 TeV. The LHC accelerator is scheduled to begin operation in late 2008.

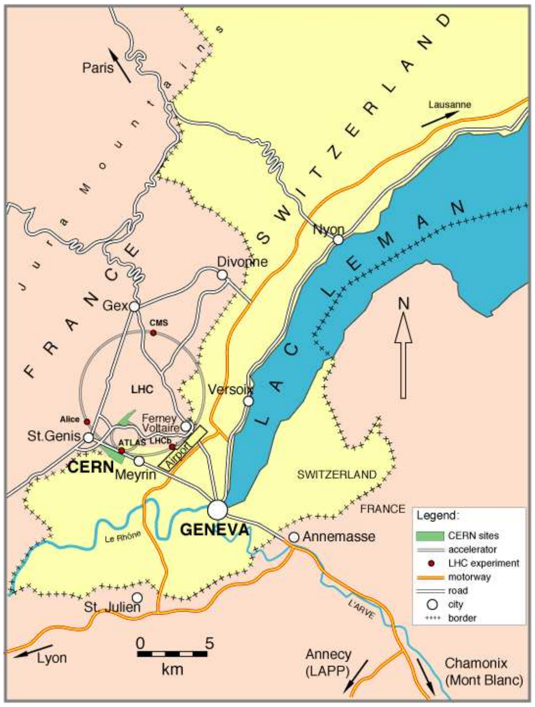

Figure 1.1: Area map of the LHC and the French-Swiss border.

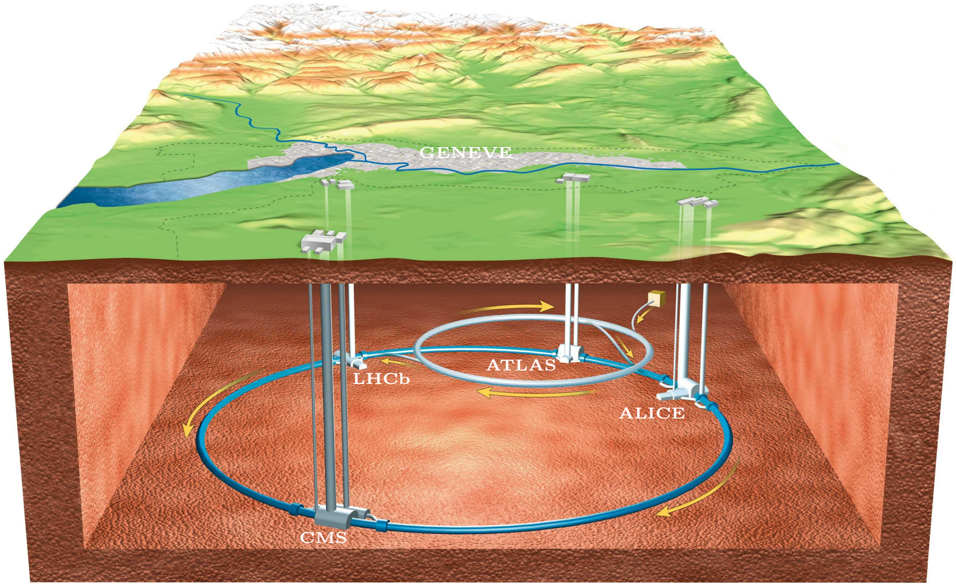

Figure 1.2: Schematic overview of the LHC tunnel, showing the locations of the four main experiments ATLAS, LHCb, CMS, and ALICE.

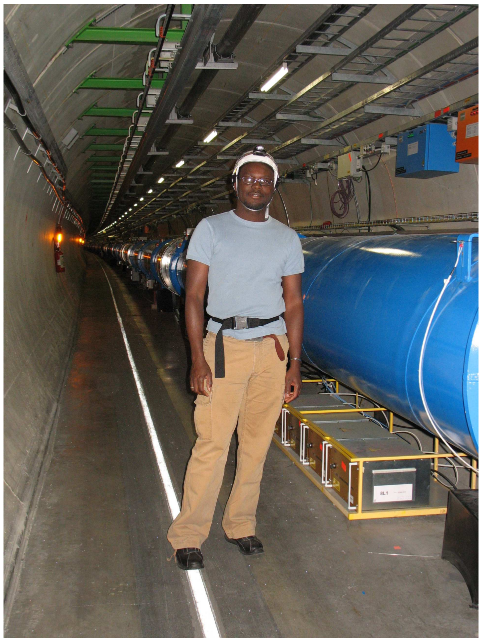

Figure 1.3: LHC dipoles (blue cylindrical tubes) in the tunnel.

1.2.1 Machine Layout and parameters

The LHC ring is made of eight sections. At the center of four of these sections are located the four major experiments currently being constructed. Two of these experiments are located at diametrically opposite high-luminosity insertion points: ATLAS at point 1 and CMS (Compact Muon Solenoid) at point 5. The other two experiments are located at point 2 (ALICE) and point 8 (LHCb). The tunnel houses 1232 super-conducting dipole magnets (Fig. 1.3) that produce the magnetic field of 8.4 T necessary to circulate the beams. In order to achieve such a high magnetic field, the (NbTi) magnets are cooled to less than 2 K with superfluid helium at 1.9 K.

A layout of the LHC injection and acceleration scheme is shown in Fig. 1.4 First an ion source injects protons into an Radio-Frequency (RF) cavity where they are accelerated to 750 keV. These protons are then transmitted to a Linear Accelerator (LINAC) where they attain an energy of 50 MeV before being injected into the 1.4 GeV Proton Synchroton (PS) Booster. The PS accelerates the protons to 25 GeV and deliver a beam of 135 bunches with a 25 ns spacing (7.48 m) and containing 1011 protons each. The Super Proton Synchroton (SPS) takes over and accelerates the protons to 450 GeV before injection into the LHC as 2835 bunches of 10^{11} particles with the same bunch spacing. The two proton beams, which circulate in opposite direction, are

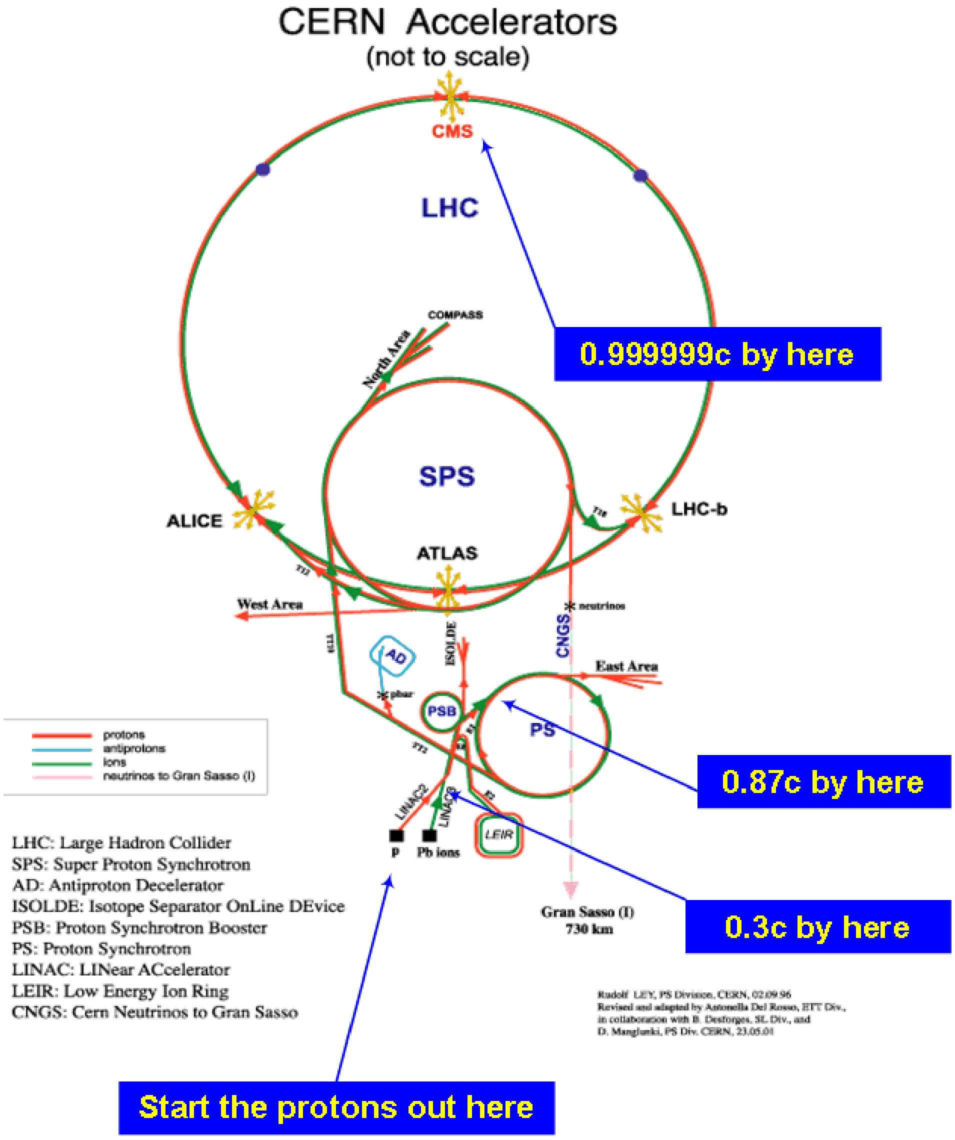

Rudolf LEY, PS Division, CERN, 02.09.96
Revised and adapted by Antonella Del Rosso, ETT Div.,
in collaboration with B. Desforges, SL Div., and
D. Manglunki, PS Div. CERN, 23.05.01

Figure 1.4: The LHC injection and acceleration scheme shows the various stages leading to the production of the very high-energy beam required for the experiments.

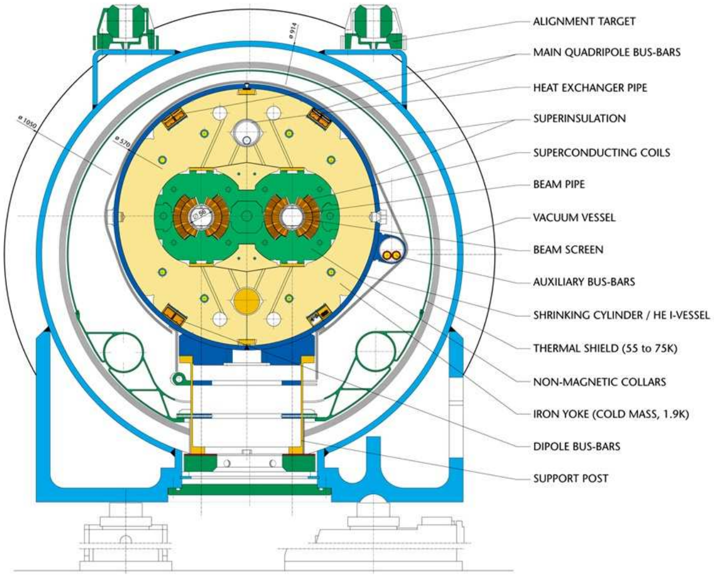

Figure 1.5: Cross-sectional view of an LHC dipole. The two beam pipes are seen in the center, each surrounded by superconducting coils in orange.

combined in a “two-in-one” design whereby the beam pipes along with their corresponding coils are inserted in a single cryostat (Fig. 1.5). Two phases are foreseen for the operation of the LHC. During the first few years of operation (called the low luminosity phase) the nominal luminosity is expected to reach $2 \times 10^{33}\mathrm{cm}^{-2}\mathrm{s}^{-1}$. The luminosity should then increase to its designed nominal value of $10^{34}\mathrm{cm}^{-2}\mathrm{s}^{-1}$ (high luminosity phase).

1.2.2 Physics Goals

A bit of history

The Standard Model of particle physics is a quantum field theory which encapsulates the knowledge of fundamental particles and forces. It identifies structureless, elementary particles that constitute all the observable matter in the universe: These are the quarks and leptons (Fig. 1.6). The SM includes three of the four fundamental interactions: The strong interaction, the weak interaction and the electromagnetic interactions. The interactions between the quarks and leptons are mediated by particles called gauge bosons and photons are the mediators of the electromagnetic interaction.

The Standard Model provides the theoretical framework to calculate physical (measurable) quantities, explain observed phenomena, and make predic-

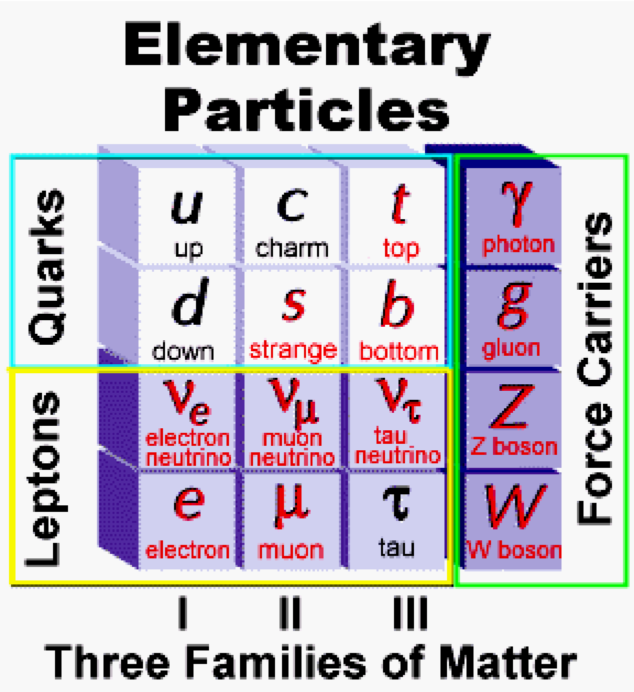

Figure 1.6: Elementary particles families in the Standard Model.

tions that can be checked experimentally. Most of these predictions have been confirmed to spectacular precision at experiments such as LEP at CERN , and the Tevatron at Fermilab. This broad success has made the theoretical framework in which particle physics currently resides.

However, despite its many successes, there is consensus among particle physicists that the Standard Model is not the final theory of particle physics and many extensions to the theory already exist. Several of these extensions, including supersymmetry, have been proposed. Peter Higgs conjectured in 1964 that the massless gauge bosons of weak interactions acquire their mass through interaction with a scalar field (the Higgs Field), resulting in a single massless gauge boson (the photon) and three massive gauge bosons ($W^{\pm}$ and Z^0)[2]. The assumption is that the universe is filled with a spin-zero field, called the Higgs field. The gauge bosons' and fermions' interactions with this field give them their masses. This interaction, in which the particles gain masses, is an example of spontaneous symmetry breaking, in which the SU(2) and U(1) symmetries are broken.

The LHC was built for the potential discovery of new particles such as the Higgs boson (predicted by the Standard Model) and new physics such

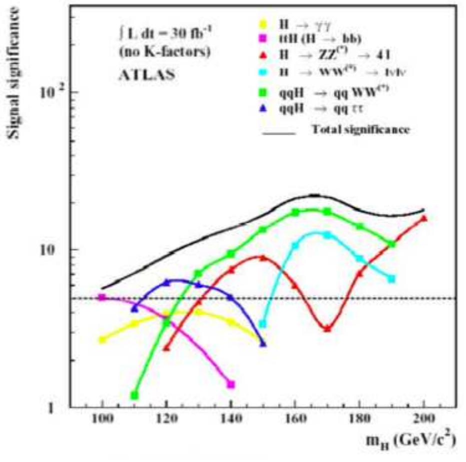

Figure 1.7: Discovery Potential of the SM Higgs boson as function of its mass at low luminosity.

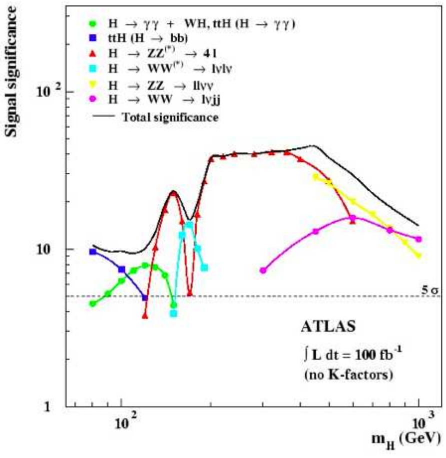

Figure 1.8: Discovery Potential of the SM Higgs boson as function of its mass at high luminosity.

as supersymmetric particles, but also to improve precision measurements of gauge bosons, such as the $W^{\pm}$ bosons, and heavy quarks properties. Therefore, future experiments, in particular at the LHC, will give insight into which, if any, of the proposed theoretical extensions to the Standard Model is correct.

ATLAS Physics

The Discovery potential of the LHC experiments and of ATLAS in particular depends (see Fig. 1.7 and 1.8) entirely on the performance of the detectors. In the case of ATLAS, much discovery hinges on the ability of the calorimeter to make excellent measurements of electrons and photons, including a good energy resolution and a good linearity for energies ranging from a few GeV up to a few TeV. Examples of the importance of the precise measurements of electrons and photons are provided by the potential discovery of a light or intermediate mass Higgs boson:

- **Light Mass Higgs Boson (**115 GeV $< m_H <$ 140 GeV**):**
  If the Higgs is light, the decay $H \rightarrow \gamma\gamma$ is the most promising discovery channel despite it's low branching ratio (10^{-3}). The final state particles consist of two high-P_T photons ($P_T \sim 50$ GeV) with an invariant mass compatible with the Higgs boson mass [3]. The identification of isolated high-P_T photons ($P_T > 25$ GeV) is essential in any Higgs search in this channel. The $H \rightarrow \gamma\gamma$ channel has a simple and clean signature but is

very challenging because of the associated backgrounds. The dominant backgrounds are direct photon production and QCD + γ-*jet* (or *jet-jet*) where one or both of the jets are misidentified as photons. A single *jet* rejection factor of about 3000 is required for the search of SM Higgs decay to two photons. The rejection factor for the separation of γ and π^0 should be better than 3 for $P_T \sim 50.$ GeV The EM calorimeter is optimized to observe the narrow mass peak of the signal above the irreducible $\gamma\gamma$ QCD continuum.

- **Intermediate Mass Higgs Boson** (140 GeV $< m_H \leq 2m_Z \sim$ 180 GeV): If the Higgs has intermediate mass, it's discovery is most promising in the decay channels $H \rightarrow ZZ^* \rightarrow 4$ *leptons*. The reconstruction of final states containing two or four electrons is mainly based on information gleaned from the EM calorimeter. In the case in which the 4 leptons are $e^+e^-e^+e^-$, the energy of one of the electrons can be as low as 10 GeV. This type of measurement is rather demanding on the calorimeter at the lower end of the mass spectrum. In the mass range between 90 GeV and 180 GeV, the calorimeter is required to have a resolution of 1% on the mass of the Higgs decaying into $\gamma\gamma$ or $e^+e^-e^+e^-$.

1.2.3 Experiments and Experimental Challenges

A total of four experiments are currently under construction at the LHC: ATLAS, CMS, ALICE, and LHCb. Two of these, ATLAS and CMS, are general purpose experiments which share similar physics goals but have different design philosophies. The main difference between ATLAS and CMS lies in the design of their respective magnet systems which translates into a radically different geometry of the two detectors. ALICE and LHCb are optimized respectively for heavy ion (Pb-Pb) collisions and B-mesons studies and its related CP-violation. The extreme operating conditions of the LHC impose severe constraints on detectors, in terms of radiation tolerance, background rejection capability, response speed, spatial coverage, time stability and reliability.

At the LHC, a collision involving two bunches of 10^{11} protons will occur every 25 ns. This will give rise to a total of 1000 charged particles in the region $|\eta| < 2.5$[1]. This high particle flux represents an unavoidable source of radiation for the detectors. The ATLAS forward calorimeters will receive a total of about 10^{17} neutrons/cm^2 and a dose of up to 10^7 Gy over a 10-year period, while

---

[1] The direction of a particle coming from the interaction point is usually given by an azimuthal angle ϕ and the pseudo-rapidity η defined as $\eta = -\log\tan(\theta/2)$ where θ is the angle between the beam axis and the particle trajectory.

electromagnetic calorimeter will receive less than 10^{13} neutrons/cm^2 and a dose of about 200 Gy over the same period.

When an interesting high-P_T event takes place, it is usually accompanied by an average of 25 additional simultaneious soft proton-proton interactions (minimum bias events). The detectors parameters have been carefully tuned in terms of background rejection capability, response speed and granularity with the aim of reducing the impact of such contaminations from minimum bias events and pile-up.

Because the energy of interacting partons is not known at hadron colliders, the missing energy of the final state cannot be determined. To compensate for this deficiency, both the measurement of the transverse energy and an efficient reconstruction of jets are required within a good spatial coverage ($|\eta| < 5$).

Finally, because of limitations in storage capabilities and computer processing power, a good trigger system is an absolute necessity for all LHC experiments in order to reduce the interaction rates from 10^9 events/s to about 100 recorded events/s.

ALICE

ALICE (A Large Ion Collider Experiment)[4] is a heavy ion detector designed to investigate Pb-Pb collisions and the properties of quark-gluon plasma. The aim of ALICE is to study strongly interacting matter at high energy densities equivalent to the densities that would have been present in the universe a few seconds after the big bang. ALICE is located at point 2 of the LHC ring. Its Inner Tracker uses Pixel and Silicon Drift Chambers for vertex reconstruction. The Inner Tracker is surrounded by the largest ever built Time Projection Chamber with a drift volume of 100 m^3. Other sub-detectors of ALICE include a Time of Flight (TOF) measurement system, a Ring Imaging Cerenkov (RICH) detector, a dedicated $PbWO_4$ photon spectrometer (PHOS) and a muon arm. ALICE is designed to deal with the highest particle multiplicities anticipated for Pb-Pb reactions ($dN_{ch}/dy = 8000$).

CMS

The Compact Muon Solenoid (CMS)[5] is a multi purpose experiment designed to investigate proton-proton collisions. It is built around a 13 m long high-field solenoid (4T) which surrounds the tracker and calorimeters. Despite its compact design, with a length of 22 m and a height of 15 m, CMS is almost twice as heavy as ATLAS with a weight of 12500 tons. The CMS tracker uses Silicon Pixel detectors in the regions of high occupancy and Silicon Microstrip detectors where the occupancy is low. The hadronic calorimeter of CMS is a sampling calorimeter made of brass absorbers and plastic scintillators while its electromagnetic calorimeter is a homogeneous scintillating crystal calorimeter using very dense $PbWO_4$ crystals. Scintillating light from both types of calorimeters is collected by either avalanche or hybrid photodiodes.

LHCb

The LHC-beauty experiment[6] is designed to study CP violation and other rare phenomena of B mesons decays. Since these mesons will be preferentially produced in the direction of the beam, LHCb is in the form of a single arm. The detector consists of successively a Vertex-Locator based on Silicon Pixel technology located nearer the interaction point, followed by 2 RICH detectors designed for B-flavor tagging and suppression of background events. Between the two RICH detectors are placed a dipole magnet producing a field of 4 T and a tracker which uses both Silicon Microstrip and Straw-Tube Drift Chamber technologies. The electromagnetic calorimeter is made of lead absorbers sandwiched between scintillators and the hadronic calorimeter is made of iron absorbers and plastic scintillators. The muon system is located the furthest from the interaction point. It is composed of Resistive chambers and Multi-Wire proportional Chambers.

ATLAS

The ATLAS (A Toroidal LHC ApparatuS) experiment, presently under construction, is one of five experiments at the LHC. ATLAS is a general-purpose detector with a broad physics program designed for the discovery of new particles predicted by the Standard Model, such as the Higgs boson, and of signatures of physics beyond the Standard Model, such as supersymmetry. With its high-resolution, full-solid-angle-coverage detector, ATLAS will provide improved precision measurements, e.g. of properties of the $W^{\pm}$ bosons and heavy quarks.

Current theoretical wisdom strongly suggests that new physics signals will show up at LHC energies. Most of the predicted signatures contain high-energy leptons or photons in the final state, and therefore a premium is placed on highly efficient detection and high-resolution measurement of these particles. In ATLAS in particular, the liquid Argon (LAr) calorimeters serve to identify and measure electrons and photons with high resolution. This dissertation reports on a study of various topics relevant to the measurement of electrons and photons with the LAr calorimeters.

The first topic concerns the high voltage feedthroughs (HVFT) for the LAr calorimeters. The HVFTs carry high-voltage lines to the calorimeter cells in the liquid, while maintaining the electrical and cryogenic integrity of the system. The design specifications, construction, and testing of the HVFT ports and filters for the LAr calorimeters are described. Seven HVFTs, including one spare, were designed and built at Stony Brook and installed on the ATLAS calorimeters at CERN. It is shown that the inaccessible parts of the HVFTs are expected to operate without failures in excess of 20 years.

Energetic electrons (e) and photons (γ) lose part of their energy in material upstream of the LAr calorimeters, dominantly by bremsstrahlung and photon conversions. A detailed knowledge of the upstream material is required to properly calibrate the calorimeter energy measurement with electrons from well-known resonances. The second topic of this dissertation addresses the inactive material installed in the gap between the barrel and the two end-cap cryostats of the LAr calorimeters. In large part these are the services for the ATLAS Inner Detectors. A detailed accounting of this material in the ATLAS reconstruction software was implemented, making it possible to correct for energy loss of e/γ in this region of the EM calorimeter. Simulations show that the amount of materials in the gap is consistent with the early estimates used in the Calorimeter Performance Technical Design Report and therefore does not impact the e/γ energy resolution beyond what was predicted.

In the last topic of this dissertation we report on results of photon runs from the 2004 Combined Test Beam (CTB) and compare this data to photon simulations done with the ATLAS software.

Chapter 2

ATLAS

The ATLAS (A Toroidal LHC ApparatuS) experiment presently under construction, is one of five experiments at the LHC which will start operation towards the end of 2008. This multi-purpose detector with a wide physics program was specifically designed and optimized for the discovery of new particles predicted by the Standard Model such as the Higgs boson and new physics such as supersymmetric particles, but also to improve precision measurements of gauge bosons, such as the $W^{\pm}$ bosons, and heavy quarks properties. ATLAS has an "onion-layer" structure (Fig. 2.1) composed of independent detector subsystems with the innermost being the inner detector (Pixels, Sillicon Tracker, and Transition Radiation Tracker), followed by the calorimeters (Electromagnetic (EM) and Hadronic) and finally the muon detectors. The ATLAS detector is an incredibly complex experiment described in detail in its Technical Proposal [7], its Technical Design Report [8], and its "As Installed" paper [9]. Physics signatures expected to be extracted with high precision include:

- Reconstruction of charged tracks with transverse momentum measurements at $|\eta| < 2.5$.
- Reconstruction of electromagnetic showers from photons and electrons at $|\eta| < 3.2$, with fine calorimeter segmentation, tracking and particle identification based on transition radiation allowing for separation between electrons, photons, pions and other particles at $|\eta| < 2.5$.
- Identification of muons and measurements of their transverse momentum over a very large momentum range and in presence of high backgrounds ($|\eta| < 2.7$).
- Reconstruction of jets and hadronic particles with energy measurements at $|\eta| < 4.9$, and tagging of b-jets at $|\eta| < 2.5$.

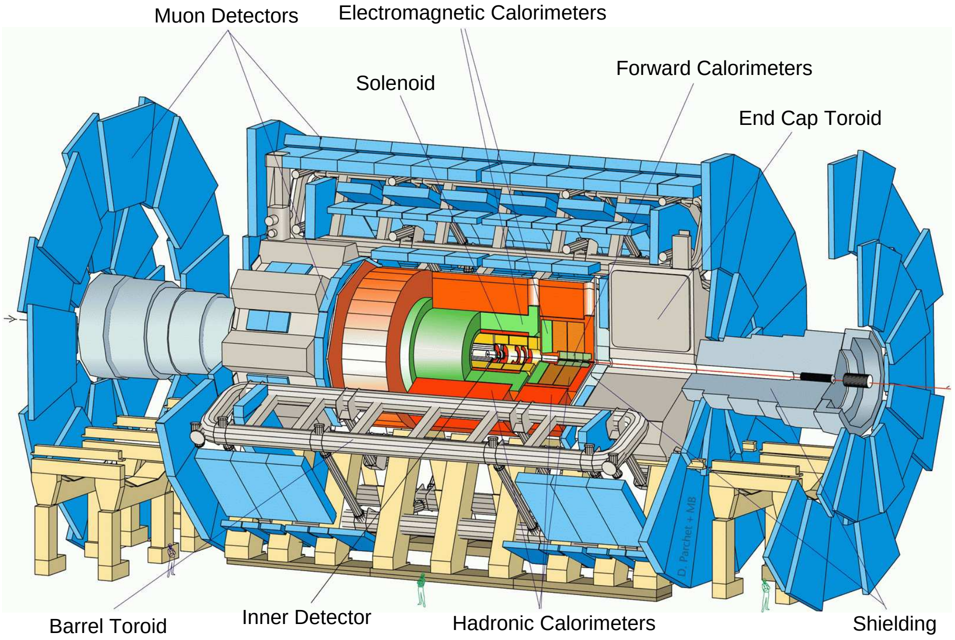

Figure 2.1: The ATLAS detector.

- Identification of hadronic tau decays at $|\eta| < 2.5$.
- Reconstruction of transverse missing energy with complete ϕ acceptance for $|\eta| < 4.9$.

2.1 Inner Detector

The inner Detector (ID) system consists of three different sub-detectors (Fig. 2.2): The Pixel Detector and the Silicon Strip Detector (SCT) both of which use semiconductor tracking technology, and the Transition Radiation Tracker (TRT). The outer radius of the ID cavity is 115 cm and its total length is 7 m. It has a spatial coverage in the range $|\eta| < 2.5$ and is placed within a solenoidal magnetic field of 2T. The ID is the innermost part of ATLAS and is designed to reconstruct the production and decay points (vertices) of charged particles.

SCT detectors are used because they provide the fine granularity and high precision necessary to resolve the vertices and very large track density produced by collisions at the LHC. However, because of cost and material considerations, decision was made to use straw tubes modules in the TRT. The ID is divided into a barrel and two identical end-caps on either side. In the

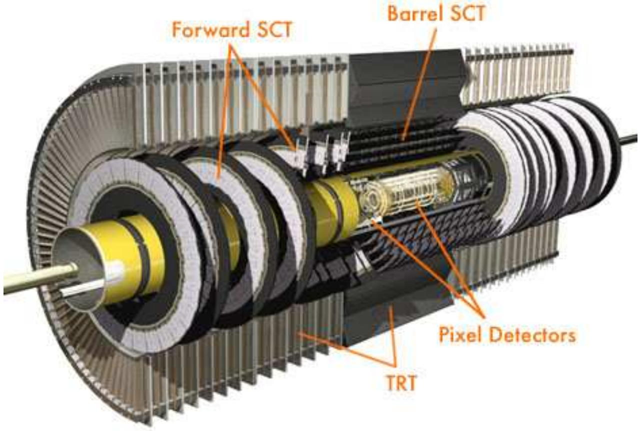

Figure 2.2: 3D view of the ATLAS Inner Detector system.

barrel the SCT layers are arranged in concentric cylinders around the beam axis and the straw tubes are parallel to the beam axis as well. In the end-caps the SCT layers are mounted in disks perpendicular to the beam axis and the TRT straw tubes are mounted radially.

Performance requirements of the ID include [8]:

- Required resolution: $\sigma_{P_T}/P_T = 0.05\% P_T \oplus 1\%$
- Tracking efficiency better than 95% (90%) over the full coverage for isolated tracks with $P_T > 5$ GeV (for tracks in a cone of $\Delta R \leq 0.25$ around isolated tracks), and a fake-track rate $\leq 1\%$ ($\leq 10\%$) of signal rates.
- At least 90% efficiency for reconstructing both primary ($P_T \geq 5$ GeV) and secondary ($P_T \geq 0.5$ GeV) electrons. For primary electrons both bremsstrahlung and trigger efficiency are taken into account.
- Identification of individual particles in dense jets and of electrons and photons that form similar clusters in the EM calorimeter. Combined efficiency of ID and EM calorimeter for photon identification should be $\geq 85\%$.
- Tagging of b-jets by displaced vertex with an efficiency $\geq 40\%$. This is done with a rejection of non b-hadronic jets ≥ 50.
- At low luminosity, efficiency $\geq 50\%$ for tagging b-jets and $\geq 90\%$ for reconstructing K_s^0.

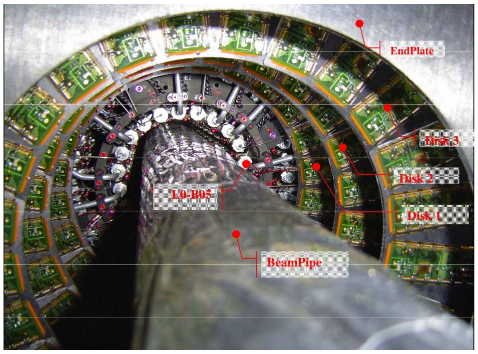

Figure 2.3: Picture of the ATLAS pixel detector showing the three disk stations, the beam pipe and some cooling services.

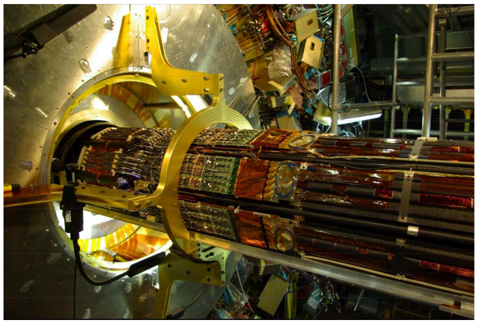

Figure 2.4: The pixel detector pictured during its insertion into ATLAS.

2.1.1 Pixel Detector

The pixel detector, shown in Fig. 2.3 and 2.4, is the closest to the interaction point. It consists of three layers in the barrel and five disks in each end-cap. The required high resolution is provided by 140 millions individual square pixels of 50 μm in rϕ and 400 μm in z. The pixel detector provides at least three measurements over the full acceptance and also determines the impact parameter resolution. A single layer of the pixel detector provides a 2-dimentional coordinate. Due to its location within ATLAS it is built to withstand at least 300 kGy of ionizing radiation and more than 5×10^{14} neutrons/cm^2 over a 10 year period.

2.1.2 Silicon Strip Detector

The silicon strip detector (Fig. 2.5 and 2.6) consists of four layers in the barrel and up to nine wheels in the end-caps. Each layer is made of two single sided detectors placed back to back. Each detector is 6.36×6.40 cm^2 with 768 read out strips of 80 μm pitch. The SCT is thus capable of providing eight precision measurements per track to determine momentum, impact parameter and vertex position. It has a resolution of 16 μm in rϕ and 580 μm in z, and can resolve 2 parallel tracks separated by 200 μm or more.

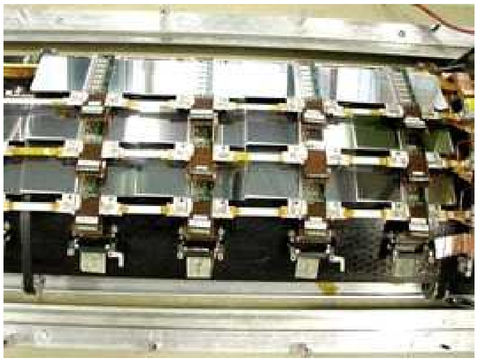

Figure 2.5: Picture of the ATLAS SCT detector showing modules of the SCT barrel.

Figure 2.6: Picture shows an SCT end-cap module with tapered strips.

2.1.3 Transition Radiation Tracker

The TRT constitutes the outermost part of the ID system. It uses straw tubes, which can operate at very high occupancy and counting rates because of their small diameters (4 mm) and the excellent isolation of the 30 μm thick gold covered tungsten wire at the center of each individual gas volume. The straws (Fig. 2.8) are filled with a xenon gas mixture for the detection of transition radiation photons produced in a radiator located between straws. The drift-time measurement gives a spatial resolution of 170 μm per straw as well as a low and a high threshold. Thus, the TRT can discriminate between transition radiation hits that have passed the high threshold, and tracking hits that have passed the low threshold.

2.2 Calorimeters

The ATLAS Calorimeter is divided into an Electromagnetic (EM) Calorimeter and a Hadronic Calorimeter each of which consisting of a barrel and two end-caps. The ATLAS calorimeter consists of an Electromagnetic Barrel Calorimeter (EMB) covering the pseudorapidity $|\eta| < 1.4$, an Electromagnetic End-Cap Calorimeter (EMEC) covering $1.375 < |\eta| < 3.2$, a Hadronic End-Cap Calorimeter (HEC) covering $1.5 < |\eta| < 3.2$, a Forward Calorimeter (FCAL) covering $3.2 < |\eta| < 4.9$, and a Tile Calorimeter (TileCal) covering $|\eta| < 1.7$. The calorimeters are designed to provide a measurement of the energy and position of electrons, photons, isolated hadrons and jets. Because of its good hermeticity, the calorimeter as a whole provides a reliable mea-

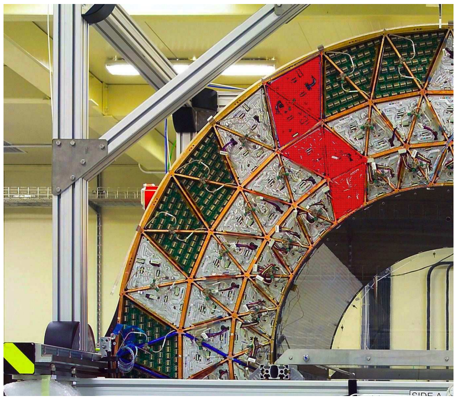

Figure 2.7: Picture shows one quadrant in the $r - \phi$ plane of the TRT with inner, middle, and outer modules in red.

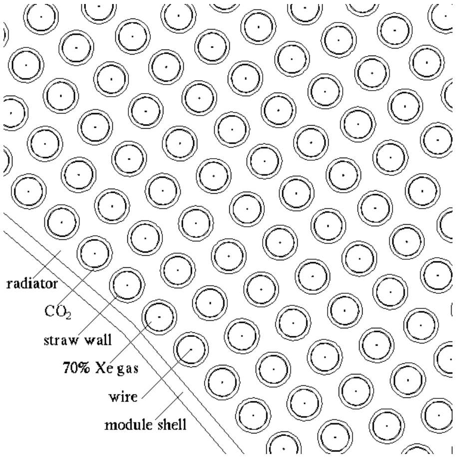

Figure 2.8: Figure provides a close-up view of the TRT straws corresponding to the square inlet (Fig. 2.7) on the left.

surement of the missing transverse energy (E_T^{miss}). Together with the Inner detector, the calorimeter provides a robust particle identification exploiting the fine lateral and good longitudinal segmentation. Figure 2.9 shows a general layout of the ATLAS calorimeters and how they complement each other to form a hermetic system.

2.2.1 Electromagnetic Calorimeters

The Electromagnetic (EM) Calorimeter is a highly granular lead-liquid Argon sampling calorimeter with accordion-shaped lead absorbers and kapton electrodes. This geometry enables the detector to have a hermetically uniform azimuthal coverage while keeping the size of its gaps constant. It is divided into a barrel covering $|\eta| < 1.4$ and two end-caps covering each $1.375 < |\eta| < 3.2$. The EM calorimeter is required to reconstruct electrons with an energy ranging from a few GeV up to a few TeV. The ability to identify such low energy electrons can improve b-tagging by about 10%. The EM calorimeter is also expected to provide excellent energy resolution, with the resolution in terms of a sampling and constant term given by

$$\frac{\sigma_E}{E} = \frac{10\%}{\sqrt{E}} \oplus 0.7\%. \tag{2.1}$$

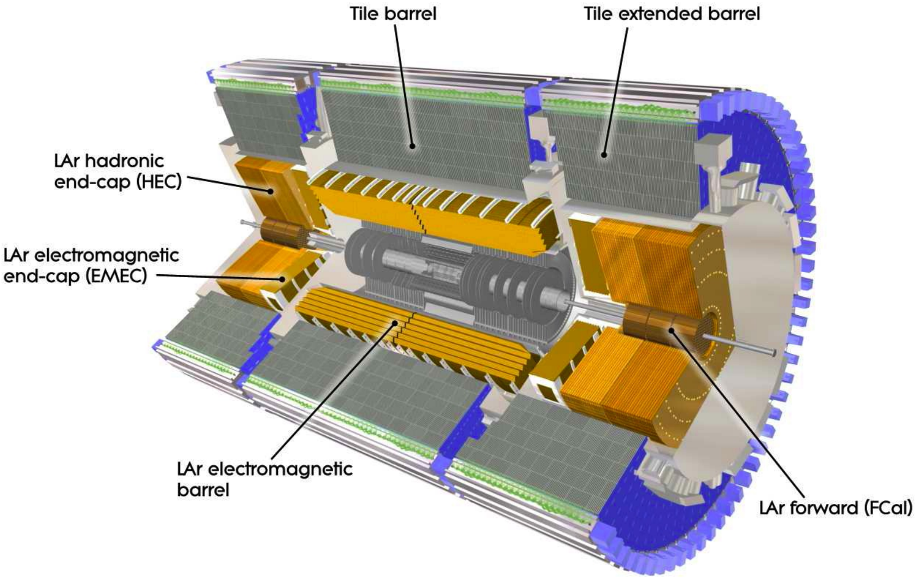

Figure 2.9: General layout of the ATLAS calorimeters showing a good hermeticity.

The requirements for linearity of the EM calorimeter are 10^{-4} in an energy interval given by the difference of the transverse energy spectrum of an electron from the $W^{\pm}$-boson decay and that of the Z^0-boson, and better than 0.5% for energies below 300 GeV [18]. A more detailed description of the EM calorimeter will be given in chapter three of this dissertation.

2.2.2 Hadronic Calorimeters

The ATLAS hadronic calorimeters cover the pseudorapidity range $|\eta| < 4.9$ using three different techniques because of the wide spectrum of physics requirements and differing radiation environments. The region $|\eta| < 1.7$ is covered by the Tile Calorimeter while at larger pseudorapidities where radiation tolerance is crucial, the intrinsically radiation hard LAr technology is used in both the HEC and the FCAL.

The hadronic calorimeters are required to identify and measure the energy and direction of jets as well as the total E_T^{miss}. The required jet-energy resolution depends on the pseudorapidity region and is given by the following:

$$\frac{\sigma_E}{E} = \begin{cases} \frac{50\%}{\sqrt{E}} \oplus 3\%, & |\eta| < 3 \\ \frac{50\%}{\sqrt{E}} \oplus 10\%, & 3 < |\eta| < 4.9 \end{cases} \tag{2.2}$$

Through their ability to measure quantities such as leakage and isolation, the hadronic calorimeters are are well suited to complement the EM calorimeters in electron and photon identification. Because of their total thickness in terms of interaction length (11 λ), the hadronic calorimeters are capable of containing hadronic showers and minimizing punch-throughs into the muon system.

Hadronic Tile Calorimeter

The Tile Calorimeter (TileCal) is a sampling calorimeter that uses plastic scintillating tiles as active material and steel plates as absorbers. In addition to serving as absorbers, the steel structure also plays the role of magnetic flux return yoke for the solenoid magnet. The plates are laminated with pockets containing the scintillating tiles at periodic intervals. To improve the uniformity of their response, the tiles are wrapped in a special material called Tyvek.

Light from a scintillator is read out with 1 mm diameter wavelength shifting fibers on both sides of the tile and connected to two photo-multipliers placed outside of the calorimeter. While moving through the fibers, the light is shifted to a longer wavelength matching the sensitive region of the photomultipliers. The tiles are placed such that hadronic showers pass through them longitudinally as shown in figure 2.10. This configuration ensures a better homogeneity and an easier read out of the light than in previous experiments. Because the TileCal is part of the ATLAS Level-1 trigger system this read out has the additional requirement that it has to be very fast.

The TileCal is segmented into one barrel and two extended barrels each consisting of 64 independent azimuthal modules divided in cells and towers. Its coverage in pseudorapidity extends to $|\eta| < 1.7$. Like the other hadronic calorimeters, the TileCal is required to identify and measure both energy and direction of jets with a relative energy resolution of

$$\frac{\sigma_E}{E} = \frac{50\%}{\sqrt{E}} \oplus 3\%. \tag{2.3}$$

in addition to providing a good measurement of E_T^{miss}.

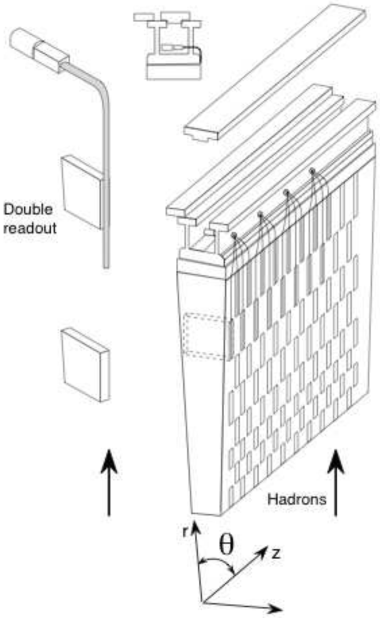

Figure 2.10: Principle of an ATLAS tile calorimeter module.

Hadronic Forward Calorimeters (FCAL)

The FCAL is made of rod shaped electrodes (Fig. 2.11) inserted inside a tungsten matrix (details shown in figure 2.12). The electrodes consist of a rod inside an outer tube such that there is a cylindrical shell gap of LAr between the two. A polyimide-coated quartz fiber is wound onto the rod to help center the rod in the tube. One end of each rod holds a signal pin. Rods are held at positive high voltage while the tubes and the matrix are grounded. The FCAL provides electromagnetic as well as hadronic coverage in the very forward region $3.2 < |\eta| < 4.9$. It is located in the inner bore of the HEC and around the beam pipe. Because of its location, the FCAL is designed to sustain high levels of radiation. The first of three FCAL modules uses copper (Cu) as absorber while the remaining two use tungsten. Because of the high counting rate associated with its position, the active gaps are much thinner than with the other LAr calorimeters.

Hadronic End cap Calorimeters

The Hadronic End-cap Calorimeter (HEC) is a LAr sampling calorimeter with copper-plate absorbers, designed to provide coverage for hadronic showers

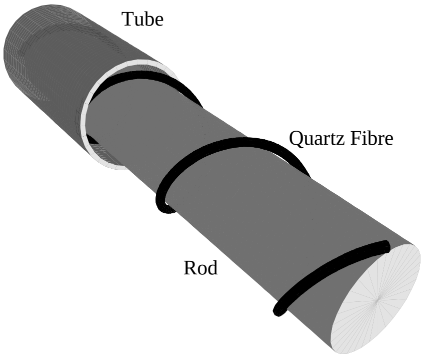

Figure 2.11: Detail of an FCAL narrow gap rod.

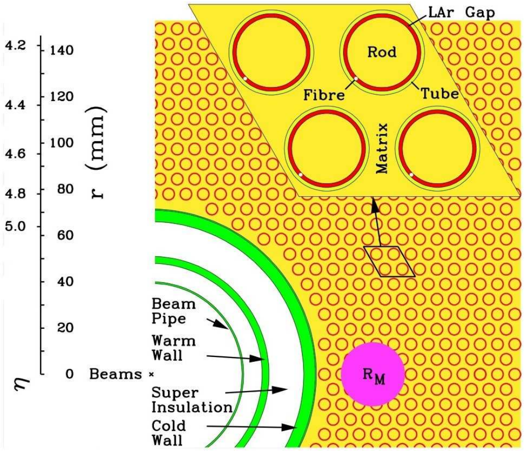

Figure 2.12: Illustration of the matrix of rods within the FCAL assembly.

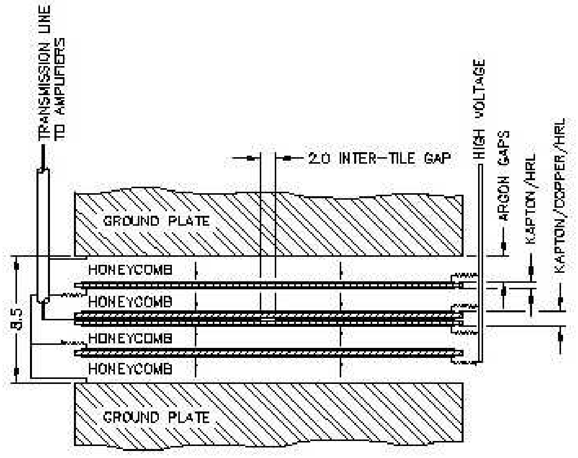

Figure 2.13: Read out structure of the HEC in the inter-plate gap.

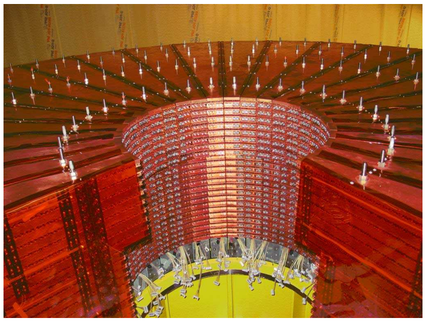

Figure 2.14: Illustration of the matrix of rods within the FCAL assembly.

in the range $1.5 < |\eta| < 3.2$. The HEC uses parallel plate geometry chosen for the simplicity of its design. The gaps between copper plates are instrumented with a read out structure designed to optimize signal to noise ratio while reducing high-voltage requirements (Fig. 2.13). The HEC is housed behind the EMEC but in the same cryostat. Each HEC consists 32 modules housed in two independent wheels (Fig. 2.14) of outer radius 2.03m. Each module of the front wheel is made of 24 copper plates of 25 mm thickness, while each module of the rear wheel is made of 16 copper plates of 50 mm each.

2.3 Muon Spectrometer

The ATLAS muon system serves as both a trigger for the selection of events with high energy muons and as a precision muon spectrometer. It is, in terms of volume, the largest component of the ATLAS detector. The design of the muon spectrometer uses four different detector technologies including two types of trigger chambers and two types of high precision tracking chambers. The muon chambers (shown in Fig. 2.15) form three concentric cylindrical layers at radii around 5, 7.5 and 9.5 m in the barrel region and cover a pseudorapidity range of $|\eta| < 1.0$. In the forward region ($1.0 < |\eta| < 2.7$), the chambers are arranged in four vertical disks concentric and perpendicular to the beam axis at distances of 7, 11, 13.5 and 22 m from the interaction point (see Fig. 2.16).

The muon trigger system comprises the Resistive Plate Chambers (RPC) in the barrel region and Thin Gap Chambers (TGC) in the forward region. The ATLAS trigger system is designed to reduce the LHC interaction rate of about 1 GHz to the foreseen storage rate of about 100 MHz. The trigger chambers must be able to identify the LHC bunch crossing, trigger with a well defined P_T cut-off and measure the coordinates in the direction orthogonal (ϕ coordinate) to the one measured by the precision chambers with a resolution of 5-10 mm. The high precision tracking system comprises the Monitored Drift Tubes (MDT) and the Cathode Strip Chambers (CSC). The precision chambers are required to measure spatial coordinates in two dimensions and to provide good mass resolution as well as a good transverse momentum resolution in both the low and high P_T regions. The performance benchmark, given the magnetic field and the size of the spectrometer, requires a position resolution of 50 μm. The spectrometer is designed such that particles from the interaction vertex traverse always three stations of chambers. Only the trigger chambers are read out to the level1 trigger.

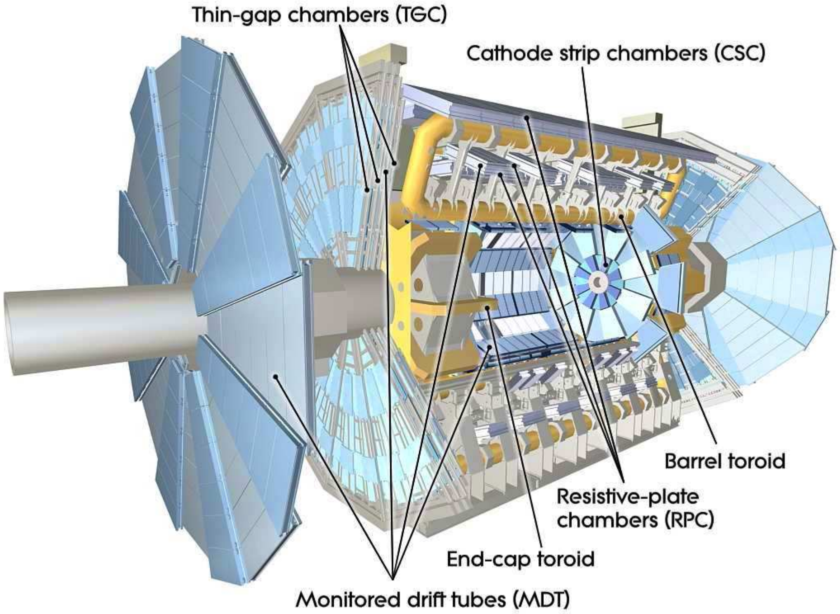

Figure 2.15: 3D view of the ATLAS muon spectrometer showing areas covered by the four different chamber technologies.

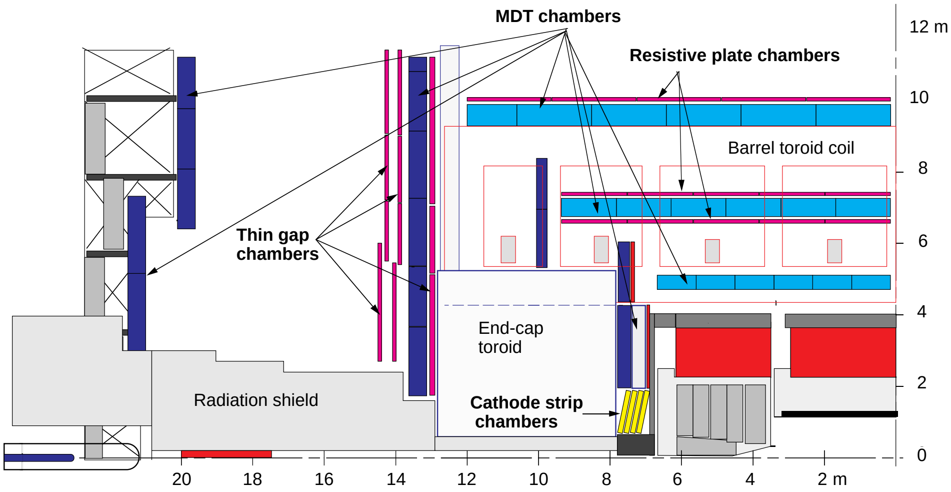

Figure 2.16: R-Z view of one quadrant of the ATLAS muon spectrometer. High energy muons will typically traverse at least three stations.

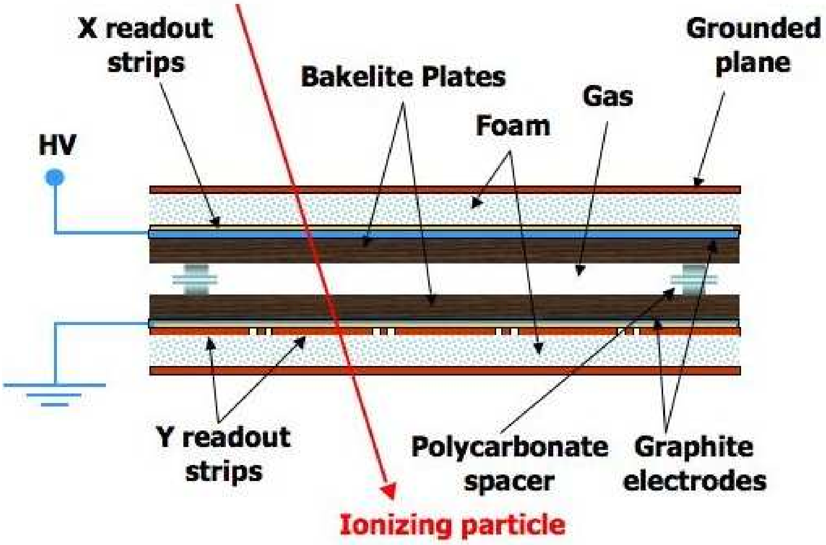

Figure 2.17: Concept of an ATLAS RPC. An incoming particle (red arrow) ionizes the gas enclosed between the two plates (brown).

2.3.1 Resistive Plate Chambers

A resistive plate chamber (RPC) is made of two independent gas gaps formed by two parallel resistive ($\rho \sim 10^{10}\Omega$cm) bakelite plates separated by 2 mm polycarbonate spacers (Fig. 2.17). The gas mixture is composed of 94.7% tetrafluorethane ($C_2H_2F_4$), a gas that allows for a relatively low operating voltage, 5% isobutane (iso-C_4H_{10}) and 0.3% hexafluoride (SF_6). On both sides of each gas volume are placed two orthogonal pick-up strip planes which allow independent measurement of both the η and ϕ coordinates. The number of strips (average strip pitch is 3 cm) per chamber is variable: 32, 24, 16 in η and from 64 to 160 in ϕ. When a particle goes through an RPC chamber, the primary ionization electrons are multiplied into avalanches by a high electric field of typically 5 kV/mm thus producing pulses of typically 0.5 pC. The signal is read out via a capacitive coupling of strips on both sides of the chamber. More than 1000 RPC units of different sizes will be installed in the barrel of the muon spectrometer, covering a surface of about 3650 m^2[12].

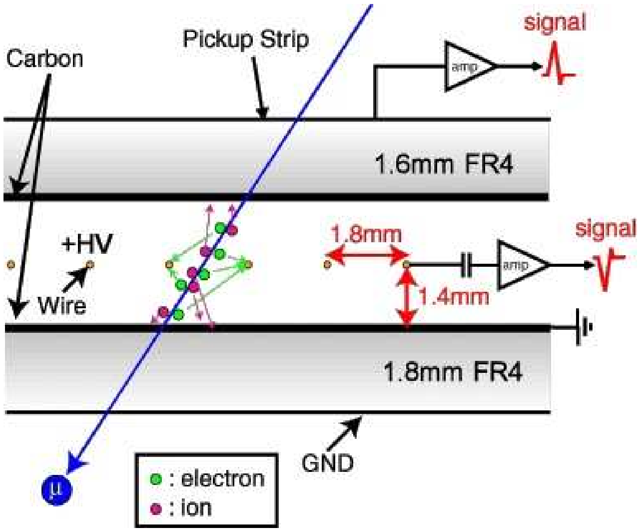

Figure 2.18: Concept of an ATLAS TGC showing anode wires and graphite (carbon) cathodes.

2.3.2 Thin Gap Chambers

Thin Gap Chambers (TGC) are very thin multiwire proportional chambers (MWPC) in which two graphite cathode planes form a gas volume where gold coated anode wires of 50 μm diameter are installed with a pitch of 1.8 mm. The peculiarity of TGCs compared to regular MWPCs is that cathode-anode spacing is smaller than the anode-anode (wire-wire) spacing (Fig. 2.18). This characteristic makes for a shorter drift time and excellent timing resolution of less than 20 ns, which meets the requirement for the identification of bunch crossing at 40 MHZ. The gas mixture used in the ATLAS TGCs is composed of 55% CO_2 and 45% n-pentane C_5H_{12}. This is a highly flammable mixture that requires extreme precaution. The read out strips are orthogonal to the anode wires. This configuration allows for an independent measurement of the r coordinate provided by groups of 4 to 20 wires and of the ϕ coordinate.

2.3.3 Monitored Drift Tubes

A monitored drift tube (MDT) chamber consists of many layers of 30 mm diameter drift tubes each outfitted with a central W-Re wire of 50 μm (see Fig. 2.19 and 2.20). The MDTs are operated with a gas mixture of 93% Argon and 7% CO_2 at a pressure of 3 atm. The tube lengths vary from 70 to 630 cm as a function of chamber position around the detector. The chambers are

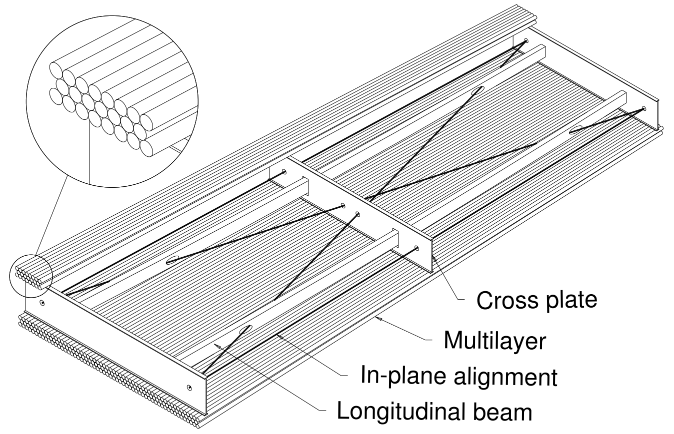

Figure 2.19: Schematic view of an ATLAS MDT module with detail of the tube arrangement in the inlet.

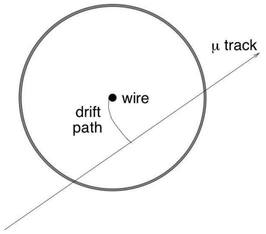

Figure 2.20: Drift path of an ionized particle in a magnetic field.

positioned orthogonal to the r-z plane (wires parallel to magnetic field lines) in both the barrel and end-cap regions, thus providing a very precise measurement of of the axial coordinate (z) in the barrel and the radial coordinate (r) in the transition and end-cap regions. The MDTs provide a maximum drift time of about 500 ns (35 μm/ns) and a single tube (wire) resolution of 80 μm, while the resolution in the bending direction is 40 μm. The precision measurement of muons tracks are done everywhere using MDTs except in the innermost ring of the inner station of the end-cap, where particle fluxes are highest. In this region the CSCs are used.

2.3.4 Cathode Strip Chambers

The ATLAS Cathode Strip Chambers (CSC) (Fig. 2.21 and 2.22) are MWPCs with symmetric cells in which anode-cathode spacing of 2.54 mm is equal to the anode-anode (wire-wire) pitch. Each CSC chamber consists of 4 layers. The CSCs are operated with a non flammable gas mixture of 80% Argon and 20% CO_2 and provide a drift time of 30 ns. An r.m.s time resolution of 3.2 ns makes for a fully efficient bunch crossing resolution. Each layer contains a total of 768 precision (x) strips orthogonal to the anode wires and 192 coarser y strips parallel to the anode. The precision coordinate is obtained by measuring the charge induced on the cathode strips by the avalanche formed on the anode wire. Good spatial (r) resolution (60 μm) is achieved by segmentation of the

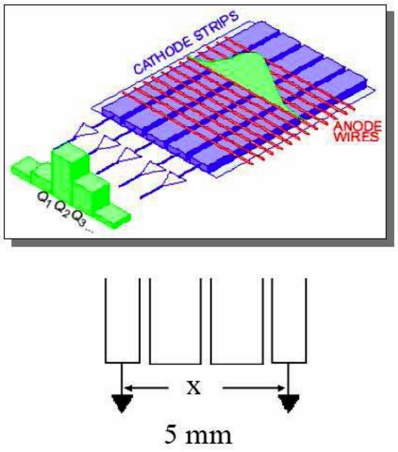

Figure 2.21: Schematic view of the ATLAS CSC cathode and anodes layout.

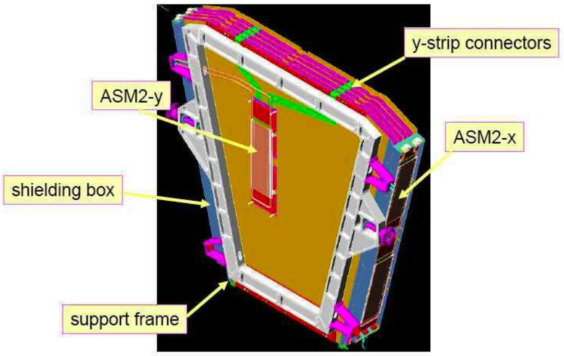

Figure 2.22: A CSC chamber model shown with read out electronics.

read out cathode and by charge interpolation between neighboring strips. The parallel strips provide the ϕ coordinate. Installed at a distance of seven meters from the interaction point and $2.0 < |\eta| < 2.7$, these muon detectors will be particularly vulnerable and are built to survive the high radiation environment produced by the colliding high-energy protons.

2.4 Magnet System

The ATLAS superconducting magnet system consists of a central solenoid (CS) and three large air-core toroids. Its design was motivated by the need to provide the optimised magnetic field configuration for particle bending around the various detectors while minimizing scattering effects.

The three air-core toroids (Fig. 2.23) consists of a barrel toroid (BT) (Fig. 2.25) and two end-cap toroids (ECT) (Fig. 2.26). Each of the three toroids consists of eight superconducting coils assembled symmetrically around the beam axis and parallel to it. For the BT, the coils are of a racetrack type, each 25 m long, 5 m wide and weighing 100 tons, grouped in torus shape and placed in eight separate cryostats kept in position by 16 support rings. The ECT, positioned inside the BT at both ends of the CS, is also made of eight racetrack type superconducting coils placed in one single cryostat per end-cap. On November 9, 2006, the BT was tested in its final configuration and reached the nominal field of 4 T in its coil windings, with an electric current of 21 kA

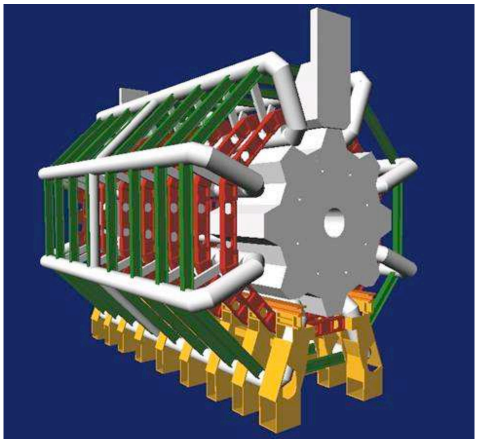

Figure 2.23: Schematic view of part of the ATLAS magnet system. The donut shaped barrel torroids and end-cap torroids are shown in grey while the support structure is shown in green red and yellow.

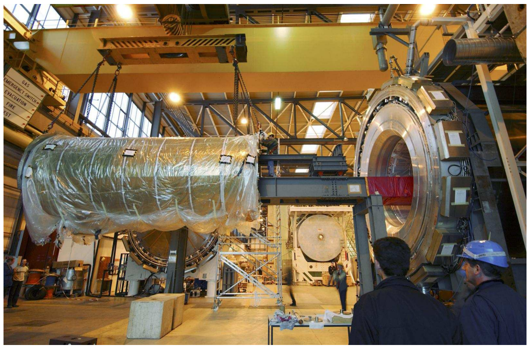

Figure 2.24: Central solenoid (left), wrapped in a protective shield, is shown during insertion in the LAr cryostat (right) at CERN.

passing through the eight superconducting coils.

The central solenoid (Fig. 2.24), cooled by helium at 4.5 K, provides the magnetic field for the ID. It is integrated directly inside the cryostat of the Liquid Argon calorimeter thus eliminating the need for additional vacuum walls and reducing the amount of material in front of the calorimeter. Indeed, an excess of material in front of the calorimeter would cause many particles to start showering before they reach active calorimeter cells. The CS creates a central field with a nominal strength of 2 T at the interaction point and a peak of 2.6 T at the level of the superconductors.

Both BT and ECT generate a precise, stable and predictable magnetic field of 3 to 8 Tm for the ATLAS muon spectrometer. This field is produced in the barrel region ($|\eta| \leq 1.0$) by the BT and in the forward region ($1.4 \leq |\eta| \leq 2.7$) by the ECT, while in the transition region ($1.0 \leq |\eta| \leq 1.4$), it is produced by a combination of the two.

2.5 Trigger and Data Acquisition

The ATLAS trigger and Data Acquisition system (TDAQ) is organized in three trigger-levels (LVL-1, LVL-2 and LVL-3 or event filter) as seen in figure 2.27. The trigger system has the challenging role of selecting bunch crossings

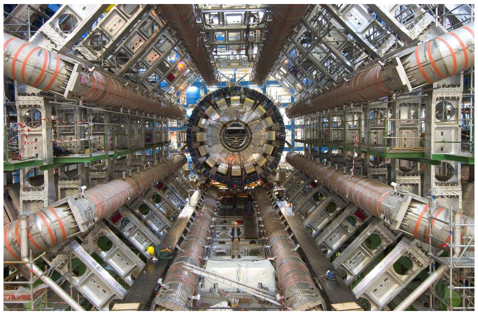

Figure 2.25: The eight barrel toroids in their final position before insertion of the calorimeter. The massive support frames of the toroids can be seen.

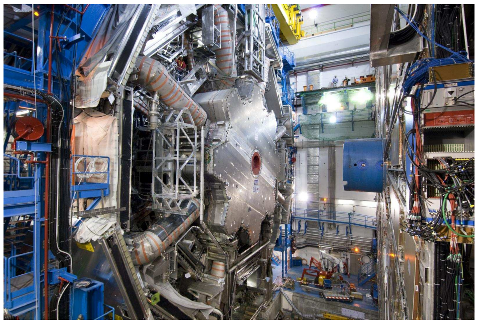

Figure 2.26: One of two end-cap toroids inserted in its final position.

containing interesting events by reducing the data rate from 40 MHz (collision rate) to 200 Hz. Decisions made by a given trigger level are used as input at the subsequent level.

The LVL1 trigger searches for signatures of high-P_T muons in the muon system trigger chambers (RPCs and TGCs), and for signatures of jets, electrons/photons clusters, τ-leptons decays, and large missing transverse energy (E_T^{miss}) in the calorimeter. It also identifies Regions-of-interest (RoI) of the detector associated with those signatures and informs the front-end electronics. While events are accepted by the LVL-1 trigger system at a maximum rate of 75 kHz, its decision must reach back the front-end electronics within 2.5 μs after the bunch-crossing with which the event is associated.

The LV-2 trigger reduces further the event rate to below 3.5 kHz by using detailed information about the RoIs. It accomplishes this feat by having full access to the granularity of the calorimeter as well as precise coordinates from the inner detector. The event builder system assembles and ships to the LVL-3 trigger the full event data of all events accepted by the LVL-2. The average event processing time at this level is about 40 ms per event.

The LVL-3 trigger uses up to date detector information including magnetic field maps, calibration results and full granularity and precision of the calorimeter, muon system and ID to further reduce the event rate to about 200 Hz equivalent to a data storage flux of about 300 MB/s.

All the data flow between various front-end electronics and different trigger levels is organized by the Data Acquisition (DAQ) system. It stores the information from all detectors in pipelined memories while decision is being

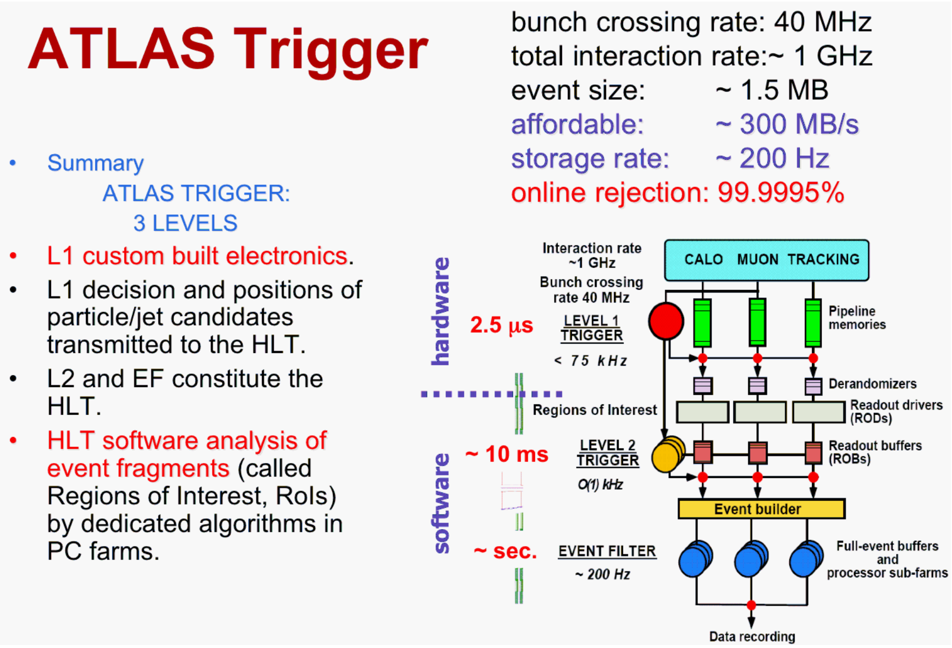

ATLAS Trigger

bunch crossing rate: 40 MHz
total interaction rate:~ 1 GHz
event size: ~ 1.5 MB
affordable: ~ 300 MB/s
storage rate: ~ 200 Hz
online rejection: 99.9995%

- Summary
  ATLAS TRIGGER:
  3 LEVELS
- L1 custom built electronics.
- L1 decision and positions of particle/jet candidates transmitted to the HLT.
- L2 and EF constitute the HLT.
- HLT software analysis of event fragments (called Regions of Interest, RoIs) by dedicated algorithms in PC farms.

Figure 2.27: The ATLAS trigger levels and Data Acquisition system [13].

made (latency) by the trigger system. The DAQ also provides configuration, control and monitoring of the ATLAS detector during data-taking.

Chapter 3

The Liquid Argon Electromagnetic Calorimeter

The Electromagnetic (EM) calorimeter is a lead-liquid argon sampling detector with an accordion geometry. The detector guarantees full azimuthal acceptance ($0 < \phi < 2\pi$) as well as a coverage in the pseudorapidity region of $|\eta| < 3.2$ and is divided in one barrel ($|\eta| < 1.475$) and two end-caps ($1.375 < |\eta| < 3.2$). The EM calorimeter is segmented in depth in three layers labeled "Strips", "Middle", and "Back". Because the EM calorimeter has to match challenging requirements for energy, position and time resolutions, liquid argon (LAr) was chosen for its intrinsic linear behavior, response stability and radiation tolerance. The lead absorbers provide the required thickness for the absorption of high energy electrons and photons.

The EM calorimeter is complemented by a 11 mm thick LAr presampler detector placed in front of its inner cold wall. The barrel presampler covers the full η range. The presampler is made of interleaved cathode and anode electrodes glued between glass-fiber composite plates. The role of the presampler is to provide shower sampling in front of the EM calorimeter in order to correct for energy lost in the material upstream of the EM calorimeter. The end-cap presampler covers the region $1.5 < |\eta| < 1.8$. Its role is to improve the energy measurement in the barrel/end-cap transition region filled with dead material made of ID services (see chapter 5).

The LAr EM calorimeter will play a key role in measuring energy, position and time of electrons, photons and jets. The construction of the ATLAS EM calorimeter is described in great detail in [14].

3.1 Physics of Calorimetry

High-energy electrons, positrons, and photons traversing matter interact through well-known electromagnetic p rocesses described by Quantum Electrodynamics: ionization, bremsstrahlung and pair-production. Typically high-energy positrons or electrons radiate bremsstrahlung photons when passing through matter. The resulting photons can give rise to $e^{+}e^{-}$ pairs which in turn radiate more photons. The EM shower continues until the energy of particles fall below the threshold for pair production. These processes are described in more detail in chapter 5 which deals with the dead material in the barrel/end-cap transition region.

3.1.1 Sampling Calorimetry

The unit of a typical noble liquid sampling detector is made of a gap formed by two parallel plate absorbers. In the case of the ATLAS EM calorimeter, the gap is filled with liquid argon while the absorbers are made of lead plates sandwiched between two stainless-steel sheets (0.2 mm thick) glued using a resin-impreganted glass-fibre fabric to provide mechanical strength (see Fig. 3.1). A potential difference is applied between the grounded plates and read out electrodes. These electrodes are made of three conductive copper layers separated by two insulating kapton (polyimide) sheets. The two outer copper layers are connected to the high voltage while the central layer is used for reading out the signal via capacitive coupling. In the Barrel, the absorbers have two different thicknesses (1.53 mm for $|\eta| < 0.8$ and 1.13 mm for $|\eta| > 0.8$) to limit the decrease of the sampling fraction as $|\eta|$ increases [15], while in the end-caps the absorber thickness vary from 1.7 mm for $|\eta| < 2.5$ and 2.2 mm for $|\eta| > 2.5$). Liquid argon was chosen because of its intrinsic linear behavior (good density and homogeneity), response stability, and radiation tolerance.

The high-energy particles will lose energy by ionizing the material they traverse. The ionized charge drifts, under the influence of the electric field in the LAr gap, towards the electrodes where they induce an electrical signal. This signal is proportional to the energy deposited in the LAr gap. Sampling calorimeters like the ATLAS EM calorimeter are built such that only a fraction of the total energy is deposited in the active LAr gap. The ratio of the energy deposited in the active LAr gap to the total energy deposited is called the sampling fraction. Thus the total energy of the shower is obtained by multiplying the measured (sampled) energy with the inverse of the sampling fraction.

The sampling term is larger for sampling calorimeters as less of the shower

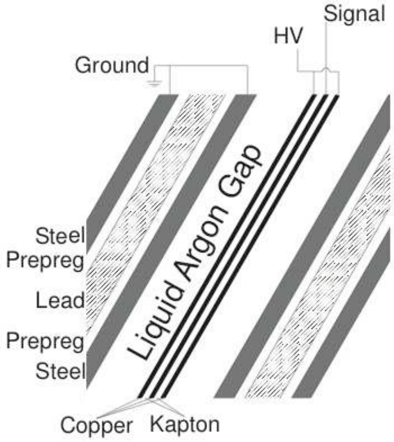

Figure 3.1: Detailed structure of a sampling layer of the ATLAS EM calorimeter.

is measured. The distribution of the number of charged particles in the shower has a fractional width given by $\sqrt{n}/n = 1/\sqrt{n}$. Therefore the reconstructed energy fluctuates as well and the relative precision of the energy E measured by a sampling calorimeter can be written as $\sigma_E/E = a/\sqrt{E}$, where the second term ($a/\sqrt{E}$) is called the *stochastic* or *sampling* term. Adding a third term (b/E) for the electronics noise and pileup and yet a fourth constant term (c) to account for effects such as imperfection in the construction and calibration of the calorimeters or fluctuations of the energy lost in the dead areas, the energy resolution of a realistic calorimeter like the ATLAS EM calorimeter can be parametrized as [16]:

$$\frac{\sigma_E}{E} = \frac{a}{\sqrt{E}} \oplus \frac{b}{E} \oplus c. \tag{3.1}$$

Clearly the relative energy resolution improves with energy and both the *sampling* and the electronics noise terms can be neglected in favor of the constant term for very high energies.

3.2 Construction and Assembly of the LAr EM Calorimeter

Construction of the LAr EM calorimeter has been finished and its various components assembled and installed in their final position within the ATLAS

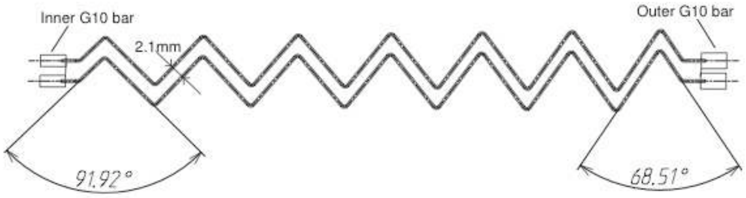

Figure 3.2: Detail of the accordion folding of the EM barrel calorimeter.

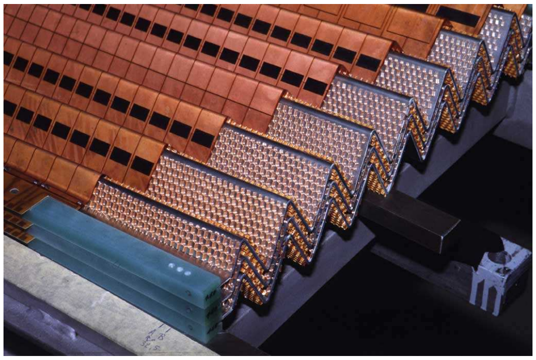

Figure 3.3: 3D detail of the accordion folding of the EM calorimeter. Spacing of the absorbers is maintained by blue G10 bars (fiberglass-epoxy) placed at both ends. The electrode etching can be seen as well as the honeycomb spacers.

detector in the collision hall.

3.2.1 The Barrel

As noted above, an accordion geometry has been chosen for the ATLAS LAr EM Calorimeter because it provides a full azimuthal coverage (in ϕ) and also because it enables a fast signal extraction at both ends (front and rear) of the electrodes. Fig. 3.2 and 3.3 show how the absorbers and electrodes are bent to form the accordion shape. The flexible electrodes are held in place with honeycomb spacers. The LAr gap, and therefore the sampling fraction, is held constant by varying the bending angles as a function of radii and by optimizing the absorber design in terms of the lead thickness. The bending angles decrease with increasing radii.

The barrel cryostat is composed of two concentric cylindrical aluminum vessels centered on the beam axis (z-axis), an inner cold vessel and an outer warm vessel separated by an insulating vacuum in which the central solenoid is housed. The barrel is made of two half-barrels separated by a 6 mm gap at z = 0. Each half-barrel is divided into 16 modules and made of a total of 1024 accordion-shaped absorbers interleaved with electrodes. In the barrel the accordion waves are axial and run in ϕ. The thickness of the modules vary as a function of η from 22 X_0 to 33 X_0.

The EM Barrel Calorimeter (EMB) is segmented in depth into three layers (Fig. 3.4) with a total of 150000 cells. In ϕ, cells are obtained by connecting neighboring read out electrodes while in η the segmentation is achieved by etching the copper of the signal layer of the electrodes. The first sampling, otherwise referred to as "Strips", has a very fine granularity in η and a relatively coarser granularity in ϕ. The "Strips" has a thickness of approximately 4.3 X_0. The second sampling, also called "Middle", is segmented into square cells of size $\Delta\phi \times \Delta\eta = 0.0245 \times 0.025$ each of which covers 8 "Strips" cells in η and 1/4 "Strips" cells in ϕ. The "Middle" sampling is about 16 to 19 X_0 thick and is the siege of most of the energy deposit in the EM calorimeter. The third sampling ("Back") is segmented into cells of size $\Delta\phi \times \Delta\eta = 0.025 \times 0.05$ and has a thickness varying from 1.4 to 7 X_0.

3.2.2 The End-Caps

The Electromagnetic End-Cap Calorimeter (EMEC) consists of two wheels located on either sides of the barrel. Each end-cap is itself divided into two co-axial wheels separated by a 3 mm thick layer of low density material. The outer wheel covers the region $1.375 < |\eta| < 2.5$ while the inner wheel covers the region $2.5 < |\eta| < 3.2$. The end-cap wheels are each divided into eight wedge-shaped modules (Fig. 3.6). In the end-cap, the absorber plates are arranged radially and the accordion waves are parallel to the radial direction and run axially. Unlike the EMB, the LAr gap of the EMEC is not constant, rather it is a function of the radius and varies in both the inner wheel (from 3.1 mm to 1.8 mm) and the outer wheel (from 2.8 mm to 0.9 mm). The total thickness of the EMEC vary as a function of η from about 24 X_0 to 38 X_0.

The precision region ($1.5 < |\eta| < 2.5$) of the EMEC is segmented in depth in three longitudinal layers, Strips, middle and back, while the outermost region ($|\eta| < 1.5$) of the outer wheel and the inner wheel ($2.5 < |\eta| < 3.2$) are segmented in two layers. The first layer of the precision region, the "Strips", has a thickness of approximately 4.4 X_0. The "Middle" layer is segmented into square cells of size $\Delta\phi \times \Delta\eta = 0.0245 \times 0.025$, while in the "Back" the granularity is $\Delta\phi \times \Delta\eta = 0.025 \times 0.05$. The rest of the end-cap wheels (non-precision region) is segmented into two longitudinal layers with a coarser granularity.

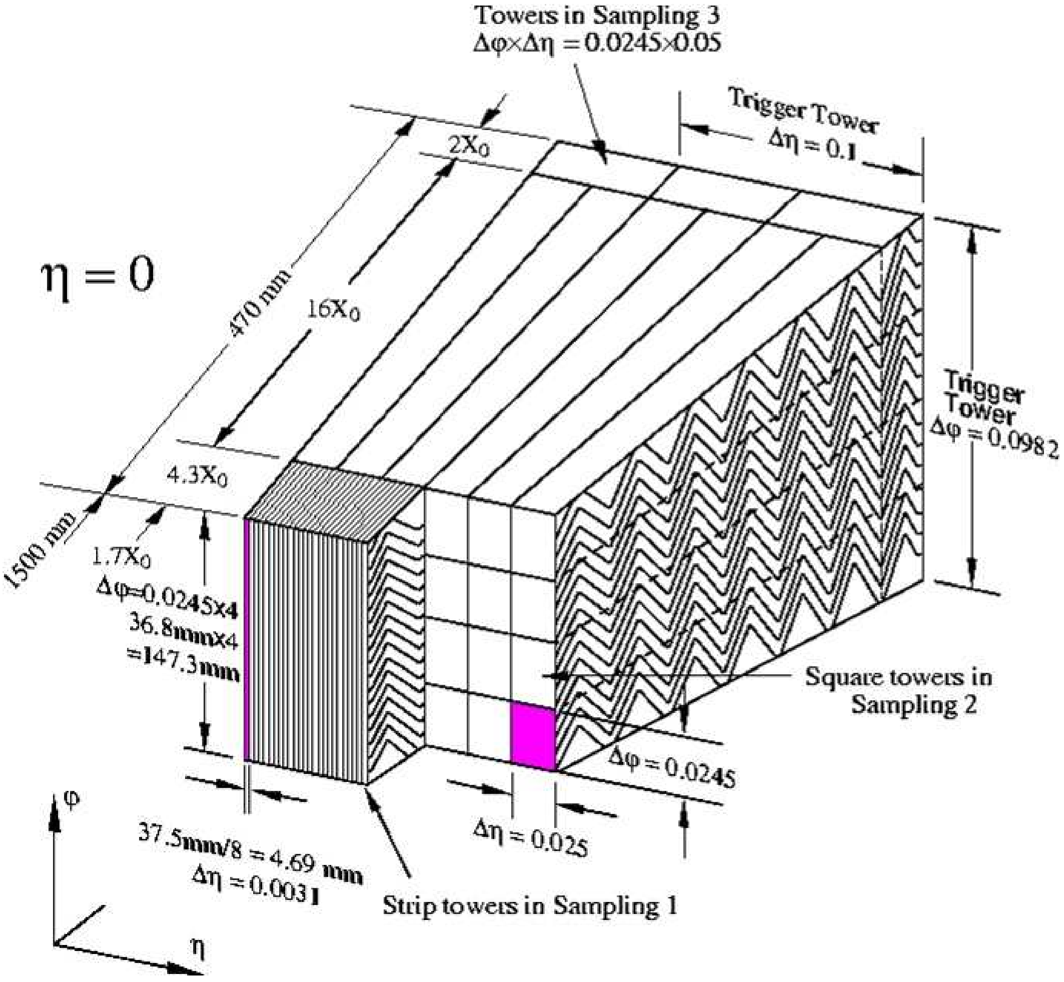

Figure 3.4: 3D view of the layout of the 3 different sampling layers of the barrel EM calorimeter in terms of depth in X_0 and granularity in ϕ and η.

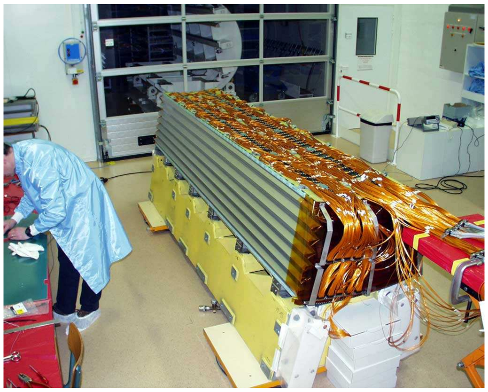

Figure 3.5: Module of the EMB calorimeter shown during assembly.

Figure 3.6: Module of the EMB calorimeter shown during assembly. Eight such wedge-shaped modules combine to form a wheel.

3.2.3 High Voltage

One high-voltage feedthrough port [19] is mounted close to the highest point of each half-barrel. A port holds approximately 840 HV lines including spares. The nominal high-voltage for the barrel EM calorimeter is 2000 V with a corresponding drift time for the LAr gap of 2.1 mm (from electrode to absorber) of about 450 ns. The high-voltage for the end-caps is η dependent. It decreases with increasing η from 2500 V to 1000 V. The end-cap presampler's electrodes are the only ones with negative voltage (-2000 V) applied to them.

The two high-voltage sides of each electrode are fed independently. This insures that at least half of the signal will be collected even if only half of the electrode is powered. The high-voltage granularity of the barrel ($\Delta\phi \times \Delta\eta = 0.2 \times 0.2$) is such that 32 electrode sectors are powered simulatneously. However, in case of high-voltage problems, contingency plans allow for one electrode sector to be powered individually or divided into two halves (in ϕ) to be powered separately depending on the circumstances. The high-voltage feedthroughs and filters will receive an extensive treatment in chapter 4 of this thesis.

3.2.4 Signal Feedthroughs

The electronic signals from the EM barrel calorimeter are carried out by means of 64 signal feedthroughs (32 per half-barrel) located radially around the ends of the cryostat. The signal feedthroughs [17] insure the passage of the signal, monitoring, calibration and spare lines (122800 lines) through both cryostat walls with minimal heat transfer. A signal feedthrough consists of a warm flange and a cold flange, with a flexible bellows welded between them and the volume between the two flanges is under vacuum. Signal cables emanating from the feedthroughs are connected, via the pedestals, to the Front-End electronics housed in 32 Front-End crates (2 feedthroughs per crate). Both pedestals and crates sit directly atop the feedthroughs to minimize the lengths of the signal cables, which end at the backplane of the crate. Each crate is equipped with 14 Front-End boards, one Monitoring board, and one Tower-builder board, all plugged into the backplane. FEBs are water cooled to cope with the significant amount of heat they dissipate.

3.3 Electronic Signal Processing and Calibration

As seen in section 3.1.1, the energy resolution of the ATLAS EM barrel calorimeter is influenced by an electronics noise and pileup term (b/E) as well as a constant term (c) that relies on the calibration of the electronics chain. To ensure that both b/E and c remain small, the read out electronics must be extremely stable and accurate and the calibration system very precise. Indeed the design resolution of the EM calorimeter is

$$\frac{\sigma E}{E}(\%) = \frac{10\%}{\sqrt{E}} \oplus 0.7\%, \tag{3.2}$$

where the read out electronics is required not to contribute more than 0.5% to the constant term. Furthermore, because of their location inside or on the cryostat, the the read out electronics must be able to cope with significant radiation levels of the order of 850 Gy.

3.3.1 Front-End Electronics

The first elements of the electronics read out chain are the summing boards, which are connected to the electrodes, grouping the signals in ϕ. A summing board services 16 electrodes for the barrel. The first sampling of the barrel is read out from the front (cryostat bore) while the second and third samplings are read out from the back (outer radius). The summing boards generate analogue sums from adjacent calorimeter gaps. All electrodes of the first sampling are summed into one read out cell, while for the second and third sampling electrodes are summed in four adjacent cells. Sitting directly on top of the summing boards, motherboards provide read out for a region of size $\Delta\phi \times \Delta\eta = 0.2 \times 0.2$ and distribute calibration pulses to all read out channels through tantalum-nitride calibration resistors. Presampler modules are also equipped with identical motherboards and calibration resistors. The output signal from the motherboards are then routed, through connectors designed to minimize cross-talk between read out channels, first to patch panels and then to the signal feedthroughs.

Fig. 3.7 shows a schematic of the read out electronics for the barrel EM calorimeter. The first stage of the signal processing, already described above, takes place inside the cold walls of the cryostat and involves the summing boards and motherboards. In the second stage, the electronic signals are sent to the front-end crates via the feedthroughs and processed in various stages by the Front-end Boards (FEB). Each FEB can amplify, shape, sample, and digitize the signals of up to 128 cells before sending the output for further processing to the Read Out Driver (ROD) and Data Acquisition system (DAQ), in the third stage taking place outside the collision hall.

Signals entering the FEBs are first dispatched to the right preamplifier, which is a current sensitive low noise amplifier, depending on the location of the cell that originated the signal. After amplification, the signals are sent to the shaping amplifier. The role of the shaping amplifier is to optimize the signal-to-noise ratio by splitting into three gain scales (1:10:100 or low, medium, and high) and shaping the signals with a bipolar function. Thus, the negative triangular ionization signal received from the cell is transformed into a smooth curve (Fig. 3.8) with a peak amplitude proportional to the energy deposited in the cell.

After shaping, the signals are sampled at the bunch crossing frequency of 40 MHz and stored in the appropriate Switched Array Capacitor (SCA), depending on the gain, until decision arrives from the first level of the trigger system (LVL1). Events that pass the LVL1 decision are then digitized by a 12-bit Analog-to-Digital Counter (ADC). The FEBs can function in either normal or automatic gain modes. Samples for all three gains are digitized in normal mode , while in automatic mode the gain selection logic decides which sample is to be digitized based on the amplitude of a fixed sample in the medium gain. The digitized samples are sent to the ROD modules via an optical link.

3.3.2 Back-End Electronics

The main element of the back-end electronics is the ROD whose most essential component is the Field Programable Logic Gate Array (FPGA). Each

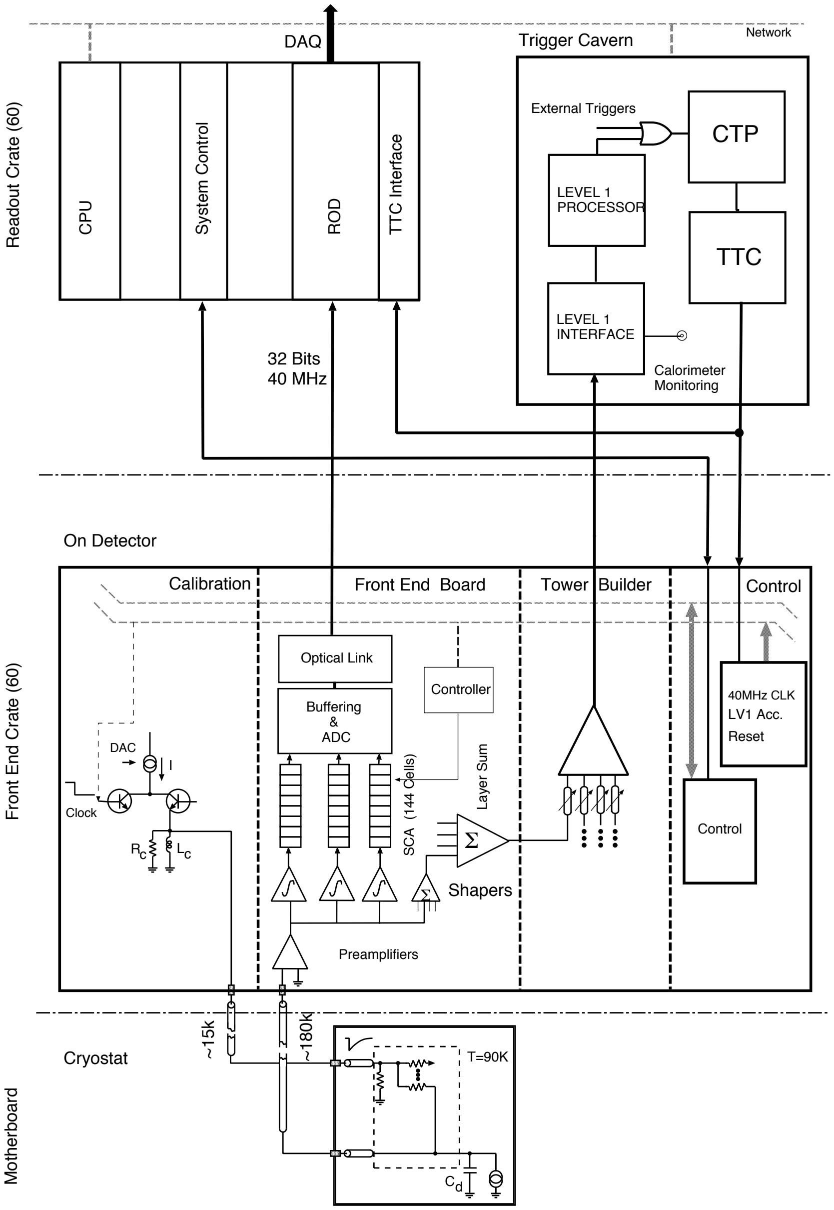

Figure 3.7: Schematic of the read out electronics for the EMB, EMEC and FCAL. For the HEC, the preamplifiers are replaced by a preshaper

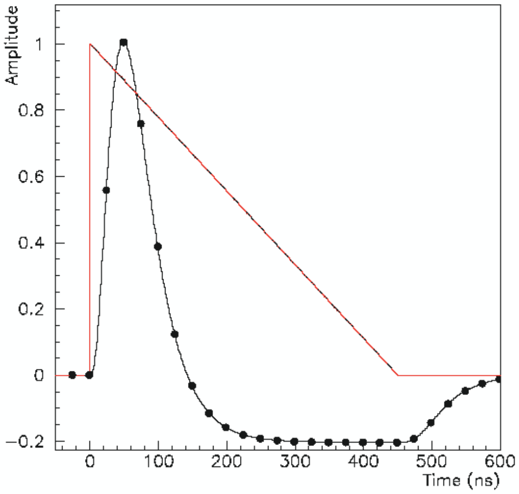

Figure 3.8: Bipolar shaping (black curve) of the triangular ionization signal in red. The signal was sampled at every bunch crossing or 25 ns (black dots).

ROD receives data from eight FEBs via the optical fibers. Each ROD has an input bandwidth of 12.8 GB/s. The FPGA chips preprocess the data before sending it to the Digital Signal Processor (DSP) for further treatment. The DSPs have the capability of either calculating the cell energy from the raw ADC samples with the use of Optimal Filtering Constants (OFC)[53], or simply forwarding the raw data directly to the output FPGAs.

3.3.3 Calibration

The components of the calibration system are also shown in Fig. 3.7. The calibration current is generated via an inductor, by a Digital-to-Analog Converter (DAC) whose value determines the amplitude of the signal. When the current is interrupted by the clock (or trigger), magnetic energy stored in the inductor produces a fast voltage pulse with an exponential decay. The pulse is then propagated to the cells via a resistive network located on the motherboards and designed for a precise distribution of the signal across the cells. One calibration line pulses either 16 presampler cells, 32 Strips cells, 8 Middle cells, or 8 Back cells. The pulsers are themselves located on the calibration boards (64 pulsers per board) in the electronics crates.

Chapter 4

The ATLAS High Voltage Feedthroughs for the Liquid Argon Calorimeters

4.1 Introduction

The purpose, design specifications, construction techniques, and testing methods are described for the high voltage feedthrough ports and filters of the ATLAS Liquid Argon calorimeters[19]. These feedthroughs carry about 5000 high voltage wires from a room temperature environment (300 K) through the cryostat walls to the calorimeters cells (89 K) while maintaining the electrical and cryogenic integrity of the system. The feedthrough wiring and filters operate at a maximum high voltage of 2.5 kV without danger of degradation by corona discharges or radiation at the Large Hadron Collider.

4.2 Conceptual design of the high-voltage feedthrough port

Feeding high-voltage (HV) wires into the LAr calorimeters presents different problems from those which must be solved in order to get the signals out of the LAr (at 89 K). The HV lines are especially susceptible to problems resulting from condensation near the exposed surfaces, so it is highly desirable to maintain the wire feedthroughs at ambient temperature (and if necessary heat them) in order to avoid condensation. The total cross section allotted to HV supply wires is severely limited as most of the available space around the edges of the cryostats is taken up by signal feedthroughs and cryogenic services. There is no requirement that the HV lines should enter the cryostat with axial symmetry (like the signal wires). Thus, the HV feedthroughs (HVFTs) are placed at the highest point on the cryostat and are kept at room-temperature, with a buffer volume of gaseous argon gas directly below the wire feedthroughs separating them from the liquid argon below. Being non-cryogenic simplifies the design of a very dense HV feedthrough greatly. The heat flow through the HVFT is limited by the choice of constantan conductor and by thin-walled and long metal bellows that flexibly link the outer and inner cryostat vessels.

The conceptual design of a HVFT port is shown in Fig. 4.1. The HV lines lead from the various calorimeter patch panels and come up through the surface of the LAr into a small pipe (73 mm inner diameter). A stainless steel bellows in this cold pipe accommodates the differential motion of the cold and warm walls during cooldown and serves as the dominant thermal resistance in the cold pipe. At approximately 0.9 m above the liquid, the cold pipe is welded to the warm pipe of the HVFT which is bolted to the outer cryostat vessel so that, above this point, the feedthrough (FT) wall is at room temperature. Above this point, the HV wires fan out to four HV Wire FTs (WFTs) mounted in a strong FT Plate, from where each wire is connected to its own RC filter to reduce electronic noise entering the cryostat. The HV filter section is also severely limited by the available space. A total of 840 HV channels is accommodated in each HVFT port. Two HVFT ports serve the barrel cryostat, one per end, and two ports serve each of the two end-cap cryostats. This makes for a total of six HVFT ports with 5040 HV channels, including about 10% spare channels.

Each HVFT port was constructed and installed in three parts: (1) the mechanical/cryogenic part consisting of the port proper; (2) the electrical part consisting of the FT plate with the four WFTs with HV wire bundle and HV backplane; and (3) the HV filter crate with filter modules. The ports were welded, installed, and first tested as part of the cryostat commissioning. The FT plate with HV wiring was installed later, at the time the calorimeter modules were installed in the cryostats. Finally, the HV filters were installed last after the cryostats were closed and HV testing in LAr was started.

4.3 Mechanical Construction of the HVFT ports

The mechanical design and technical specifications of one HVFT port are respectively shown in Fig. 4.2 and Table 4.1. A single port consists of several mechanical parts that are welded or bolted together. The parts and welded joints were designed and executed to meet stringent pressure codes.[1]

Depending on its location, end-cap or barrel, the bellows is first welded on either side to a long and a short cuff (end-cap) or to a long cuff and a

---

[1] ASME Boiler and Pressure Vessel Code (CODAP)

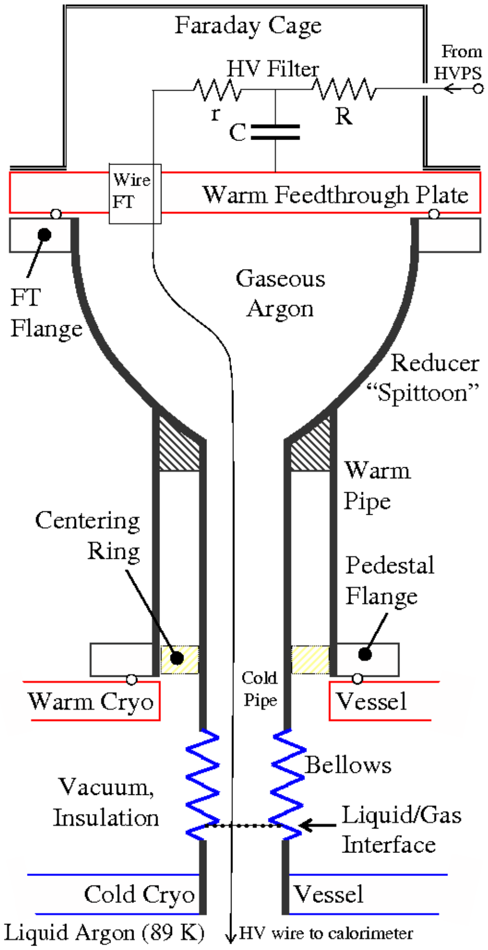

Figure 4.1: Conceptual drawing of the ATLAS LAr high voltage feedthrough (HVFT) port and the HV filters. The HVFT ports are located near the top of the LAr cryostats. Not to scale.

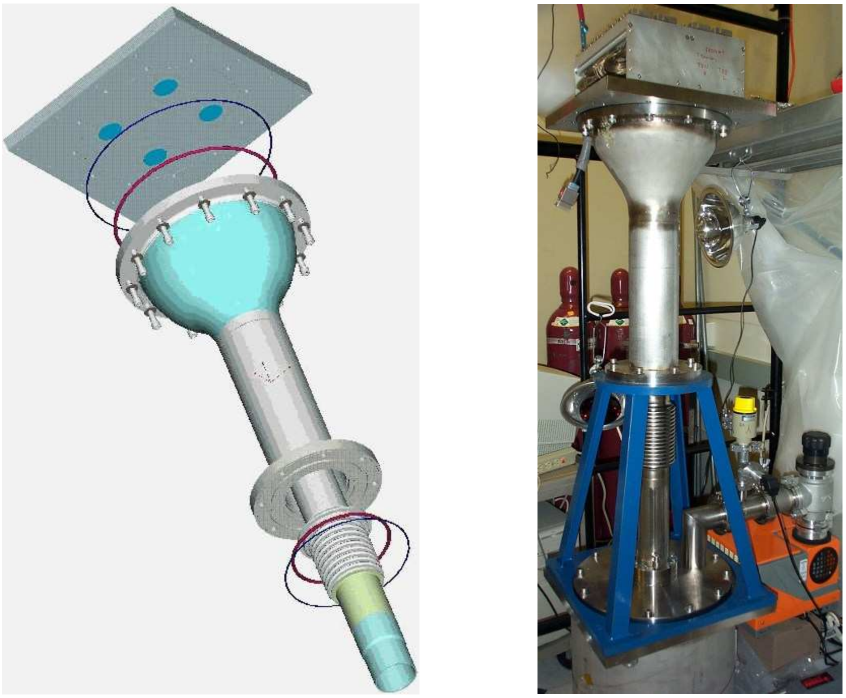

Figure 4.2: Mechanical design of a HV feedthrough port (left). The four holes on the FT plate accommodate the four wire feedthroughs of 210 wires each. Also shown are the O-rings and RF gaskets. The leak testing at Stony Brook of a completed HVFT port mounted on a test vessel which contains the HV wire bundle (right).

Component	Height	Thickness	Inner ø	Outer ø	Stain. steel type
Bellows	140	0.3 x 2	80.0	101.0	331
Cold pipe	424 (ab)	1.6	73.0	76.2	304L
Warm pipe	333.5	2.11	110.1	114.3	304L/316L
Reducer	178	2.1 to 3.4	110.1 to 266.3	114.3 to 271.3	304L
Plate		25			304L

Table 4.1: Dimensions (mm) of HVFT port components (ab means above bellows).

barrel adapter (barrel), see Fig. 4.3. A PEEK (Poly-Ether-Ether-Ketone) pipe insulator is slid on the long cuff (which provides centering support of the cold pipe within the warm pipe), with a weld flange capping the top end of the cold pipe and bellows assembly. On the bottom a temporary test flange is welded. This end is cut to size at the time of installation, when the HVFT port is welded to an aluminum-to-stainless steel transition piece on the cold cryostat.

The bellows has a two-ply structure and consists of two individual bellows, one inside the other. The thickness of each ply is 0.3 mm. The bellows are guaranteed to survive more than 1000 cooldown cycles, and can operate in LAr and in vacuum.

The warm components (the weld flange, the reducer, the warm pipe, and the pedestal flange) are welded together with the cold assembly to form the completed HVFT unit. The various pieces were all machined at Stony Brook University, while all welding was executed by a Code-certified welder at BNL.

In addition to the weld joints, there are several O-ring joints in each HVFT port structure: at the pedestal flange between the HVFT port and the cryostat vessel, and at the joint between the FT transition flange and the FT plate. Both these flanges contain an O-ring as well as a RF gasket. Since electrical noise considerations require that the HVFT port be an integral part of the Faraday cage with the cryostat, a CuBe wire mesh RF gasket (Laird Technologies part no. 8300-0225-40) is used to ensure a good electrical connection. The O-ring material is EPDM rubber (Ethylene Propylene Diene Monomer). Finally, each 210-wire FT is sealed in the FT plate with a nitrile O-ring made of BUNA-N (Acrylonitrile Butadiene Terpolymer).

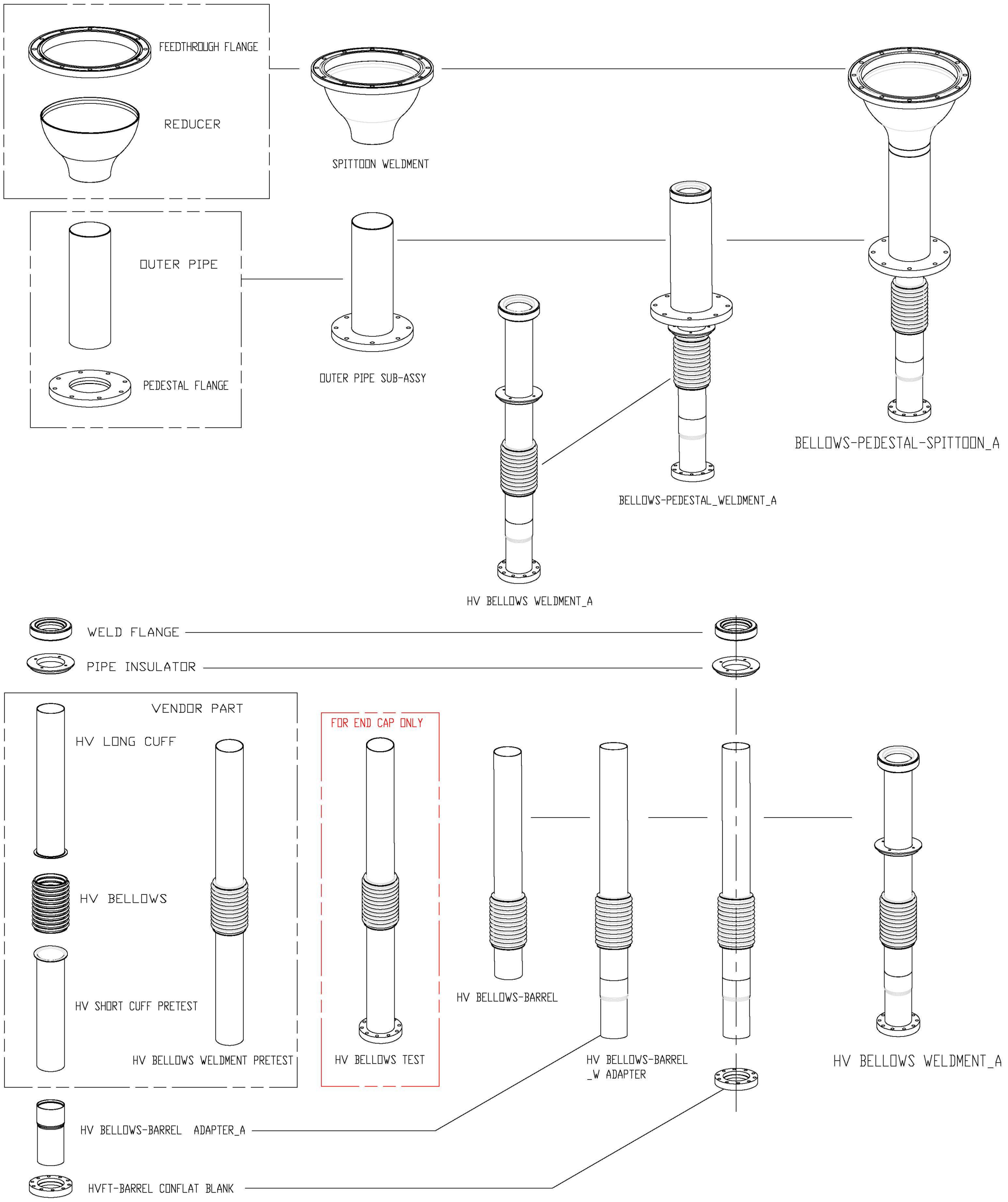

Figure 4.3: Assembly tree of a HVFT port: cold pipe and bellows (below). Assembly of the warm parts: pedestal, outer pipe, reducer; and the final port assembly (above).

Figure 4.4: “Squirm” test of a bellows unit. Squirm occured at 190 psi (13 atm).

4.3.1 Performance and Tests

In the HVFT port there are two dominant sources of heat leaks into the LAr: the cold pipe and the constantan-PEEK HV wire bundle. The heat flow along the cold wall is mostly determined by the stainless steel bellows (having the smallest wall thickness and therefore the smallest heat conduction) and amounts to 0.8 W. The LAr is calculated to rise inside the bellows to a level of a few centimeters above the cold end. The heat flow along the HV wire bundle is 0.4 W. So the total heat flow is about 1.2 W, making it unnecessary to heat the FT plate unless a major gas leak occurs in one of the HVFT seals causing the LAr level to rise. Thus, in order to control the temperature and heat the FT plate if necessary, two thermocouple pairs and four resistive heaters are mounted on the FT plate. Temperature readout and heater power wires are filtered and lead to the ATLAS cryogenics control room.

Several tests were performed to check the weldments and the O-ring seals. A FT plate outfitted with four 210-wire FTs and bolted to the reducer was tested and found to withstand an absolute pressure $P_{\text{abs}} \geq 68$ bar without leakage and deformation.

Given the highly sensitive role they have in the HVFT mechanics, the bellows were tested separately at BNL to test the “squirm”-limit (sideways bulging instability that could destroy the bellows), see Fig. 4.4. The critical pressure for squirm, P_{cr}, was found as $P_{\text{cr}} > 4 \times P_{\text{op}}$, where P_{op} is the nominal operating pressure of 2.8 bar. In addition, all HVFT port assemblies were Code leak-tested at 125% of rated pressure.

In order to ensure the vacuum integrity of the high voltage FTs, every FT port, each containing four WFTs, was required to have a leak rate below 10^{-9} STD cc/s of Helium at standard temperature and pressure. Measurements were conducted at Stony Brook. The expected permeation rate L in STD cc/s through the seal is approximated by the following formula[2] in metric units:

$$L \approx 0.123 \times \mathcal{P} \times ID \times \triangle P \times Q \times (1 - S)^2$$

where $\mathcal{P}$ is the specific permeation (STD cc/s$\times$cm/cm^{2}bar) of the gas through the seal at the anticipated temperature, ID (cm) the inner diameter of the O-ring, $\triangle P$ (bar) is the pressure difference across the seal, Q the quality factor of the seal (about 1.25 for a non-lubricated O-ring at 30% squeeze), and S is the squeeze factor expressed as a fraction. We calculated a helium permeation rate $L_{\mathrm{He}} = (4-6)\times 10^{-6}$ STD cc/s for a nitrile seal, and $L_{\mathrm{He}} = 15\times 10^{-6}$ STD cc/s for EPDM.

Gas	Nitrile(BUNA-N)	Butyl	EPDM	Butadiene
He	(5.2-8)$\times10^{-8}$	(5.2-8)$\times10^{-8}$	20$\times10^{-8}$	12$\times10^{-8}$
Ar	(1.6-3.9)$\times10^{-8}$	1.2$\times10^{-8}$	(11-23)$\times10^{-8}$	NA
O_2	(0.7-6)$\times10^{-8}$	(1.0-1.3)$\times10^{-8}$	NA	(8-14)$\times10^{-8}$
H_2O	760$\times10^{-8}$	(30-150)$\times10^{-8}$	NA	NA

Table 4.2: Published specific permeations [STD cc/s$\times$cm/cm^2/bar] for various O-ring materials at temperatures of $20 - 30^o$C.

Leak tests of each completed HVFT port assembly, including the WFTs, were performed. For these leakage measurements, the HVFT port was continuously pumped out for two-to-five days to bring the pressure below 4 mTorr. An oil-free membrane roughing pump to back up a high vacuum molecular turbo pump was used. The main pump was then shut off and the helium leak detector (incorporating its own diffusion pump) switched onto the system. Helium background, as measured with the leak detector, stabilized in ~ 1 hr at about $(1.4 \pm 0.2) \times 10^{-9}$ STD cc/s.

The leak rates of both types of O-ring seals used were measured separately by enclosing them in bags that were filled with Helium. For the wire FTs with the small nitrile O-rings, no Helium was measured above the background 1.3×10^{-9} STD cc/s for 5 minutes. Next, helium was injected in a second bag

---

[2] NASA, `www.nasa.gov/offices/oce/llis/0674.html`

enveloping the large EPDM seal between the FT plate and FT flange. Starting after 1-2 minutes, a slow and steadily accelerating rise of helium leakage at a rate of $(0.5 - 1) \times 10^{-9}$ STD cc/s per minute was observed. After 15 minutes of flow around the EPDM seal, the helium supply was shut off and the bag removed. About 5 minutes later the measured leak rate was still increasing and did not reach a plateau during the observation period. At the end of observations, the Helium leak rate was $\sim 6 \times 10^{-8}$ STD cc/s and still rising at 1×10^{-8} STD cc/s per minute.

The delayed onset of Helium detection is in agreement with slow permeation through the large EPDM seal in the FT plate (see Table 4.2). The observed background-subtracted permeation of this seal is 1×10^{-9} STD cc/s after 5 minutes. The smaller seals of the WFTs did not show signs of permeation (less than 2×10^{-10} STD cc/s for about 5 minutes); for these seals we expect a permeation rate one order of magnitude smaller (a factor two less because of size, and probably a factor four less because of the lower specific permeation of Buna-N compared to EPDM).

A second type of test, performed on all HVFT ports, involved "spraying" helium only near the various seals as is customarily done for UHV seal testing. Helium was sprayed (from a helium line ending in a hollow needle) at a rate of ~ 10 mL/s (~ 5 bubbles/s as measured by injecting it in a fluid). The needle was passed along the seals at a speed of ~ 2 cm/s. For this test, the helium leak detector was connected at the output of the turbo-molecular pump and also served as roughing pump. Measurements started after a baseline/background plateau of 0.45×10^{-9} STD cc/s was reached after ~ 0.5 hr of pumping. No increase of the helium leak rate was observed during the measurement, which lasted several minutes. In an attempt to confirm the permeation effect observed in the earlier test, helium was finally injected at high flow rate in a bag enveloping all seals. A steady increase was observed, as in the first test, starting after 4-5 minutes, see Fig. 4.5.

Although helium permeation through the HVFT seals is significant, no measurable leaks were detected in any of the FT plates. The expected O_2 permeation rate, assuming $P = 5 \times 10^{-8}$ and $\triangle P = 0.2$ atm, equals $LO_2 \leq 8.8 \times 10^{-7}$ STD cc/s $= 8.8 \times 10^{-7}/22413$ cc/mol $= 3.9 \times 10^{-11}$ mol of O_2/s $= 1.2 \times 10^{-3}$ mol of O_2/yr, again for the Nitrile seal. For a total LAr load of the half-barrel of 30 tonnes $= 3 \times 10^7$ g /40 g/mol $= 7.5 \times 10^5$ mol of Ar, this represents a pollution of ~ 1.6 ppb or less of O_2 per year. Oxygen diffusion into the LAr (at an inside pressure of ~ 3.5 atm) will be several orders of magnitude smaller than the helium permeation rate (with vacuum inside the HVFT), and is thus not a concern. Moreover, because the pressure is reversed in ATLAS, the rate of diffusion (not the rate of permeation) of oxygen across

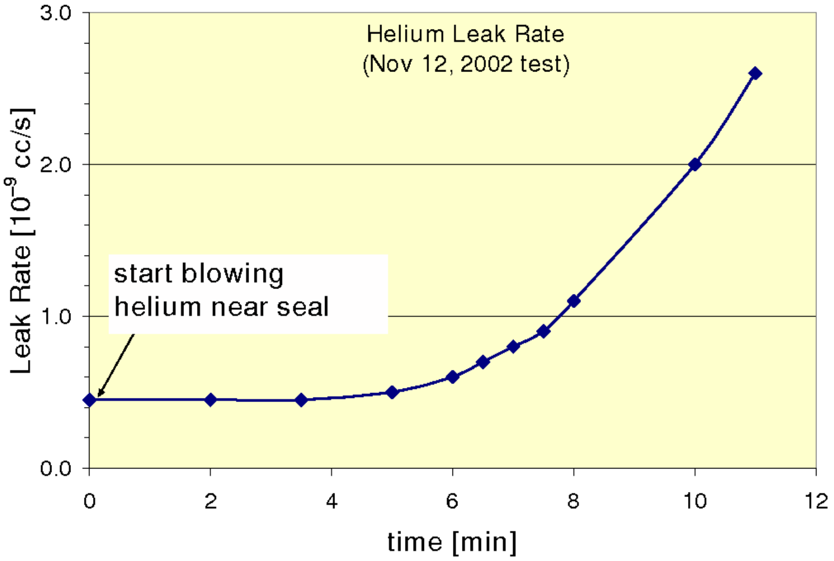

Figure 4.5: The measured helium leak rate in a HVFT port (results of second test, see text).

the seals is a more accurate measurement of pollution and is several orders of magnitude lower.

4.3.2 The HV wire

Special HV wire is used to carry each high voltage channel through the FT plate. The characteristics of this wire are shown in Table 4.3. The wire has a solid constantan conductor and an extruded PEEK insulator. We chose a constantan conductor because of its relatively low thermal conductivity, thus reducing the heat leak along the wires. Constantan was favored over stainless steel (an even poorer thermal conductor) because it is relatively easy to solder. PEEK insulation was chosen both because of its very high radiation tolerance and its very high electrical resistance. PEEK can be used throughout the calorimeters, even in the forward region which receives the highest radiation dose. Constantan wire with Kapton insulation was also considered but rejected because of its lower radiation tolerance and because of the possibility that, in principle, its insulation could unravel. All wire used in the construction of the FTs was purchased from HABIA Cable[3].

---

[3] HABIA Cable, `www.habia.se/`

Characteristics	Material/Specifications
Conductor 0.41 mm ø (26 AWG)	constantan (60% Cu, 40% Ni)
Insulator 1.01 mm ø	PEEK (Poly-Ether-Ether-Ketone)
Minimum breakdown voltage	5.0 kVAC (15 kVAC at HABIA)
Radiation tolerance	10^7 Gy (10^9 rad)
Thermal conductivity (constantan)	17 W/m.K (77 K), 22 W/m.K (273 K)
Electrical resistance (constantan)	3.82 Ω/m
Electrical resistivity (PEEK)	$\rho_R \geq 1.7 \times 10^{13} \Omega$.m

Table 4.3: Characteristics of the constantan-PEEK wires produced by HABIA.

Internal and external corona

Corona is the repetitive charging and discharging of electrical conductors at high voltage through a gas or air. In the case that one electrode is an insulated HV wire, the corona current and the UV photons created in the electrical avalanche in the gas may slowly damage the insulation and cause catastrophic breakdown. Several good references exist on corona in wiring systems [23, 24]. Corona has the insidious property that it searches out the weakest part of the insulation and eventually drills a hole in it. The voltage is highest in the gas where the insulation is thinnest around a wire, so that is where the corona will occur. Beginning approximately 100 years ago, extensive studies have been done on the conditions necessary to cause a spark in a gas. It was found experimentally that the sparking voltage is a function of pressure times distance and followed Paschen's Law, see Fig. 4.6. This curve shows that there is a minimum voltage for corona ignition at any separation of the electrodes. For argon gas and air this voltage is respectively about 270 V and 330 V [25] and is sensitive to both temperature and humidity.

As described in Ref. [24], most commercial corona tests are done with alternating current (AC). An AC voltage is applied to the object (considered as a capacitance) under test. The capacitance under test is observed with an oscilloscope through a high-pass filter, designed to filter out the HV AC component of the output signal, while passing the high-frequency corona pulses. In order to avoid internal corona, arising in gas trapped between the conductor and insulation and inside the insulation itself, HV wire manufacturers will try to exclude gas inclusions during the extrusion process. External corona occurs outside the insulation, but both types of corona could, in principle, damage the insulation. HABIA arranged for an outside lab (a swedish national laboratory) to test for internal corona after we noticed, under microscope, an

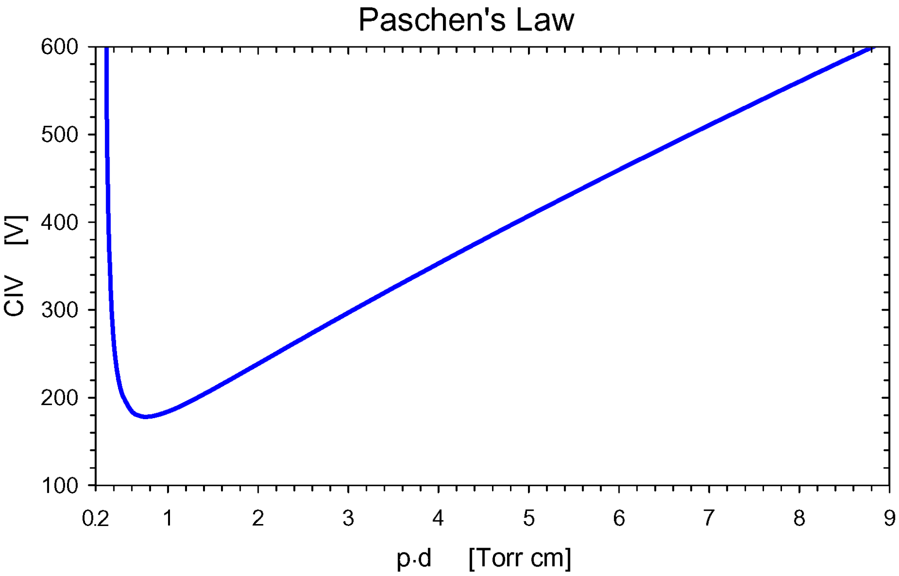

Figure 4.6: Paschen's curve for Ar/Cu.

unusually high number of air bubbles in the insulation of the production cable (compared to the thinner prototype wire which had no bubbles).

In order to obtain corona ignition voltage (CIV) measurements and to compare with those supplied by HABIA, we conducted our own tests using various geometries at NOVACAP[4]. We used 12 m of ATLAS production wire wound on an aluminum mandrel in air. Thus, this test was sensitive to both internal and external corona. Fig. 4.7 shows the CIV as a function of the charge threshold in pC (pC) for a single corona pulse. This curve is consistent with the Paschen minimum of 330 V DC or 233 V RMS for very small single-pulse charges in air (the bubbles in the wire contain air that could not be removed in the extrusion process.) The curve reaches 1 pC at 500 V and increases very rapidly after 800 V. The capacitor industry's standard threshold is 25 pC for the single pulse charge threshold. Corona charge pulses smaller than this value are not considered dangerous because they are observed not to damage capacitors.

Table 4.4 shows the CIV values measured for ATLAS production wire (Bubble PEEK) both by HABIA in Sweden and by us at NOVACAP. For the test results shown, "water" means grounded conducting water (5% salt by weight), "mandrel" means grounded aluminum mandrel in air and "epoxy" means conducting epoxy. It can be inferred from the data that there would be no internal

---

[4] NOVACAP, `www.novacap.com/`

Insulation	Test location	Medium	CIV RMS (V)
Bubble PEEK	Sweden	water	868, 898
Bubble PEEK	NOVACAP	water	740, 770
Bubble PEEK	NOVACAP	mandrel in air	820
Bubble PEEK	NOVACAP	mandrel in epoxy	610
Bubble PEEK	NOVACAP	air (10 cm from ground)	no corona to 3.5 kV

Table 4.4: CIV for ATLAS production wires at $Q_{threshold} = 5$ pC.

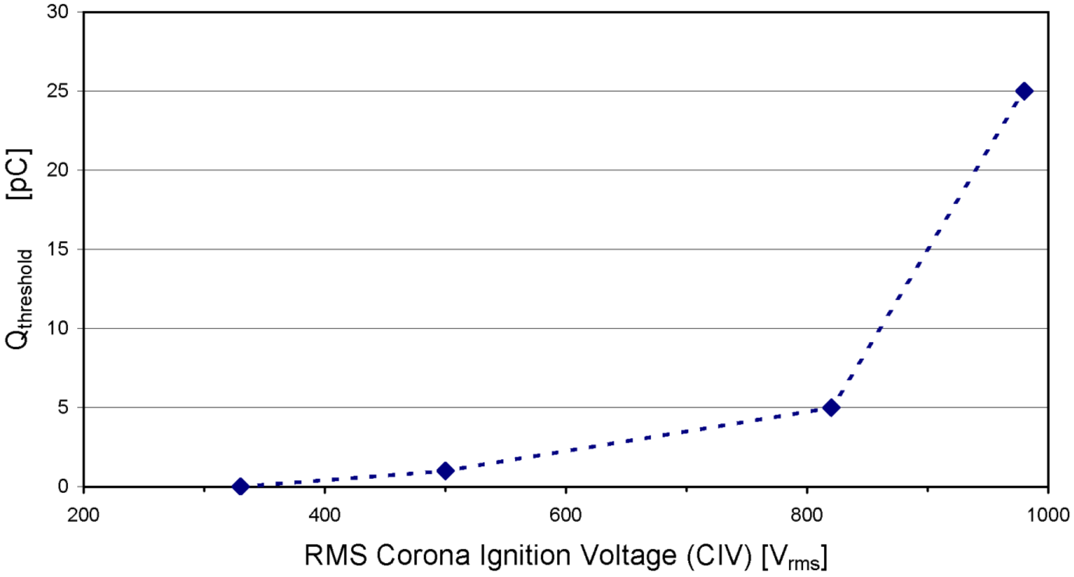

Figure 4.7: Corona charge threshold ($Q_{threshold}$) versus Corona Ignition Voltage (CIV) measured with the HABIA wire wound on a grounded Al cylinder.

corona between adjacent HV wires (assumed to touch) in our high voltage FTs if the voltage difference were less than 740 V × 2 × $\sqrt{2} = 2090$ V. Thus the most likely source of internal corona would come from a channel which is set to 0 V (off or spare), in case all wires have the same polarity. Even if such internal corona does exist, accelerated destructive corona tests (for internal corona) at both NOVACAP and SBU showed that there would be no failure of the insulation.

Assuming an AC corona pulse is as destructive as a DC corona pulse, we accelerated the destruction of our PEEK insulation by a factor

$$A = \tau / \triangle t$$

where $\triangle t$ is 1/120 s (since there are 2 corona pulses per AC cycle, one of each sign) and τ is the DC corona time constant for PEEK. When an unshielded, insulated wire is at a DC high voltage, the surface of the insulator reaches the full voltage due to leakage current through the insulation. Treating the PEEK insulator as a conductor, the capacitance C of the wire and the resistance R between the conductor and the outer surface can be calculated in terms of the bulk resistivity ρ_R, the dielectric constant $K\varepsilon_0$, the inner and outer radii r_i and r_o of the insulator, and the length L of the wire.

$$R = \frac{\rho_R \ln r_o/r_i}{2\pi L} \quad \text{and} \quad C = \frac{2\pi L K\varepsilon_0}{\ln r_o/r_i}$$

Therefore the time constant $\tau = RC = \rho_R K\varepsilon_0$ of the wire is independent of the geometry. This time constant, which is the charging constant of PEEK considered as a conductor, can otherwise be derived on very general grounds from the equation of continuity and Maxwell's equation, respectively

$$\vec{\nabla} \cdot \vec{J} = -\frac{\partial \rho}{\partial t} \quad \text{and} \quad \vec{\nabla} \cdot \vec{E} = \frac{\rho}{K\varepsilon_0}.$$

Using $\vec{J} = \vec{E}/\rho_R$ one finds that the charge density decays exponentially as $\rho = \rho_0 e^{-t/\tau}$, where $\tau = \rho_R K\varepsilon_0$. Hence, using $K = 2.27$ and the minimum value for the resistivity of the wire $\rho_R = 1.72 \times 10^{13}\ \Omega \cdot \mathrm{m}$ (values provided by HABIA) we obtain $\tau = 414$ s and $A \geq 50,000$.

In ATLAS, we separate the wire bundle from the surrounding FT port structure (maintaining a separation of at least 5 mm except at the WFT itself, where the outer wires are within 1 mm of the steel housing). Therefore, the wire-to-wire corona problem is dominant. We ground the outside of the wire bundle inside the LAr, thus draining the surface charge from the PEEK where there is essentially no internal corona (because of the temperature) and no external corona in the liquid. The NOVACAP tests including the test with a coil wound on a mandrel in air, indicate that internal corona and external corona behave in a similar manner. But these tests are not definitive because they were performed in air rather than gaseous argon.

The NOVACAP tests conducted at 1.77 kV ($2.5\ \mathrm{kV}/\sqrt{2}$) for 68 hr (384 years DC equivalent) showed no damage to the coil. It is interesting to note that the corona actually stopped after about 5 hr, phenomenon confirmed by NOVACAP in later tests. During the Stony Brook University tests, a coil in conducting water was undamaged after 20.2 hr at 1.77 kVAC (115 year DC equivalent in ATLAS). In addition, a coil wound on a grounded aluminum mandrel survived undamaged in air for 84.3 hr at 1.77 kVAC (481 year DC equivalent) and in gaseous argon for 56 hr (319 year DC equivalent). This latter test shows that the FT wires will not be damaged by either internal or external corona over the lifetime of the ATLAS experiment.

4.3.3 The Wire Feedthroughs

Wire FTs (WFTs), containing 210-220 wires per WFT, were made by the Douglas Electrical Components (DEC)[5]. DEC using a proprietary method to space and "pot" the wires in a stainless steel cylindrical housing of 1338 mm^2 cross sectional area. Inside the potting, the PEEK insulation is stripped over 1-2 cm to obtain a vacuum seal by direct adhesion between potting epoxy and the solid constantan HV conductor. Four WFTs are mounted in holes in the FT plate of HVFT port. These non-cryogenic WFTs provide the required wire density and have a rated wire-to-wire breakdown voltage of 5.0 kV DC. At delivery, the wire bundle on the cold side was up to 10 m long (LAr barrel WFTs), and 0.6 m on the warm side. The WFT contained from 105 to 110 wire "loops" (the same wire has both ends on the warm side and is "looped" on the cold side of the WFT). DEC tested every wire loop with all other wire loops grounded before shipping the WFT. DEC also guaranteed that the WFT has a leak rate below 10^{-9}cc/s of He at STP before shipment. The WFT has a radiation tolerance of 400 Gy $= 4 \times 10^4$ rad.

Cleaning the WFTs and wires

An extensive and labor intensive cleaning process, which lasted about two months, took place upon reception of the WFTs from DEC. This cleaning process began with a visual and microscopic inspection of the entry and exit areas of each WFT to check for nicks, cuts, sharp bends and debris, the latter of which are removed by a first water bath. Then, each WFT was immersed in an ultrasonic bath of water and an all-purpose detergent[6] at 50^oC for at least 2 hr. All wire surfaces were cleaned, using a minimum of 10 brush stokes, in a third bath made of a mixture of water, detergent and ethyl-alcohol. In the following stage, each WFT was soaked for at least 2 hr in a mixture containing water and 33% ethyl-alcohol. Finally, all wires were individually cleaned by hand using soft, highly absorbent and non-abrasive wipes (an average of 4 wipes per wire), and 200 proof ethyl-alcohol. This was done until no visible residue is left on the wipes. WFTs were handled exclusively inside a clean room.

---

[5] Douglas Electrical Components (formerly Douglas Engineering Company), `www.douglaselectrical.com`.

[6] Product no. 0037, `www.zepmfg.com`.

The wire bundles, connectors, and the HV backplane

Wiring diagrams were made showing the detailed routing path and the corresponding wire-length calculation (including 0.2 m extra for safety) for all HV wires as function of HVFT position and calorimeter destination patch panel. These length calculations were extensively checked. Bundle lengths vary between 1.7 m and 8.3 m. Before making bundles, all identified bad wires were cut and removed. The wires on the warm side were cut to a length of 18 cm and female REDEL[7] contact pins were crimped on the conductors. The crimp connections are protected with a HV lacquer[8] and a shrink tube[9]. Then, following the wiring plan and starting from the cold side of the WFT, separate wire bundles of 4-8 wires were formed over the full wire length on a 10 m long bundling platform (netted surface to allow filtered air to pass through from above) and identified with label ties. In bundles that carry negative HV (for purity monitors and for the End Calorimeter Presampler), grounded spare ("shield") wires are used to separate wires carrying negative voltage from the majority of wires carrying positive HV inside the WFT and the Argon gas column.

A typical WFT contains about 50 bundles, of four wires each. Because of its high radiation resistance of up to 100 Mrad, only Tefzel cable ties[10] were used for all bundling operations. After bundle formation, the bundles were cut to size (±1 cm) and connected with the cold connectors[11]. Grounding a finished bundle on the cold side, its corresponding wire contacts on the warm side were located using a powered LED pen, and inserted into the LEMO/REDEL chassis connector block.

The wire bundles were carefully guided through the appropriate FT plate holes and the WFTs were bolted in place. The HV Backplane is mounted on the FT plate. The warm REDEL HV connectors are mounted on the 56-HP-wide (1 HP = 5.08 mm) backplane, constructed using EURO-standard

---

[7] LEMO/REDEL, contacts type no. ERA.05.403.ZLL1 for 50-contact rectangular chassis connector type no. SLA.H51.LLZG

[8] HumiSeal, `www.humiseal.com`, lacquer type 1B73.

[9] Kynar; polyvinylidene-difluoride, `cableorganizer.com/heat-shrink/`

[10] Tefzel; ETFE - ethylene-tetrafluoroethylene,
`www2.dupont.com/Teflon_Industrial/en_US/assets/downloads/h96518.pdf`.

[11] Single-contact custom design in PEEK material for LAL, 91405 Orsay, France, by ATI Electronique (Alliance Technique Industrielle), `www.ati-electronique.fr`, used for most calorimeters; and 7-contact (4 used) glass-filled polyester connector by AMP/Tyco Electronics, USA, `www.tycoelectronics.com`, part no. 1-87175-5, used for the hadronic End Calorimeters.

hardware, as shown in Fig. 4.9. Before leaving the clean room, to prepare the wires for shipment to CERN, the bundles on the cold side were wrapped with protective plastic cling wrap to form a single HV bundle. This bundle was threaded through a PEEK spacer ring (that centers the bundle in the throat of the metal reducer of the HVFT port), looped and attached to a cage supported by the FT plate, and the whole was bagged in plastic for mechanical and dirt protection.

The FT plate, with HV backplane on top and the cold HV bundle below, was then ready for shipping and installation in the HVFT port on the calorimeter cryostat.

Tests and repair procedures

As an integral part of the quality control of the HVFTs, each WFT was inspected for nicks, cuts, debris and sharp bends, and a HV test was performed upon reception. For this test, the WFT was immersed in water at ground potential. We applied 4.8 kV to each wire loop, one at a time, while keeping all others at ground. This test discovered shorts to adjacent wires or housing and breaks in the wire insulation of the wires on the warm and cold sides. On average, two shorted (i.e. current > 10 nA) wire loops per WFT were found this way. These loops were cut and the faulty wires were identified and labeled on both cold and warm side of the WFT. During bundling, the faulty wires were removed.

A second, more sensitive and detailed HV test was performed on the WFT at the final stage of production, after wires were cleaned, bundled, and connectorized on both ends. For this test the cryostat side of the wire bundle was enveloped in a Plexiglass tube filled with Argon gas and the filter side was bagged in air of 60% relative humidity. During the final test of the first WFTs, a large number of breakdowns (~ 10 wires per WFT or $\sim 5\%$ of total) were found. A closer inspection of the WFTs showed that failing wires are mostly located around the circumference of a given WFT bundle and near the rim of the stainless steel housing. This inspection also showed cracks in the potting epoxy near the metal housing rim and around the perimeter of some wires, with damage to the PEEK insulation, see Fig. 4.8. The failures were most likely caused by frequent handling of the WFTs and wire bundles during manufacture at DEC and later cleaning and bundling operations at SBU. Details of WFT construction (wires exiting close to the metal housing, poor epoxy-PEEK adhesion, excessive degassing, etc.) may have contributed as well.

A repair procedure was put in place because the number of failures was

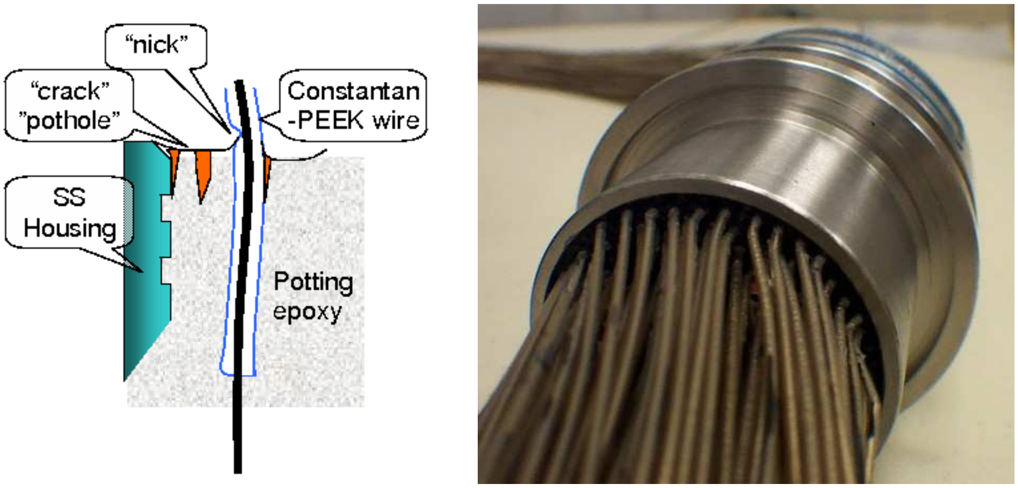

Figure 4.8: An illustration of Wire Feedthrough faults (left). Right: wires exiting a WFT on the cold side, showing the high-density 216-wire HV bundle.

too large to be accommodated by using spare wires. The solution was to re-pot both surfaces of the WFTs in-house with a non-conducting epoxy under vacuum (0.05 atm). Extensive tests of six candidate epoxies led to the choice of the Tra-Bond-2115[12]. This epoxy has a low viscosity (250 cps at 25^0C) and a good dielectric strength (6.0 kV). In tests it demonstrated very good adhesion to the original WFT potting epoxy as well as excellent adhesion to the PEEK insulation of the wires. Tra-Bond-2115 was also tested for use in the ATLAS TRT and found to have good mechanical stability and low pollution potential to LAr. Subsequent detailed HV tests of the WFTs at 3.0 kV showed very few remaining failures: about 2 wires per WFT had > 2 nA (the sensitivity limit of our HV power supply[13]) to ground. Remaining failures were all internal to the WFT, and such wires were replaced by spare wires in the WFT.

4.4 HV RC filters

The HV RC filters are designed for the purpose of reducing noise from the HV power supplies and EM pick-up to below 1 $\mathrm{mV_{pp}}$ (peak-to-peak) at frequencies much below the bunch-turn frequency $(100\ \mu\mathrm{s})^{-1}$, and to below 1 $\mu\mathrm{V_{pp}}$ at signal frequency $(25\text{-}100\ \mathrm{ns})^{-1}$. Filters have to also smooth out

---

[12] TRA-CON, `www.tra-con.com/products/tpb.asp?product=2115`.

[13] T. Droege, Fermi National Accelerator Laboratory, FERMILAB-TM-0527-A, 1975.

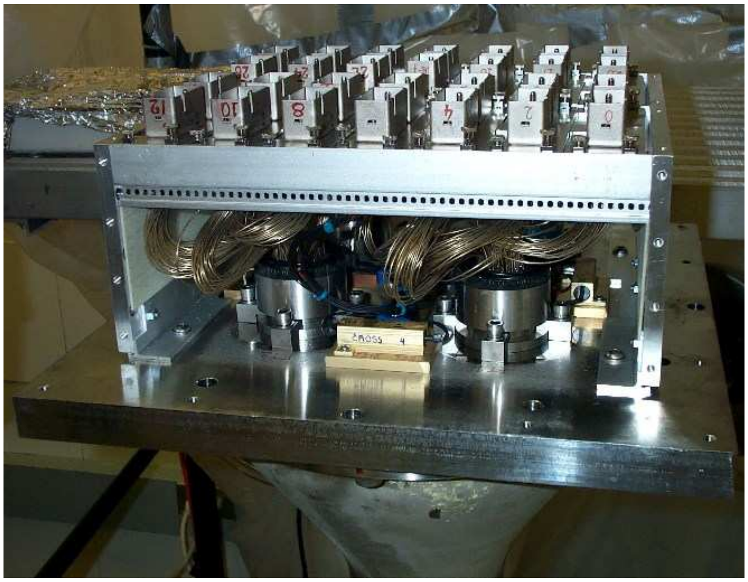

Figure 4.9: View of a FT plate with WFTs, bolted on the HVFT reducer flange. In the foreground one of four heater resistors is seen. The HV backplane with four rows of seven REDEL multi-contact HV connectors is mounted over the FT plate.

current draw fluctuations due to large showers (on the 100 ns time scale) and bunch-train patterns (100 ns to 100 μs). Cross talk between HV leads to sub detector elements is not considered a problem. First, fluctuations in current drawn by an element are reduced by filtering at the patch panels and on the modules: the shielding of cable harnesses serves as a distributed capacitance, and several resistors of 1 MΩ are in series to the calorimeter pads. Second, interline capacitance is about 2 pF/m for wires spaced by 4 mm. The cross talk percentage then roughly equals 30 pF divided by the 27 nF of the filter capacitance to ground, yielding a factor 1000 reduction.

Because the HV bundles from groups of calorimeter cells are redistributed over different HV power supplies (HVPS) such as to provide operational redundancy (e.g. each half of a LAr gap is powered by a different HVPS), the HV backplane provides a patch-panel function as well as a modular connection to HV filters. Moreover, spare channels needed to replace wires broken during calorimeter installation or to provide separate HV powering to "weak" calorimeter cells discovered during calorimeter module construction and testing, are switched in readily by moving contact pins on the backplane. For further compatibility, all warm HV connectors in the LAr system are of the same type LEMO/REDEL 50 × 3 kV (32 channels used per connector).

4.4.1 The HV filter module

The HV lines for each FT port are distributed over 12 to 14 HV filter modules of 64 HV filters each. The module is made of a motherboard on which four daughter boards reside mounted at right angles, each with 16 filter sections. The module dimensions follow the EURO standard: 3U high (5.25 in.) × 8HP wide × 165 mm deep, and use EURO hardware. Besides serving as mechanical supports for the filter cards, the motherboards also serve as a low-inductance ground plane via grounding card guides[14] in the filter crate.

As shown Fig. 4.10, the filters are mounted in a very tight configuration. The filter circuits are separated from each other by thin sheets of Mylar[15] mounted in slots between neighboring circuits. For the required flexibility, the HV wire used was multi-strand tin-plated copper with polyethylene insulation (the same wire as in the multi-conductor HV cables for ATLAS). Special care was taken in the soldering (avoiding all sharp points) and intensive ultrasonic cleaning was performed to minimize surface conduction. Mother boards, card guides and grounding rims are gold-plated, and RF gaskets are used on grounding connections and around front panels in order to provide shielding and a low-inductance ground path for the filters.

Each RC filter is made of a 27 nF, 5 kV multilayer TiO_2 class X7R ceramic encapsulated radial-lead capacitor and two 1% 0.5 W carbon resistors (a small "blocking" resistor and the main filter resistor) whose values are detector specific. The resistors were tested to remain stable under over-current conditions (0.9 W for 1 week), and after repetitive charge pulses (0.2 Hz, 2 kV, 10 μF for 24 hr). The ATLAS LAr HV filters require nearly 5000 HV capacitors. The reliability of the filter capacitors is a concern, because access for repair/replacement will only be possible once per year during a shutdown. If a capacitor shorts to ground, the corresponding HV channel becomes unusable. Therefore, in order to obtain superior reliability, we use the same, reliability-tested, type of capacitor everywhere. The filter capacitors were purchased from NOVACAP[16]. NOVACAP tested all capacitors at 6 kV and 125 ^{o}C for 100 hr, in accordance with the MIL-PRF-49467A protocol. From the results of these tests and derating with voltage, we extrapolate a failure rate of less than 1 failure per 10 years of operation for the entire calorimeter.

---

[14] Ground-R-Guide, Unitrack Industries Inc., `www.unitrackind.com`.

[15] Mylar by DuPont, `www2.dupont.com/Products/en_RU/Mylar_en.html`.

[16] NOVACAP, part no. 6560B273M502LEH, `www.novacap.com`.

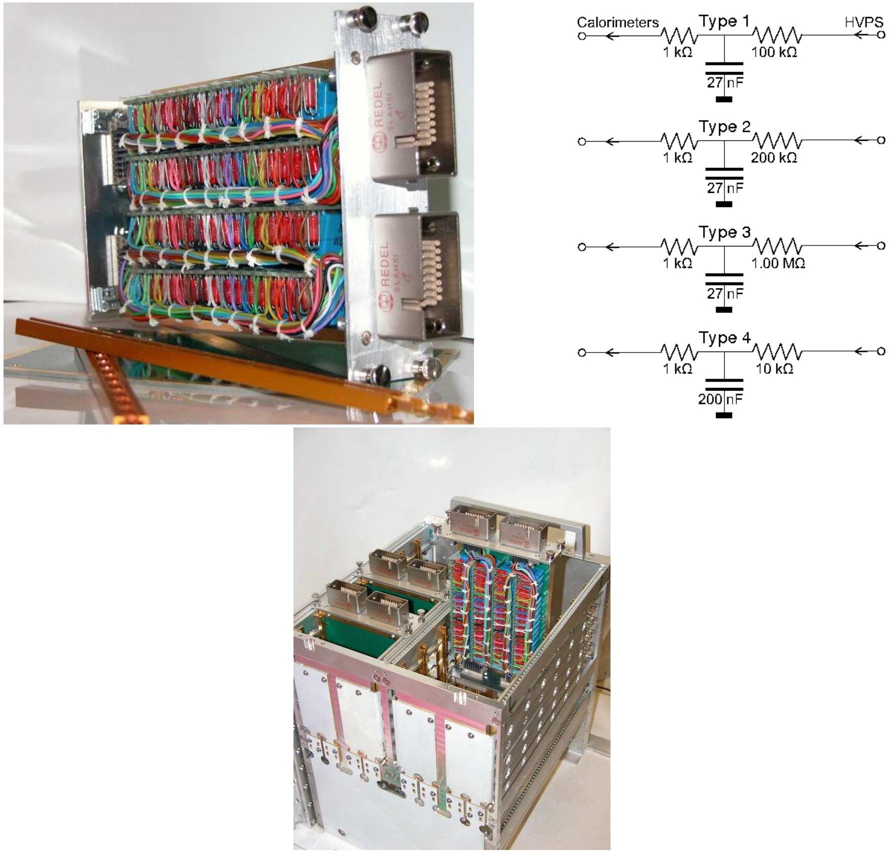

Figure 4.10: Left: a filter module showing the four daughter boards with 16 rCR filter circuits each. The grounding cover is removed, and two Ground-R-Guides card guides are shown in the foreground. Middle: arrangement and component values of the four types of HV filters: Type 1 for EM calorimeters, Type 2 for Preshowers and the Hadronic Calorimeters, Type 3 for the Forward calorimeters, and Type 4 for the LAr Purity monitors. Right: HV filter crate with three filter modules mounted on a HV backplane and without the shielding side panels in place. The grounding strips (left side of photograph at the “bottom” of the crate) and the ground planes leading from the strips to the FT plate (right-front side of photograph and at the side of the crate) are clearly visible.

The radiation environment of the filter capacitors in ATLAS is at the level of a total maximum integrated dose of 50 kRad and 1×10^{13} neutrons/cm^2. This includes a safety factor of 2 to 5. One filter module prototype (64 capacitors) was tested in CERI (France). The module, positioned 80 cm from the source, received a total dose of 5 $\times10^{12}$ neutrons/cm^2 of 6 MeV while at 5.0 kV. No breakdown was observed, and the total leakage current (80 ± 30 nA before irradiation) was 50 ± 20 nA after irradiation. We have not found any data or experiences of multilayered capacitor failures caused by irradiation in the MIL/AEI literature.

The completed filter boards were extensively tested by applying 3.5 kV and ground to alternating filter sections. All individual filter sections of the board, as well as the combined HV input and ground lines were monitored by a capacitively coupled oscilloscope and by nA current meters. The measurements were performed inside a Faraday cage for greatest sensitivity. It was observed that for good boards the leakage current per daughter board decreases to below 20 nA and that the rate of charge pulses rapidly decreases within a few minutes. Filter boards were accepted if they exhibited a discharge rate below 15 pulses/3 mins, where a charge pulse is defined to have 1 pC or more; at this level, the long-term polarization of the X7R dielectric dominates and is indistinguishable from discharges. The 1 kV capacitors for type 4 filters were tested at 800 V.

Filter modules serve HV channels of similar voltage and polarity. Four different types of filter modules, see Fig. 4.10, are used to accommodate the different subsystems in the LAr. Module types 1, 2 and 3 have 27 nF 5 kV capacitors. The choice of the filter resistor value (R) depends on the expected current draw in the part of the calorimeter supplied by the HV channel, and is a compromise between best noise rejection and minimum voltage droop across the resistor. With R = 200 kΩ the rejection is 6×10^{-7} for 50 MHz noise. Two pairs of LEMO/REDEL connectors are used on the front panel (female) and the back panel (male) of each filter module and have the exact same pin-out as the female REDEL connectors on the HV backplane. As on the backplane, 32 out of 51 pins in each connector are used. On the front panel, the unused central row of contact holes in the connector is used for interlock purposes to ensure proper routing to the HVPSs. This arrangement permits easy exchange of filter modules.

In addition to the filter modules, each feedthrough crate also contains a heater module. The heater module filters the currents to four resitive heaters and the signals from two thermocouples which are mounted on the FT plate.

4.4.2 The HV filter crates

Each filter crate is constructed using EURO-standard hardware and forms a 56-HP wide (∼28 cm) by ∼27 cm deep anodized aluminum enclosure whose height extends to about 30 cm above the FT flange. It houses two rows of seven filter modules, which can be exchanged easily. It is mounted on top of the FT flange above the HV backplane, see Fig.4.10. Four aluminum side panels of the crate, together with the RF gaskets on the filter module front panels, form a Faraday cage around the HV lines and filters, while providing access to the HV backplane (by removal of top and/or bottom panels of the crate). Low-inductance grounding contact is provided internally by wide gold-plated Cu strips between the grounding card guides and the FT plate (via a Cu-Be gasket). Shielding is provided by a Faraday cage formed by outer Aluminum panels and the filter module front panels with RF gaskets.

4.5 Installation and Commissioning

Installation of the HVFT port mechanics started early January 2002 on the LAr barrel cryostat. By June of the same year the HVFT ports for the end-cryostats were at CERN and ready for installation. An orbital welder using an autogenous TIG process was used in installation. Each cryostat was vacuum and pressure tested with all HVFT ports, with blank FT plates, in place. Thorough cleaning of the cryostats was performed before calorimeter installation started. Visible dirt was removed and all surfaces wiped down with ethyl alcohol or other appropriate solvents. The remaining part of the installation took place under a protective tent.

The FT plates, with the wire bundle attached to a harness cage and a strain relief near the FT plate were shipped and installed separately at the time of calorimeter insertion at CERN. Scaffolding and a jib crane were used to lift the FT plate and wire bundle to the top of the cryostat. The wire bundles were gradually released from their supporting cage and fed through the FT port, while removing the protective cling wrap. Near the end of insertion, the strain of the cable weight was transferred to attachments points inside the cryostat and the strain relief on the FT plate was removed. At this point the FT plate, the O-ring seal and RF gasket were inspected (and cleaned if needed) and the FT plate was fully lowered and bolted onto the HVFT port flange. Following the wire routing plan, the individual wire bundles were run around the outer perimeter of the cold cryostat vessel until they reach the azimuth of their destination patch panel, fixing the bundles every 20 cm with

Tefzel cable hooks and ties. From the destination azimuth the bundles run radially inward to the module patch panels. The cold HV connectors (ATI) remained bagged and temporarily fixed.

After routing and before the final connection of the HV connectors to the calorimeter cells, a last HV test was performed in which each HV contact on the HV backplane was put at 3 kV with all other contacts grounded. The feedthrough pipe was bagged from below and filled with argon gas. A final prototype ISEG 32-channel HV power supply controlled by a laptop PC was used to perform the tests and read currents (10 nA resolution). Spare cables are available to fix HV problems while access in the cryostat is possible. During HV wire routing and calorimeter connection, two HV wires were accidentally damaged and were replaced with spares.

The detailed HV connectivity was tested several times during calorimeter installation and HV hook-up, and no routing mistakes were found. Calorimeter cells which were suspected of showing HV problems during earlier tests, were connected to spare wires that were routed to strategical positions around the circumference for that express purpose; such channels can be supplied with lowered HV if so needed.

Filter crates and filter modules were installed after closing and before the first cooldown of the cryostats. Some failures have been observed and repaired since then. Although all REDEL pin contacts were mechanically tested after insertion, four times a HV contact in a HV back plane or filter module connector was found to have been pushed back. Twice a HV wire break was found at the wire crimp under the backplane, most likely a result of an accidental disturbance before or during the installation of the filter crate. All these failures were successfully repaired. No failures of filter components have been observed at the time of writing, after about 1 year of HV operations.

4.6 Conclusions

High Voltage FTs have been constructed to provide 5040 individual high voltage lines for the ATLAS LAr calorimeters. The non-accessible part of the system is designed to operate without failures for at least 20 years. The failure rate of accessible components (HV filter components) is expected to be less than 1 failure in 10 years.

4.6.1 Acknowledgements

We thank our staff at both Stony Brook and Brookhaven, and our ATLAS collaborators in the LAr group for their help with this effort. We acknowledge the efforts of the late Dr. F. Lobkowicz, who started the design of the ATLAS HVFTs. We thank Dr. H. Braun for helpful discussions and assistance; and Drs. M. Aleksa, L. Hervas, P. Fassnacht, and P. Pailler for their insights and support. This work was partially supported by DOE grant DEFG0292ER40697 and NSF grant PHY0652607.

Chapter 5

Simulation of the Inactive service Material in the Barrel/End-Cap Transition Region of the ATLAS Electromagnetic Calorimeter

5.1 Introduction

This chapter reports on the description and simulation of the inactive Inner Detector (ID) service materials located in the transition region between the barrel and the two end-caps of the ATLAS Electromagnetic (EM) Calorimeter. A precise description of this material, crucial to the reconstruction of simulated electrons and photons in the EM calorimeter, was implemented in the ATLAS software using GeoModel and GEANT4. Detailed simulations show that the amount of ID service materials in the transition region is compatible to that described in the Calorimeter Performance Technical Design Report, and therefore does not impact the resolution of both electrons and photons beyond what was predicted.

The complexity of the ATLAS detector and of the physics events produced by LHC collisions at an unprecedented 14 TeV center of mass energy require a detector simulation program able to very accurately model both physics and detector response. The ATLAS simulation program must meet stringent requirements. These include the ability to account for event pile-up, radiation background, secondary interactions and decays, detector occupancy, and background noise. The simulation program must be flexible in the design of its components to accommodate changes, such as misalignments due to sagging distortions. Therefore, the simulation program must be accurate enough in the description of the detector geometry but also fast in order to minimize CPU time. The simulation of the inactive material between the barrel and end-caps of the EM calorimeter is one area where this compromise between accuracy and speed is essential.

5.2 Passage of particles through matter

High-energy electrons, positrons, and photons traversing matter interact through well-known electromagnetic processes described by Quantum Electrodynamics: ionization, bremsstrahlung and pair-production. These main processes are at the origin of electromagnetic cascades, which in high Z materials produce EM showers. The mean rate of energy loss for moderately relativistic charged particles is given by the Bethe-Bloch relation[29],

$$-\frac{dE}{dx} = Kz^2\frac{Z}{A}\frac{1}{\beta^2}[\frac{1}{2}\ln\frac{2m_ec^2\beta^2\gamma^2T_{max}}{I^2} - \beta^2 - \frac{\delta}{2}]$$

where T_{max} is the maximum kinetic energy imparted to a free electron in a single collision, $\delta(\beta\gamma)$ the density effect correction to ionization energy loss, I the mean excited energy, Z and A are respectively the atomic mass and atomic number of the absorber.

As the energies of electrons and positrons in the shower decrease below a certain critical energy E_c, they dissipate their energy exclusively by ionization and excitation. The critical energy E_c is sometimes defined as the energy at which the electron energy loss rate by bremsstrahlung (linear) is equal to its loss rate by ionization (logarithmic) [29].

5.2.1 Energy loss by electrons and photons

At low energies, electrons and positrons primarily lose energy by ionization, although other processes contribute. The Photoelectric effect is the dominant process for energy loss by photons at low energies, although Compton scattering, Rayleigh scattering, and photonuclear absorption also contribute. The production of e^+e^- pairs becomes the dominant process as the energy increases.

5.2.2 Bremsstrahlung

Bremsstrahlung[30] is the main process governing energy loss of high-energy electrons and positrons when passing through matter (Fig. 5.1). This process, the result of Coulomb interaction with the electric field of the atomic nuclei, is accompanied by a small change (Coulomb scattering) in the direction of the final electron or positron. Electrons and positrons will radiate photons whose energy spectrum falls off as 1/E. In general, the energy carried by the bremsstrahlung photons is a small fraction of the charged particle's except

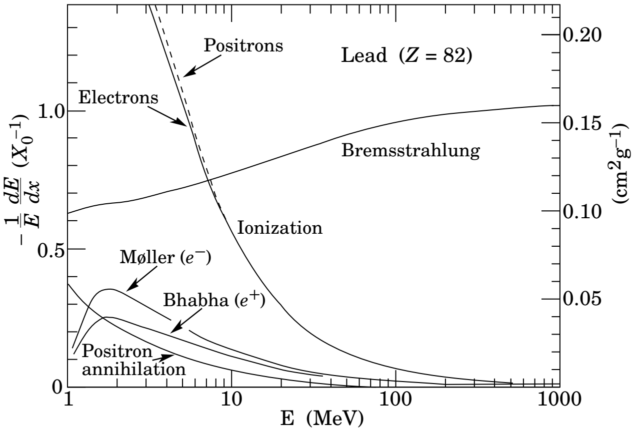

Figure 5.1: Fractional energy loss in lead by electrons and positrons [29].

in the very rare case of hard bremsstrahlung when the entire energy of the charged particle can be emitted as a photon.

5.2.3 e$^+$e$^-$ pair production

At energies greater than twice the electron rest mass, a photon predominantly converts into an electron-positron pair[30]. For reasons of momentum conservation, this is possible only in the presence of the Coulomb field of a nucleus or a charged particle. The cross section for this process rises with energy before reaching an asymptotic value above 1 GeV. Depending on the absorber material, e^+e^- pair production is the dominant process for photon interaction with matter for energies above a certain limit of a few MeV. Below this limit, dominant processes for photons are Compton scattering, Rayleigh scattering and Photoelectric effect (see Fig. 5.2).

5.2.4 Compton and Rayleigh scattering

In Compton scattering[30] an incoming photon scatters off an atomic electron initially at rest. The photon transfers momentum and energy to the electron. Therefore, the scattered photon's frequency is smaller than that of the initial photon. This process, predominant for photons in the energy range from a few hundred KeV to a few MeV, will result in a free electron and a scattered photon. Rayleigh scattering[30] on the other hand can be considered elastic since the energy of the scattered photon is not changed, only its direction is changed. Therefore, Rayleigh scattering only affects the spatial

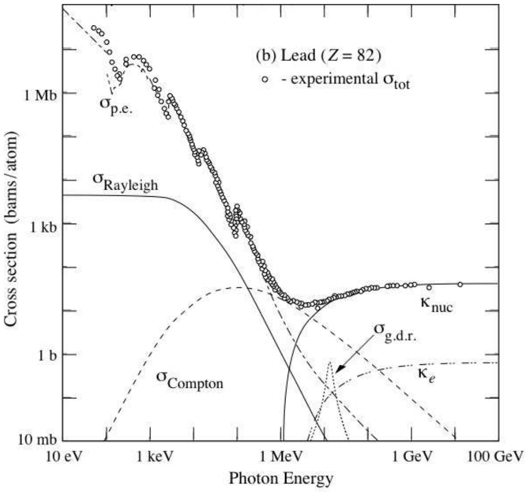

Figure 5.2: Photon interaction cross section in lead as a function of energy [29].

distribution of the energy deposition in the material.

5.2.5 Photoelectric effect

In the photoelectric effect[30], an atom in the material is put in an excited state through the absorption of the incoming photon and the emission of an electron. The atom then returns to the ground state while emitting Auger electrons ("x-rays"). The photoelectric effect is the dominant process for energies below the threshold for Compton or Rayleigh scattering. The cross section for the photoelectric effect, strongly dependent on the electron density in the absorber material, scales as Z^n ($4 \leq n \leq 5$).

5.2.6 Radiation length

Radiation length (X_0), for a specific material, is defined as both the mean distance over which a high-energy electron loses all but 1/e ($\sim 37\%$) of its energy by bremsstrahlung, and 7/9 of the mean free path for an e^+e^- pair production by a high-energy photon. It is clear from this definition that radiation length is an appropriate scale length for describing high-energy electromagnetic cascades. In fact, the scale of longitudinal development of such cascades is directly dependent on the radiation length X_0 of the material.

A good calorimeter must be thick enough in terms of radiation lengths in order to contain and measure the energy of incoming particles accurately. This is accomplished with the use of a high density (high Z) absorber, lead (Pb) in the case of the ATLAS EM calorimeter. Expressing the dimension of the absorber in terms of X_0 has the advantage of eliminating, to first approximation, material-dependent effects. However, it is necessary to minimize the amount of material seen by incoming particles before entering the calorimeter. This is done in order to minimize both the probabilities of EM showers starting too early as well as the amount of "invisible" energy deposits. The radiation length of a given material can be approximated by the following formula:

$$\mathrm{X}_0(\mathrm{g.cm}^{-2}) = \frac{716.4(\mathrm{g.cm}^{-2}) \times \mathrm{A}}{\mathrm{Z}(\mathrm{Z}+1) \times \ln(287/\sqrt{\mathrm{Z}})},$$

where A and Z are respectively the atomic mass ($\mathrm{g.mol}^{-1}$) and the atomic number of the absorber material [29].

5.3 The ATLAS simulation program

A full simulation of physics processes in ATLAS requires the use of three separate software modules that can be run either separately or in sequence under the ATHENA infrastructure [32]. These modules are event generation, detector simulation, and digitization. The simulation software must take into account a large number of physics processes covering the broadest possible range of energies, from the ionization potential (as low as 10 eV) in the active gas of detectors up to the few TeV required to mimic catastrophic energy losses of muons traversing the calorimeters. The software is required to track the particles through the complete ATLAS detector and record the response of all sensitive elements of the various subsystems. Fig. 5.3 shows the various stages of the simulation process and data flow.

5.3.1 Event generation

The first step of the event generation phase is implemented within ATHENA using physics event generators such as PYTHIA [33] and HERWIG [34]. The generators simulate the collisions of various particle species at a given center of mass energy. Generators also simulate particles emerging from the interaction region. A physics event generator produces events (lists of particles) to reflect a particular aspect of physics. The input to the generator is usually in the form of beam energy, tables of decay probabilities, specific particle reactions, and specific final state particles. The output is a list of events which serve as input to the simulation. Each particle is parameterized by particle-type,

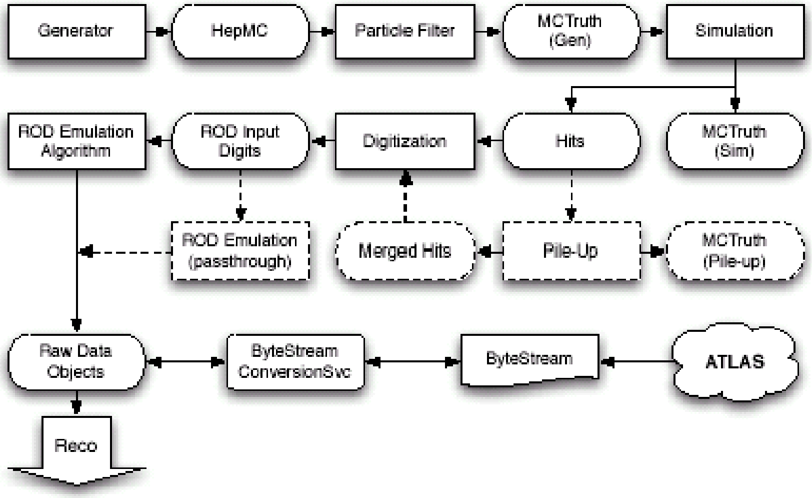

Figure 5.3: The ATLAS simulation data flow shown in the upper branch.

initial vertex, initial and final 4-momentum vectors. Event generators are frequently updated to keep up with the latest theoretical insights. In the case of LHC phenomenology, calculations must include QCD uncertainties due to the parton distribution functions and the hadronisation. Event generators for ATLAS must also take into account details of the beam such as the crossing angle of about 150 μrad between the two proton beams, which will give a global transverse energy boost of $\sim$ 1 GeV.

5.3.2 Detector simulation

Detector simulation is the simulated response of the ATLAS detector to particles generated in the interactions and their decay products. The ATLAS experiment uses a GEANT4-based [27] suite as its simulation tool of choice. The simulation requires a precise geometrical description of the detector components including the materials used in the manufacture, as well as the magnetic field maps. Starting from the interaction point, the particle four-vectors are tracked through sensitive detector elements, represented by geometrical volumes and materials. Dominant electromagnetic processes such as scattering, energy loss (dE/dx), light produced in scintillator tiles and production of secondary particles are adequately simulated over an energy range from 10 KeV to 10 TeV [31]. Data objects representing Monte Carlo truth information from the generators are read by simulation, processed, and recorded as “simulation hits” to be stored or processed by the digitization algorithm.

Simulation performance

The description of the ATLAS geometry in GEANT4 is probably the most critical issue for the detector simulation program, since it must represent the right compromise between accuracy and performance. Most of the CPU time used during simulation goes into the production of detector "simulation hits". In terms of CPU time, one of the most challenging tasks is the simulation of showers in the complex accordion geometry of the EM calorimeter. Recent measurements [39] have shown that the 100 kSI2k-sec[1]per event processing time assumed by the ATLAS Computing Model [38] is largely underestimated. These measurements found that the full simulation of EM particles in the EM Barrel, EM End-Cap and Forward calorimeters necessitate 645 kSI2k-sec per event. The solution to this problem requires the implementation of optimization procedures (such as Fast Shower Parametrization) thus highlighting the importance of using reasonable approximations to describe the inactive ID services in the transition region. Furthermore, inactive materials (cryostats walls, support structures, services, etc.) have been shown to have a direct impact on the physics performance of ATLAS as well, and must be evaluated very carefully in order to account for an "invisible" energy deposited. This report addresses primarily the simulation of the inactive materials, mostly made of ID services and located in the transition regions between the barrel and end-caps of the LAr calorimeter.

5.3.3 Digitization

The digitization step is the final phase, where the deposited energies in the various detector elements are recorded, collected and reprocessed in order to simulate the electronic output from the detector. The digitization stage includes simulation of physics effects specific to each type of detector and of the front-end electronics response and of noise. The output of the digitization is written into Raw Data Objects (RDO) to be used by the reconstruction programs.

---

[1] kSI2k "Kilo-SpecInt 2000" is the output unit of a testing suite and characterizes the computing power. It is correlated with computing speed.

5.4 Simulation of the LAr Calorimeter Barrel/Endcap transition regions

The Liquid Argon (LAr) calorimeter consists of the Electromagnetic Barrel Calorimeter (EMB), the Electromagnetic End-Cap Calorimeter (EMEC), the Hadronic End-Cap Calorimeter (HEC) and the Forward Calorimeter (FCAL). The LAr calorimeter is described in GeoModel as a separate tree of nodes belonging to a general mother volume, the *ATLAS experiment*. One such node is the physical volume called *cryoMotherPhysical* to which belong the various volumes used in the description of the two transition regions (side A and side C).

5.4.1 GeoModel

GeoModel [35] is a geometry kernel used to describe the ATLAS detector geometry. It is a library of geometrical primitives which provides application developers with a complete set of tools and methods for the description of large and complex detector geometries with minimal memory consumption [36]. The geometry description is built by reading primary numbers containing shapes, dimensions, positions, rotations, etc. from a single database which allows for versioning based on ATLAS software releases. This means that GeoModel descriptions are also versioned. The purpose of GeoModel is to support a central store of detector description information that can be accessed by both simulation and reconstruction.

The material geometry consists of a set of classes represented in memory by a graph of nodes consisting of both physical volumes and their properties (name, identifier and transformations) arranged in a tree. The tree structure allows direct and simultaneous access to both volumes and properties during graph traversal. Physical volumes, the main building blocks of the geometry graph, consist of associated logical volumes and sets of child volumes. A logical volume describes only shape and material while a physical volume also holds complete information about its location with respect to the world volume. A transformation in the graph changes the position of the subsequent volume with respect to the parent (mother) volume. The last transformation in a series is always the first to be applied to the child volume. Time-dependent alignments or misalignments can be introduced by simply altering the values of such transformations stored in the relevant nodes.

GeoModel uses various techniques in order to reduce memory consumption. One such technique is shared instancing, where different physical volumes

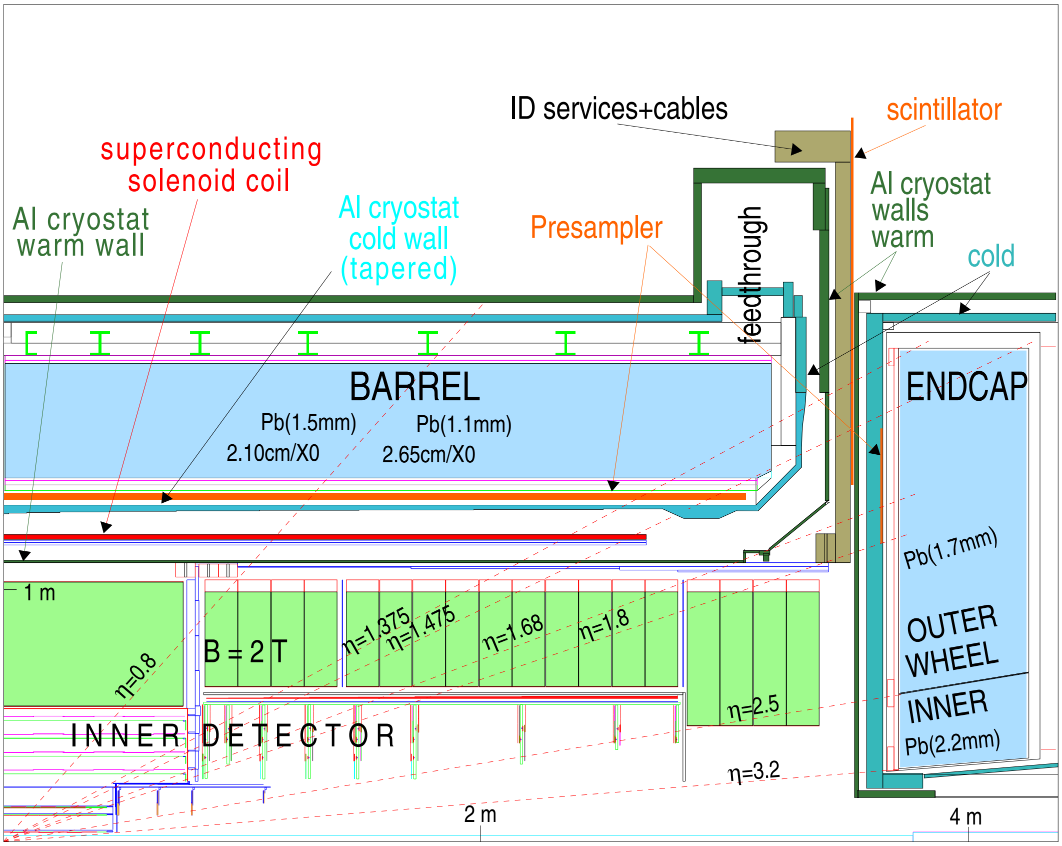

Figure 5.4: A schematic view of the transition region region where ID services are located.

can share the same logical volume and be labeled by the same name and identifier tags, and where transformations can be used more than once in the geometry graph. Other techniques include the use of Serial Denominators to automatically generate name strings for physical volumes (to avoid filling up memory with identical ASCII name tags), and parametrizations which are mathematical recipes for creating and placing volumes by way of various functions (GENFUNCTIONS, TRANSFUNCTIONS) and Serial Transformers [35].

Aside from the raw geometry already described, each sub-system must also implement a readout geometry which consists of geometrical information required in the digitization and hit making phase of simulation, for example the projective towers in the LAr calorimeter and the η and ϕ positions of calorimeter cells.

In order to run GEANT4 simulation of a detector described in GeoModel, ATLAS developed a tool called Geo2G4 which automatically translates the GeoModel description to GEANT4. Geo2G4 is a simple and reliable tool capable of transferring to GEANT4 the same memory optimization techniques used by GeoModel. An example of how translation of memory optimizations is done from GeoModel to GEANT4 is given by instance sharing [36]. A shared logical volume in the GeoModel tree implies sharing of the corresponding logical volume in GEANT4, while a shared physical volume in the GeoModel tree implies sharing of the corresponding branch in the GEANT4 tree.

A visual debugging tool called V-Atlas [37] was developed from Open Inventor, a 3D visualization toolkit. V-Atlas includes an interactive geometry browser that allows for the investigation of geometry clashes by navigating through volume hierarchy (Fig.5.5 was produced with V-Atlas) and the printing of volume characteristics such as names, dimensions, and masses. When used with simulated data, V-Atlas can also visualize tracks and hits superimposed on the raw geometry.

5.4.2 Volume description

The barrel/end-cap transition region is the transition region located between the two cryostats housing the barrel and end-cap calorimeter. This region can be divided in two sections. The first section runs approximately from $\eta \sim 1.0$ to $\eta \sim 1.8$ along the entire radial depth of the LAr cryostat flange. This section, which contains mostly ID services and a scintillator slab, is about 106 mm deep along the z coordinate (shown in gold in Fig. 5.4). The second section (not shown in Fig. 5.4), extending approximately from $\eta \sim 0.6$ to $\eta \sim 1.0$, is located between the TileCal and the extended TileCal. It is about 640 mm deep along the z coordinate and contains many services such as LAr electronics crates, HVFT filter boxes, ID cables, cooling tubes, etc.

In the most current version of the ATLAS software, the first section is described using two different types of trapezoidal volumes: SectorEnvelopes1 (SE1) and SectorEnvelopes2 (SE2). The two volumes are placed contiguous to each other in the radial coordinate and replicated 16 times (22.5-degree intervals in ϕ), with the help of Serial Transformers, to match the 16 sectors of the ATLAS detector. All 32 individual volumes combine to form a solid ring around the transition region with a rectangular cross-section of about 106 mm x 1617 mm. A third aluminum trapezoid, representing the ID splicing boxes (SPB) and contained in SE2, is placed 4 times (in 90-degree intervals) in each transition region. Section 2 of the transition region is described using 5 different physical volumes (trapezoids and boxes) representing the LAr electronic crates and boards, the pedestals which connect the crates to the cryostat, the BridgeEnvelopes (BE) and BaseEnvelopes (BaseE). The latter two volumes represent the space between LAr crates and tile fingers used to route ID services and other cryogenic tubes. Three 10 mm thick aluminum plates, SectorPlates (SP), BridgePlates (BP) and BasePlates (BaseP) are placed underneath each of the envelopes. These plates protect the cryostat flange and are used as supports for the services. The description is identical for SIDE A (Geneva side) and SIDE C (Jura side) of the ATLAS detector. Figure 5.5 shows the transition region as seen by V-ATLAS.

5.4.3 Material description

Because inactive materials have a direct impact on the physics performance of ATLAS, they must be evaluated very carefully. However, the description of this material or any other part of the ATLAS geometry in GEANT4 is a critical issue for the detector simulation program, since it must represent the right compromise between accuracy and speed. A description of the material as built in the transition region is impossible to realize because of the sheer complexity of the task, but even more important is that such description entails a huge memory consumption and a decrease in speed during simulation. Fig. 5.6 gives an idea of the complexity of the ID service materials in the barrel/end-cap transition region.

Composition

A large variety of materials is used in the transition region. Tubes are made of copper (Cu), stainless steel (SS) and a multilayer (ML) plastic/Al/plastic

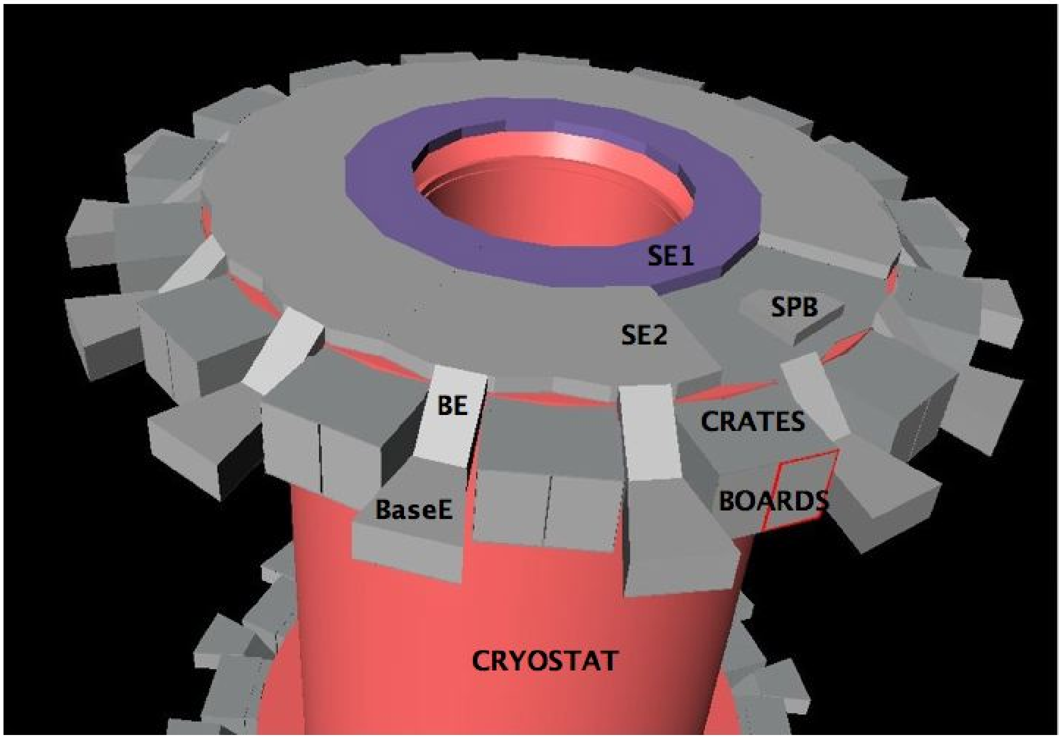

Figure 5.5: Detailed view of the barrel/end-cap transition region showing volumes used to describe various services. Section 1, directly on top of the cryostat is the region covered by SE1 (purple) and SE2, while section 2 covers the flange of the Tile calorimeter (removed for clarity).

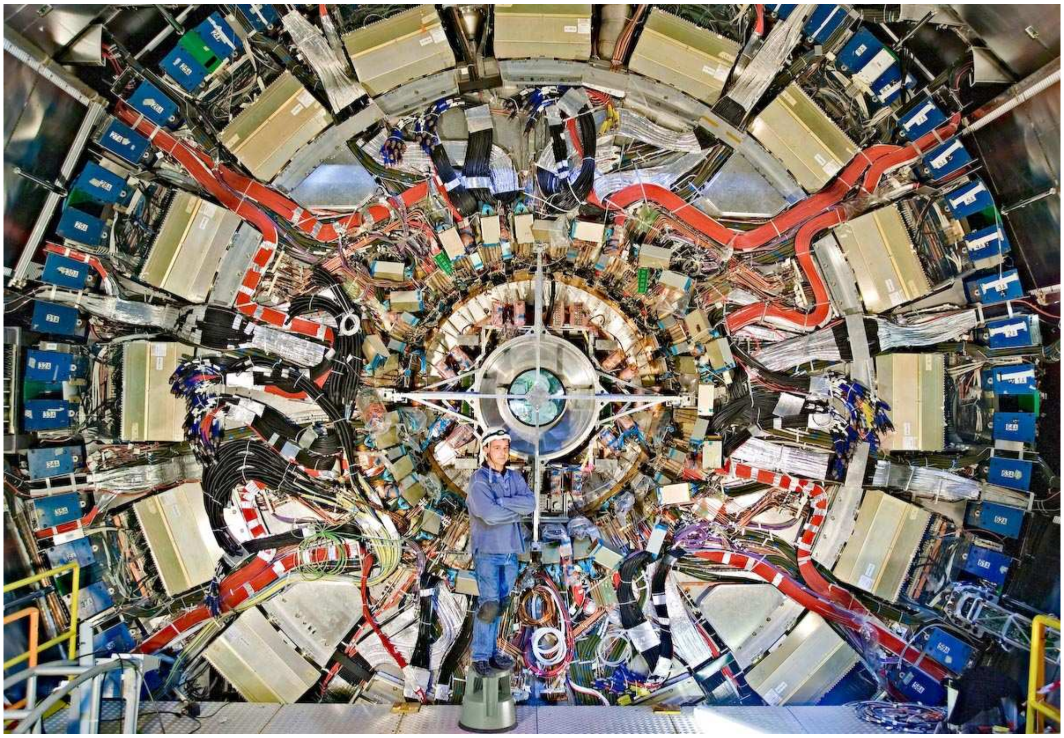

Figure 5.6: This picture of the services in the transition region (SIDE A) highlights the complexity and diversity of the materials to be described. Note the intricacy of the routing of services.

material. The dimensions of the tubes vary greatly, going from an outer-diameter/inner-diameter of 3/2 mm for some Cu tubes to 50/42 mm for ML tubes. In addition to the tubes themselves, one must account for the many gases (N_2 and CO_2) and liquids (C_6F_{14} and C_3F_8) used as coolants, but also as active gas ($XeCO_2O_2$) for the ID subsystems [42]. Table 5.1 provides a summary of the tube materials composition in the barrel/end-cap region in terms of density and total volume.

The material in section 2 of the barrel/end cap transition region is similar to the one in section 1 with the exception of the LAr electronics crates and pedestals. The crates and pedestals are made of Aluminum while the boards and cooling plates are described as a mixed material made of air (.08%), water (7.36%), aluminum (51.09%), and matFEBoards (52%) (itself a mix of epoxy resin (20%), copper (28%) and fiberglass (52%)).

The situation is even more problematic for the cables due to the myriad of cable types and dimensions [43] still being installed on the cryostat flange. Our inventory yielded 24 different types of cables with outer-diameters from 0.81 mm to 11.0 mm. A summary of the amount and volume of cables organized by sub-detector is shown in Table 5.1. Cables are mostly organized in bundles wrapped with a thin protective aluminum shield. Cable connectors are not detailed in the documents already mentioned and, therefore, were not taken into account in our inventory. However, we did account for the sizable number of Cu tubes carrying C_3F_8 to cool the cables. These tubes are laid inside the cable bundles themselves [44]. Although there are many types of cables used for ID services, we have assumed that most cables are made of some sort of copper (nickel plated etc.) conductor and kapton or polyimid insulator. Other materials used in the cables are polyester/aluminum foils for shielding and constantan conductors.

Distribution

Table 5.2 shows how the inventoried tubes and cables are distributed over the cryostat flange as a function of the LAr gaps. The LAr gaps correspond to subdivisions of the cryostat flange into 11.25-degree wedges. Two LAr gaps combine to form what is called a sector of which there are 8 (1, 3, 5, 7, 9, 11, 13, 15). It is clear from the tables that, as part of the optimization procedures taken during the design phase of the experiment, an attempt was made to conserve a certain symmetry in the distribution of services. For example we note an almost identical number of tubes of the same material on both sides of the same gap. This is also true for the cables. Exceptions are gaps 12 and 13 which have SS tubes on only one side (C) compared to most of the other

		SIDE A 665 tubes/pipes	SIDE C 708 tubes/pipes
Material	Density (g/cm^3)	SE1+SE2 (cm^3)	SE1+SE2 (cm^3)
Cu	8.96	13906.3	14271.8
SS	8.00	4751.4	5146.5
ML	1.825	965.6	965.6
C_6F_{14}	1.68	1750.6	2317.9
C_3F_8	1.032	13686.2	14308.4
CO_2	0.001842	5566.3	6993.3
N_2	0.001251	2457.7	852.3
$XeCO_2O_2$	0.004377	2586.6	2662.9
Air	0.001214	56034.9	56944.6

		SIDE A	SIDE C
Detector	Density (g/cm^3)	cables in SE1+SE2 SE1+SE2 (cm^3)	cables in SE1+SE2 SE1+SE2 (cm^3)
PIXEL	2.34	1099 65715.96	1130 66358.22
SCT	2.34	2489 110019.53	2499 110429.17
TRT	2.44	19464 63777.46	19464 63777.46
ID-Global	2.46	89 2896.05	75 2356.32

Table 5.1: Composition of ID tubes and cables by volume in the barrel/end-cap transition region. ID tubes and their content in the barrel/end-cap transition region are shown in the upper half. ML is a multilayer (Plastic/Al/Plastic) tube. The volume of air given here is that included in the ID drain pipes located in gaps 13 A/C and 5C. The large variety of cables does not allow for their individual description here. Cable densities shown are averages of densities of cables per sub-detector.

gaps. Gaps 4 and 5 are the only ones with ML tubes.

Table 5.2: Distribution of ID tubes and cables in the gaps between LAr crates for both side A and side C.

(a) Distribution of tubes and cables in gaps 1 through 8

Material	Sides	**Gaps**							
		1	2	3	4	5	6	7	8
Cu	A	46	52	27	4	6	26	50	56
	C	57	53	26	6	5	26	60	52
SS	A	18	3	6			6	3	19
	C	18	6		8	12		6	18
ML	A					1			
	C				1				
Cables	A	2091	1741	1920	9	28	1913	1740	2148
	C	2105	1744	1913	9	28	1919	1746	2134

(b) Distribution of tubes and cables in gaps 9 through 16

Material	Sides	**Gaps**							
		9	10	11	12	13	14	15	16
Cu	A	46	32	18	38	34	18	34	54
	C	58	38	18	33	45	18	32	55
SS	A	18	3	6			6	3	19
	C	20	6		12	8		6	18
ML	A								
	C								
Cables	A	2092	1545	294	1834	1889	284	1516	2097
	C	2102	1558	287	1831	1898	291	1513	2090

The routing of both cables and tubes is generally done in bundles. In the case of tubes, the bundles are held together by aluminum brackets. The brackets are either soldered or screwed to the various plates (SectorPlates, BridgePlates, and BasePlates). It is impossible to reproduce the exact routing of the services. Also, not all routing maps are available on the ATLAS CDD database and the ones that are available have gone through many modifications.

In light of both the composition and distribution of the services, it was decided to simplify their description by creating a new type of compound material whose density would be a direct reflection of the proportion of its individual components. In doing so one must be extremely careful in estimating the proportion of air in the mixture.

5.4.4 Density calculations

A mixture or compound can be thought of as made of thin layers of pure elements in the right proportion (Bragg additivity) [29]. However, since in our case we are dealing with mixtures of mixtures, the "thin layer" approach may not be feasible. Consequently, in a mixture of materials as is the case of the description of ID services in the transition region, one can approximate the average radiation length by

$$\frac{1}{\mathrm{X}_0} = \sum_j w_j/X_j$$

where w_j and X_i are respectively the fraction by weight and the radiation length of the jth compound. However, because of the difficulty of estimating the correct mass fraction of air in the mixture, we calculate the radiation lengths of the materials using their volume fractions instead. This is an equivalent but more robust approximation since we can evaluate the volume of all services in barrel/end-cap region and assign the remaining volume to the air.

In more practical terms, the density d of the mixture of material is the sum of the products of densities d_j multiplied with the fraction by volume $f_j = V_j/V$ for each member of the mixture. Put otherwise,

$$d = d_1 f_1 + ... + d_n f_n.$$

The lengths of tubes were calculated according to the envelopes they are contained in. Some tubes only span the length of SE1 while others only span that of SE2. However, the majority of tubes span SE1 and SE2. Tubes in SE1 were assigned a length equal to that of SE1 (we did not allow for bending), while tubes in SE2 were assigned a length equal to that of SE2 plus a 5% contingency which accounts for bending and routing. The method used for tubes is also valid for cables except that all cables span our region of interest (SE1 + SE2) and a 10% contingency was added to cables in SE2 due to: Length variation within the same bundle, and possible change of routing along cryostat flange.

For lack of complete information about the cables and in an attempt to simplify the calculations, we used a series of approximations for the density computations. The density of the cables for each sub-detector is obtained by calculating the average densities of cables for which information is available. This method was checked against the average density of SCT cables provided by engineers.

The volume fraction for air was calculated by assigning to the air the remaining volume after all other ID services were subtracted. This calculation was performed separately for SE1 and SE2.

The results of the density calculations are shown in figures 5.7 and 5.8. These results confirm the already mentioned symmetry between side A and side C of the barrel/end-cap transition region. Indeed, If we calculate the average density of the services in SE1 and SE2, and compare both sides, we find it to be respectively 0.87 and 0.33 on side C, 0.86 and 0.33 on side A. We can see that regardless of the side, sector 13 (gaps 12 and 13) and sector 5 (gaps 4 and 5) have the lowest densities. In the current software release, the barrel/end-cap transition region is simulated with 16 different densities for SE1, reflecting the granularity in ϕ. For SE2, densities in sectors 1 and 9 were averaged together, and the same is true for sectors 3, 7, 11 and 15. BE and BaseE are given a uniform density equal to the highest density of the SE1 volumes. This is motivated by the lack of accurate knowledge of the material in those 2 volumes. What is clear is that the densities in both BE and BaseE will be higher since these volumes contain the Cryogenic pipes and other cables and tubes in addition to ID services. Clearly, the description of the ID services must be refined in subsequent releases. In the following section, we show the result of radiation length scans of the transition region done with release 13.0.10.

5.5 Simulation of the barrel/end-cap transition region

For an understanding of the impact of the transition region, one must strictly know the number of radiation lengths seen by a particle as it traverses it. In the ATLAS simulation software, this is accomplished with the use of a GEANT4 construct called Geantino. Geantino "particles" do not interact with matter; they simply carry information about the geometry and material they traverse.

In order to check the validity of our description, we performed a number of radiation length scans with GEANT4. These scans showed that there was

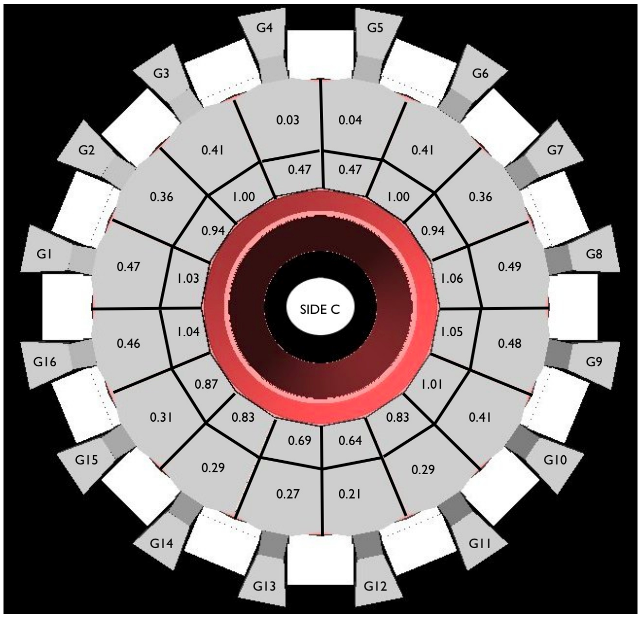

Figure 5.7: Density distribution of the material in the barrel/end-cap transition region as a function of LAr gaps (ϕ) for SIDE C.

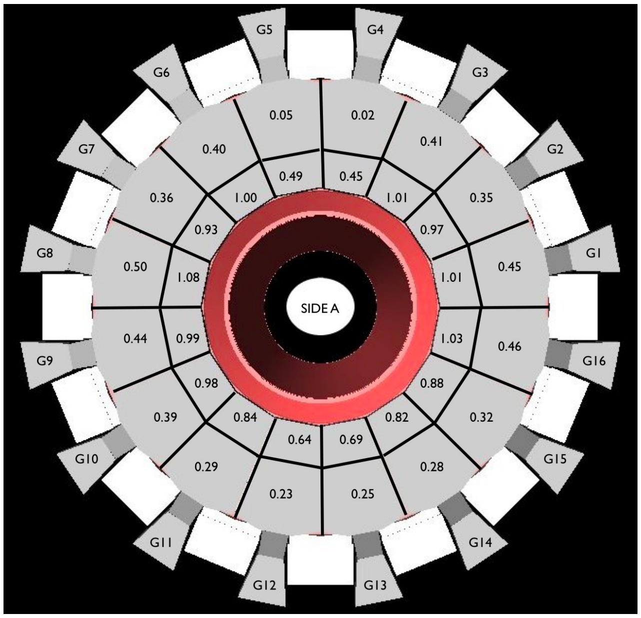

Figure 5.8: Density distribution of the material in the barrel/end-cap transition region as a function of LAr gaps (ϕ) for SIDE A.

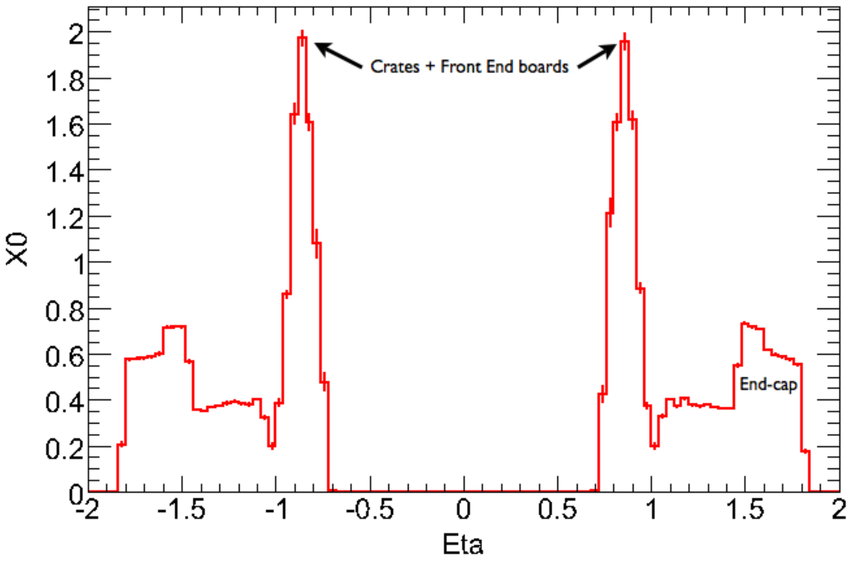

Figure 5.9: Integrated radiation length for only the material in the barrel/end-cap transition region, as a function of η and averaged over ϕ.

indeed a definitive increase in the overall thickness of the LAr calorimeter due to the addition of inactive materials in the barrel/end-cap transition region.

One such scan, shown in Fig. 5.9, concerned the transition region material alone. The integrated radiation lengths, also averaged over ϕ, provides a picture of the various services in the barrel/end-cap transition region. The sharp peak at $\eta \sim 0.8$ is explained by the presence of the pedestals, crates and front end boards ("FEB's"). The peak is followed by a dip around $\eta \sim 1.0$ right at the end of the cryostat. The amount of radiation lengths on the cryostat flange is shown in the range $1.0 \leq \eta \leq 1.85$ with a characteristically higher density in the region nearer to the edge of the cryostat where the cross section available to the services is greatly reduced. A sample result of the scan is given in table 5.3, where SP + SE2 for example means that the geantino particle went successively through SP and then SE2.

5.6 Conclusion

Although Fig. 5.9 indicates a clear increase of the overall thickness of the EM calorimeter in terms of radiation length, this increase does not go beyond the 2 X_0 allowed from the material profile shown in Fig. 5.10[28]. Between $\eta = 1.4$ and $\eta = 1.9$ ID service materials in the barrel/end-cap transition region

Physical volumes	η	X_0	Total X_0
BaseP + BaseE	0.74	0.18 + 0.51	0.69
	0.80	0.17 + 1.02	1.19
Crate + Boards	0.79	0.16 + 0.43	0.59
	0.83	0.16 + 1.62	1.74
	0.92	0.22 + 1.42	1.66
BP + BE	1.01	0.07 + 0.26	0.33
SP + SE2	1.10	0.14 + 0.28	0.42
	1.19	0.14 + 0.36	0.50
	1.37	0.13 + 0.34	0.47
SP + SPB + SE2	1.24	0.13 + 0.08 + 0.04	0.25
SP + SE1	1.60	0.12 + 0.68	0.80
SE1	1.74	0.64	0.64

Table 5.3: Radiation length X_0 as a function of η for some volumes in the transition region. The scan was made with 25 GeV Geantino particles.

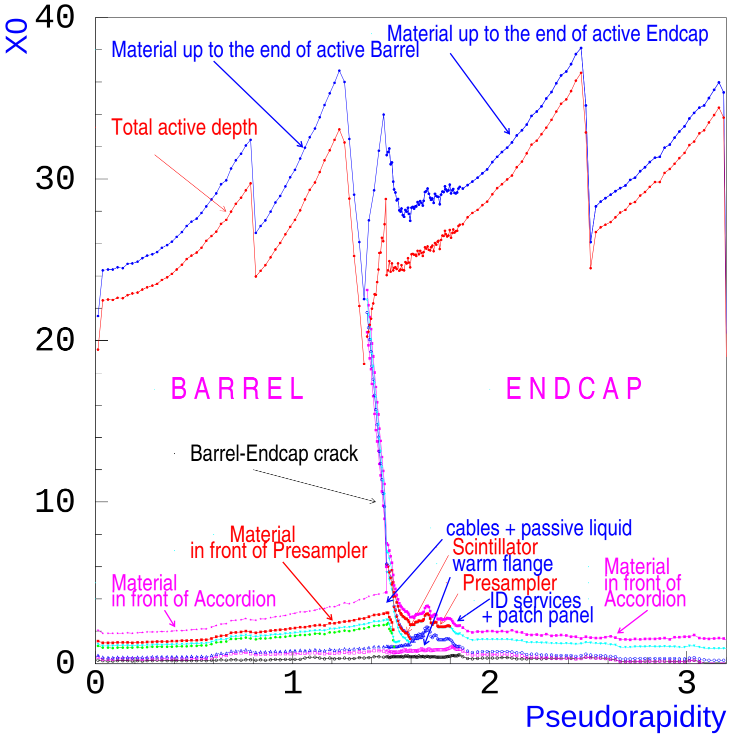

Figure 5.10: Total thickness of the EM Calorimeter as a function of η, showing the contribution of ID services + patch panel.

do not add more than 0.8 X_0 on average in front of the EMEC calorimeter.

The results presented in this report are preliminary in the sense they are based on the most recent EDMS documents (see references) available and on contacts with technicians and engineers. Clearly, it is a work in progress. We did not include many of the services located in the space described as BridgeEnvelopes and BaseEnvelopes, and located between LAr electronic boxes, particularly the huge cryogenic pipes which cut across both the LAr and Tile envelopes. Therefore, we expect the code describing the ID services to go through more revisions.

5.6.1 Acknowledgements

Thank you to all those who have provided me with most of the documents used in this work. To name a few: M. Stodulski, N. Massol, A. Bitadze, S. Malyukov, H. Danielsson, T. Weidberg, S. Gibson, C. Menot, V. Kostyukhin, S. Haywood, etc.

Chapter 6

Photons in the EM barrel during the 2004 Combined Test Beam

6.1 Introduction

Between 17 May 2004 and 15 November 2004 a Combined Test Beam (CTB04) run took place at the CERN H8 beam line. The aim of this exercise was to expose a complete slice of the ATLAS Barrel to the H8 electron test beam. The slice was made of the barrel components of all sub-detectors, the Inner Detector, the Liquid Argon (LAr) and Tile (TileCal) calorimeters, and the muon spectrometer. The ultimate goal of the CTB is to understand the response of the detector as a whole and to develop a pre-commissioning strategy for a quicker startup in the ATLAS cavern.

6.2 The H8 beam-line and its instrumentation

The H8 beam-line sketched in Fig. 6.1 provides both secondary and tertiary electron, pion and muon beams. A 450 GeV proton beam is extracted from the SPS and directed onto the T4 primary target. If the H8 beam runs as a secondary hadron or electron beam in the "filter" mode, a second target is introduced to produce tertiary beams. The beam energy is controlled by three collimators C3, C6, and C9 and ranges from 10 GeV to about 300 GeV. The momentum resolution is given by a set of two collimators, C3 and C9, and is of the order of $\Delta p/p = 0.15$ % at all energies. The electron momentum definition is based on the second momentum analysis using the bending magnets B3 and B4 between C3 acting as source and C9 acting as momentum slit [50].

All magnets used during the CTB are from the same family: The MBP magnets. These include the MBPID used for the ID, the MBPL and MBPS2 used for the muon system, and the MBPL12 used during the photon runs.

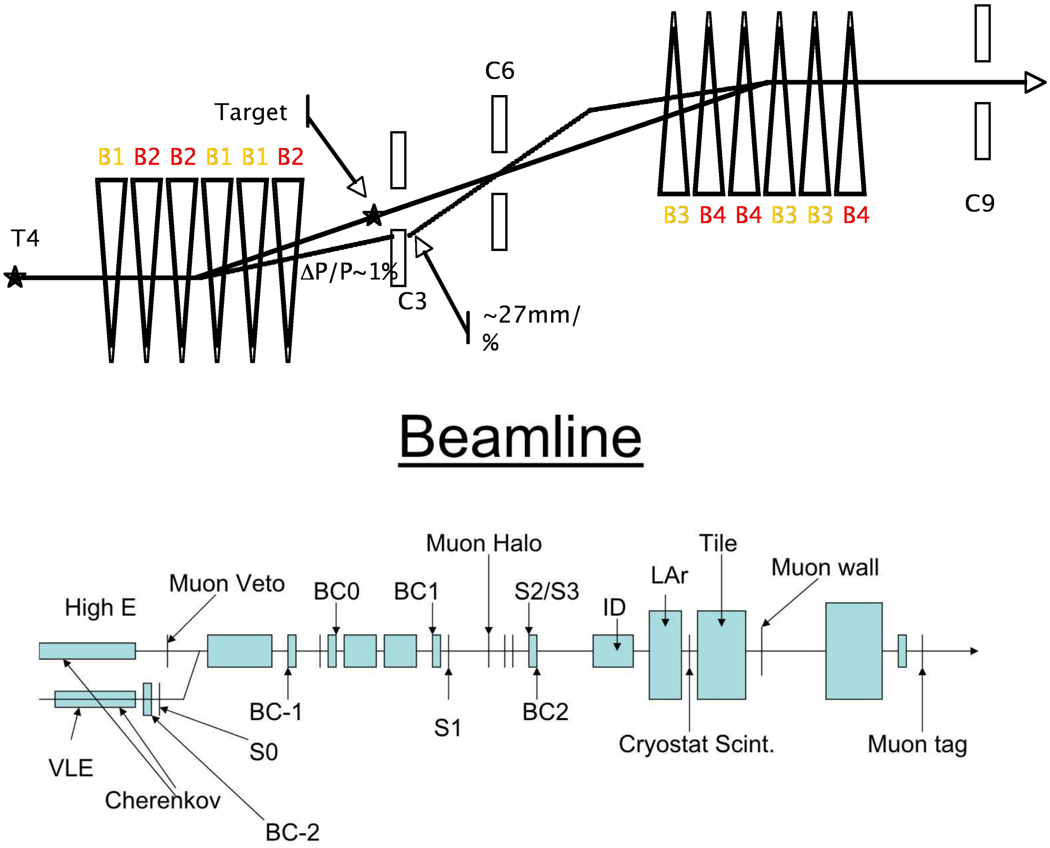

Figure 6.1: Sketch of the H8 beam line showing the momentum definition elements, collimators (C3, C6, C9) and magnets (B1,B3, etc) (above). Other elements of the beam: Scintillators (S1, S2, etc), Cerenkov counters, beam chambers (BC0, BC1, etc), and other detectors are shown below.

Other auxillary detectors used during the CTB include the Cerenkov counters used to discriminate pions from electrons, beam chambers (BC-2 to BC2 in Fig. 6.1) used to verify beam profile and various scintillators used for trigger (S2, S3) and for the removal of muons. Muon Veto ($h \times w \times t = 81 \times 34 \times 2$ cm^3) was used to tag high-energy muons during low energy runs. Muon Halo ($h \times w \times t = 30 \times 32 \times 1.5$ cm^3) was used veto muons outside the beam axis. It has a hole of 3.4 cm centered on the beam axis. Muon Tag ($h \times w \times t = 40 \times 40 \times 2$ cm^3), located behind the first beam dump was used as either a muon trigger or a muon tag [49].

The ATLAS CTB reference system is defined to be as consistent as possible with the ATLAS reference system [48], with its x-axis along the H8 beam, its y-axis vertical and pointing towards the sky, and its z-axis horizontal and pointing towards Geneva in the south. The origin (0,0,0) of the reference system lies at the front surface of the Inner Detector magnet (MBPS) which contained both Pixel and SCT in its enclosure.

6.3 Detector modules

Detailed descriptions of the ATLAS sub-detectors have already been given in chapter 2 of this thesis. Therefore we will only briefly describe here specificities of the 2004 CTB setup.

6.3.1 Inner Detector modules

The Inner Detector shown in Fig. 6.2 consists of 3 sub-detectors: The Pixel, the SCT and TRT modules. The Pixel detector consists of 6 modules, 2 for the Pixel B layer and 2 each for Pixel layers 1 and 2. The active size of each of these modules is $z \times y = 60.8 \times 16.4$ mm^2.

The SCT setup consists of 4 layers with 2 modules per layer. Each SCT module covers an area of $z \times y = 120 \times 60$ mm^2 with an overlap of 4 mm between 2 modules in the same layer.

The TRT module was made of 2 barrel wedges, each equivalent to 1/16 of a cylinder with inner radius 558 mm, outer radius 1080 mm, and length 1425.5 mm. Because of its large size, the TRT module was always kept outside of the MBPS magnet .

There was a number of run configurations. Some of these configurations involved additional material being introduced between the different sub-detectors, Pixel and SCT being moved in and out of the MBPS enclosure, TRT being rotated around the z-axis, or simply the absence of one or two of the sub-

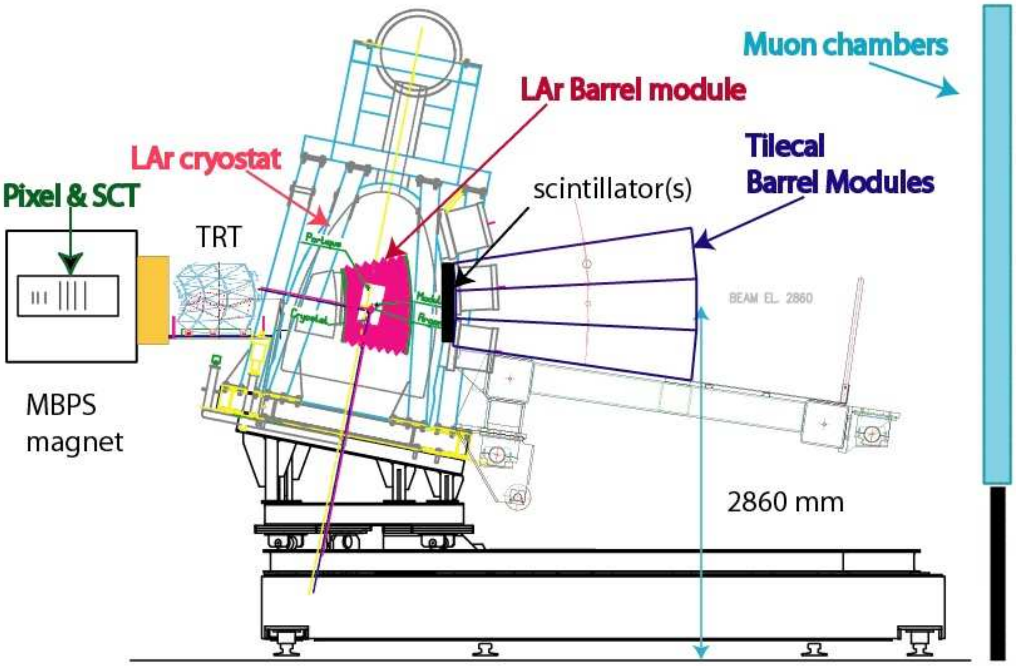

Figure 6.2: Schematic of the test beam table setup. Particles incident from left go successively through Pixel, SCT, TRT, the Calorimeters and finally the Muon modules.

detectors. It wasn't until early October 2004 that all ID sub-detectors were present all at once for the combined runs. The additional material introduced for some run configurations include aluminum slabs (10 and 20 mm thick) placed between SCT and Pixel or SCT and TRT, and a copper foil placed upstream of the Pixel.

6.3.2 Muon chambers

The muon chambers start at 12587 mm from the interaction point (origin of the reference system). However, the muon setup comprises a muon wall made of 12 scintillators and located downstream of the LAr-TileCal but sitting on the same table. The rest of the muon chambers are separated from the muon wall by a massive beam dump designed to stop all particles except muons. Muons passing the beam dump were identified by muon tag (Fig. 6.1).

6.3.3 Calorimeter modules

The LAr module and TileCal modules (also shown in Fig. 6.2) with a total mass of 82 tons are placed on a common table that can rotate around the y-axis and translate along the z-axis in such a way that it allows for the simulation of specific impact points in η. Because of the impossibility to incline the table further, magnetic deflections of the beam were used to simulate impact points in ϕ.

The EM barrel calorimeter was represented by a prototype module also called M0 placed inside a massive LAr cryostat (center of picture in Fig. 6.3). In an attempt to limit the amount of argon liquid seen by incident particles, an "argon-excluder" made of Rohacell (a rigid and very low density foam) was placed inside the cryostat and in front of the module. Three Tile Calorimeter modules including two production modules were used. The TileCal modules are stacked on top of each other and placed on the arm of the table after the LAr cryostat. A small space is left between the two calorimeters where scintillators could be placed depending on the run configurations.

6.4 The Photon Beam

The Photon Beam setup for Run 2102857, used for our analysis, is shown in Fig. 6.4. The photons are produced when an initial 180 GeV/c positron beam goes through a converter made of a 0.2 mm thick slab of lead (Pb). The converter thickness of 0.2 mm was chosen because studies showed it to provide the best chance of producing clean single photons [55]. Both the photons and the remaining positrons after bremsstrahlung traverse a magnet (MBPL12) that provides vertical (ϕ) as well as horizontal (η) deviations. The horizontal deviation insures that the photon trajectory was cleared of both electrons and positrons. However, the magnetic field was tuned such that the positron although deviated would still hit the calorimeter away from the photon.

A proper reconstruction of the photon and positron clusters in the calorimeter required they be separated by at least three cells in its "Middle" sampling. A scintillator ("snew" in Fig. 6.4) was used to trigger events for which the initial positron produced a photon. In case photons get converted in the ID material, a second magnet (MBPS) insured that the resulting e^+e^- pair is separated vertically before hitting the calorimeter at two distinct impact points in ϕ.

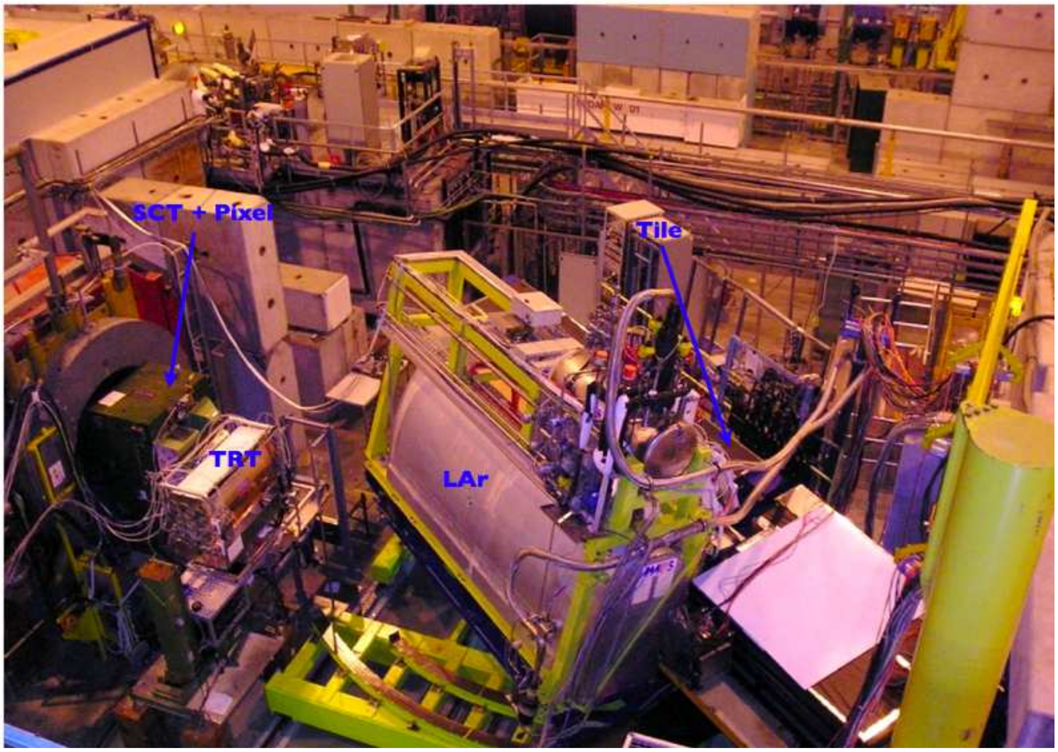

Figure 6.3: The H8 test beam area. The LAr barrel cryostat is seen in the center of the picture.

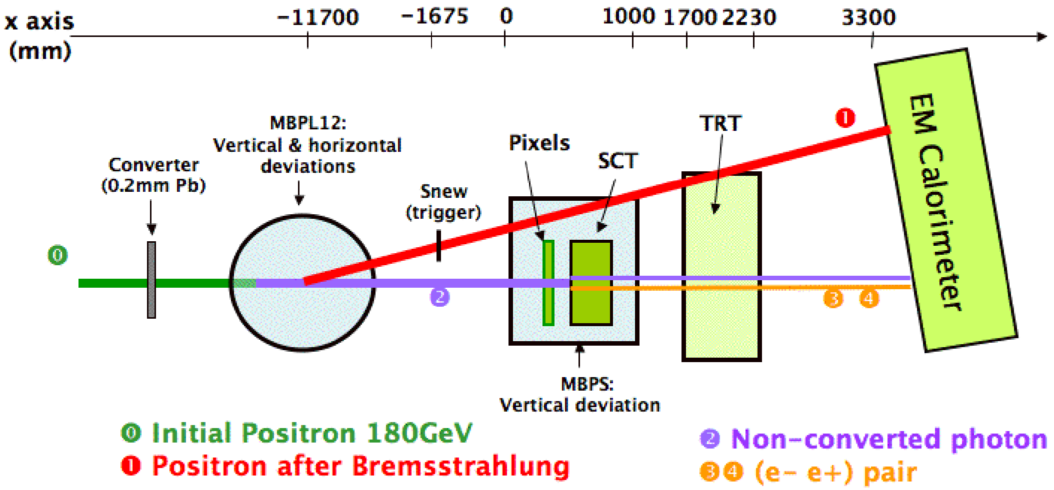

Figure 6.4: Schematic of the Photon beam configuration. Photons incident from the converter continue towards the ID material (Pixel, SCT, TRT) where they are converted. The e^+e^- pair produced is then vertically separated by a magnet (MBPS) before entering the calorimeter.

6.4.1 Calculation of the positron beam energy

Although the nominal positron beam energy for run 2102857 was known to be 180 GeV, the final momentum was lower like for all other H8 runs. The positron momentum definition is based on the second momentum analysis using the bending power of magnets B3 and B4 between collimators C3 and C9 (as shown in Fig. 6.1). However, the B4 magnets were degaussed and kept unpowered [50]. Therefore the beam momentum P was solely proportional to the bending power of B3 alone and can be expressed as:

$$P(GeV/c) = 0.3 \times \frac{\int B_3 dl}{\Delta\theta} \tag{6.1}$$

where $\Delta\theta = 41$ mrad is the total angular deviation of the beam between C3 and C9, and $\int B_3 dl = 24.1095$ Tm the bending power of the magnet [50][52].

Uncertainty from the geometry of the spectrometer was reduced by keeping the opening slits for both C3 and C9 fixed at 8 mm during data taking. The induced momentum spread was therefore $\pm 0.15\%$ at all energies [50]. The Energy loss due to synchrotron radiation is estimated to about 0.7698 GeV with a maximum induced uncertainty of 15 MeV. Other contributions to the error in the beam energy include the remnant fields in B3 and B4, which add

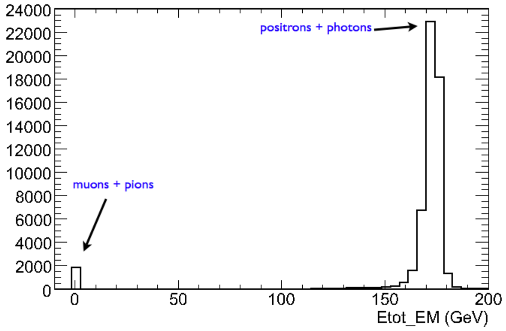

Figure 6.5: Energy distribution in EMB calorimeter M0 before cuts.

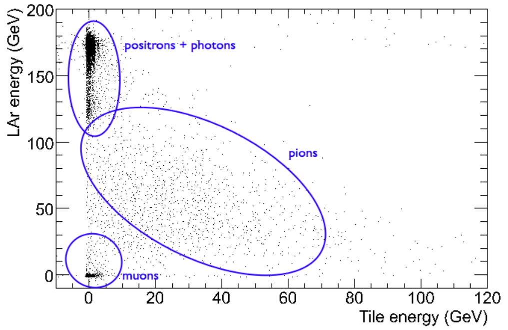

Figure 6.6: Correlation plot of LAr and Tile energies.

a systematic uncertainty of about 240 MeV, and the magnet current, which add about 0.05%. The error in the absolute energy is of the order of 0.5%. Putting all these numbers together we obtain a beam energy of 176.29 ± 1.23 GeV.

6.4.2 Event Selection

Run 2102857 was reconstructed with release 12.0.6 + “LAr groupArea” of the ATLAS offline software. The “LAr groupArea” is constituted by the most recent software packages specific to the LAr detectors. Four our analysis, we reconstructed all 56000 events of the run with the requirement that up to 5 electromagnetic clusters per event can be present in the calorimeter. This requirement is motivated by the fact that although we are solely interested in the non-converted photons along with the positrons that produced them, there might be many events with more than two clusters. It was expected that a 180 GeV positron would produce a photon of about 50 GeV during bremsstrahlung. Therefore, only the two highest energy clusters were recorded. Energy was reconstructed on 3×3 clusters using the optimal filtering coefficient (OFC) method. This method [53] uses computed noise autocorrelation from pedestal data and the normalized ionization pulse (predicted from calibration and including correction for distortion caused by electrical properties of cells) to minimize the electronics noise contribution and pile-up.

A proper analysis of the data required prior removal of various undesirable particles such as muons, pions, single positrons, and single photons as well as e^+e^- pairs resulting from photon conversions. Such e^+e^- pairs were readily removed by applying a cut that requires zero tracks in the ID. Fig. 6.5 shows the energy distributions of these particles in the EM barrel calorimeter prior to the cleaning of the beam.

Muons and pions contamination

The usual methods of removing muons by applying cuts based on the number of scintillator counts for both Muon Tag and Muon Halo [54][55] did not work very well. This suggests that at least some of the muons must have had an off-axis trajectory that made them miss Muon Halo and Muon Tag. The correlation plot between the energies in the EM barrel calorimeter and in the Tile calorimeter (Fig. 6.6) provided an efficient mean of removing muons and pions by requiring that both LAr and Tile energies be above 5 GeV.

$\mathbf{e}^+, \gamma$ position dispersion

The beam not being point-like and the amount of material in front of the calorimeter not being uniform, there exists a natural smearing of the position of the photon mainly observed in the strips [55][56]. This smearing engenders a low energy tail that must be removed. Since the photon position smearing is correlated to that of the positron, a cut on the η position of the first one should the same desirable effect on the second as well. In general, very tight η and ϕ cuts were applied to match the position of both particles in the data and the MC. As shown in Fig. 6.7, this cut only retained photons within the range $0.533 < \eta_{strips} < 0.545$. Fig. 6.8 shows that we have a good match in η and ϕ after cuts. The correlation plots (Fig. 6.9) of the energy deposit in the Strips and Middle compartment for both particles provided an additional mean of reducing the low energy tail.

6.4.3 Data Monte Carlo comparison

The simulation of both the beam-line and the EMB module was performed with GEANT4 (Fig. 6.10 shows the setup as viewed by GEANT4). A description of the different steps of a full simulation of the ATLAS detector using GEANT4 has already been given in chapter 5. Therefore this section will only address specificities related to the CTB04 runs.

The description of the beam-line and LAr module presented each its own set of challenges. It is indeed crucial to know the exact amount of passive material in front of the LAr calorimeter in order to accurately simulate particle showers. In terms of radiation length, the beam instrumentation before the cryostat contributes $0.2X_0$ while the two aluminum walls of the cryostat, the “argon-excluder” and the LAr between the presampler and first sampling all

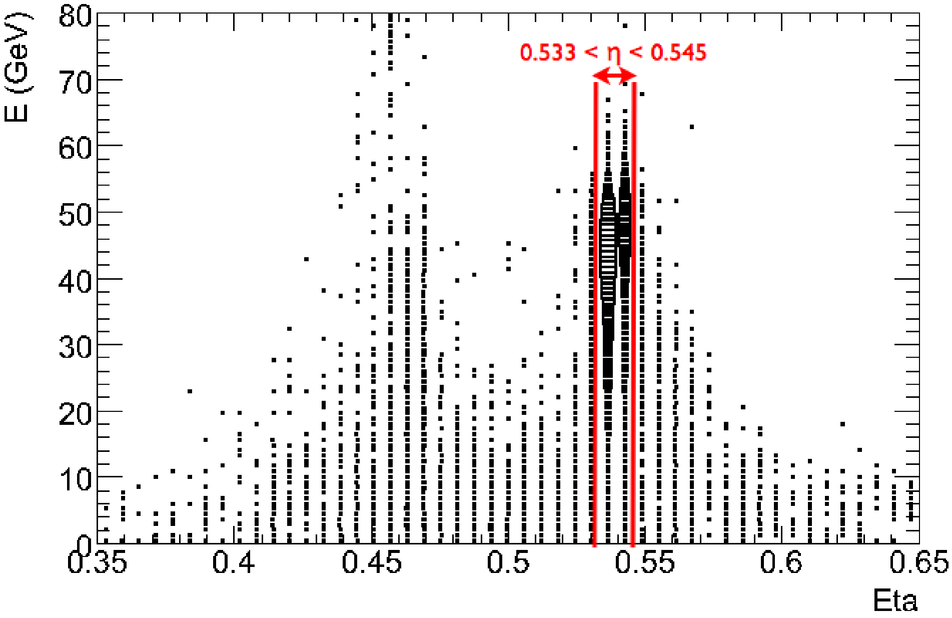

Figure 6.7: Plot of Energy vs Eta of the photon in the strips shows the beam always hitting in a narrow Eta range between 0.533 and 0.545.

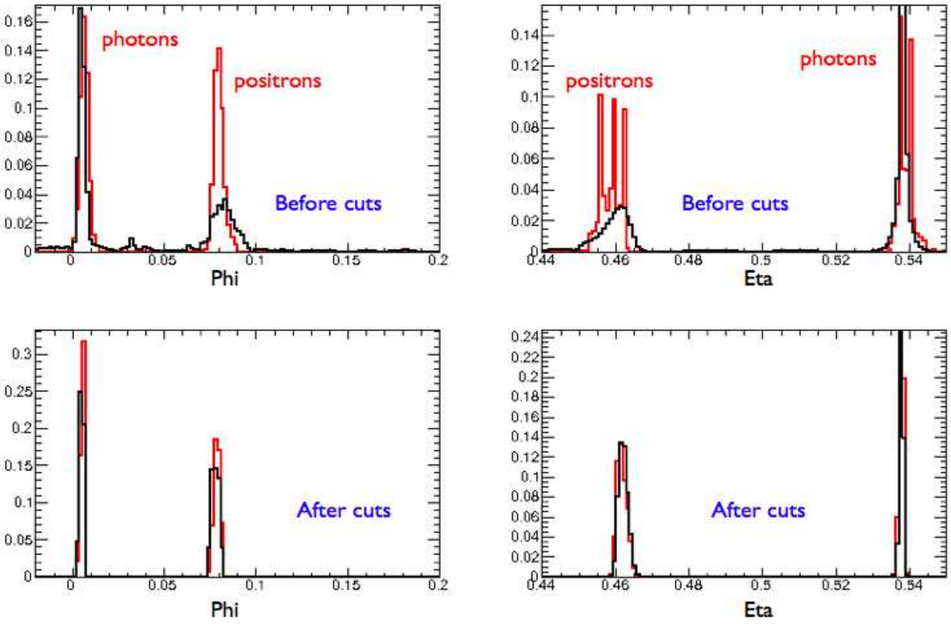

Figure 6.8: Distribution of photons and positrons in Eta and Phi, before and after cuts were applied for a better match.

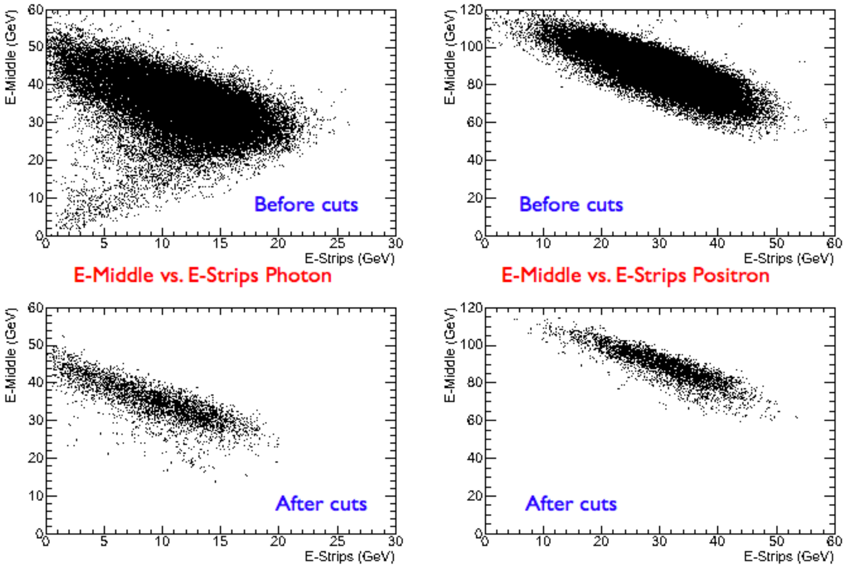

Figure 6.9: The e^+ plots (right) cleaned up with the 5 GeV cut applied to Tile and LAr, while the photon plots (left) cleaned up by requiring $\mathrm{E}_\gamma\mathrm{Strips} + \mathrm{E}_\gamma\mathrm{Middle} > 15$ GeV Upper plots are before clean up and lower plots are after clean up.

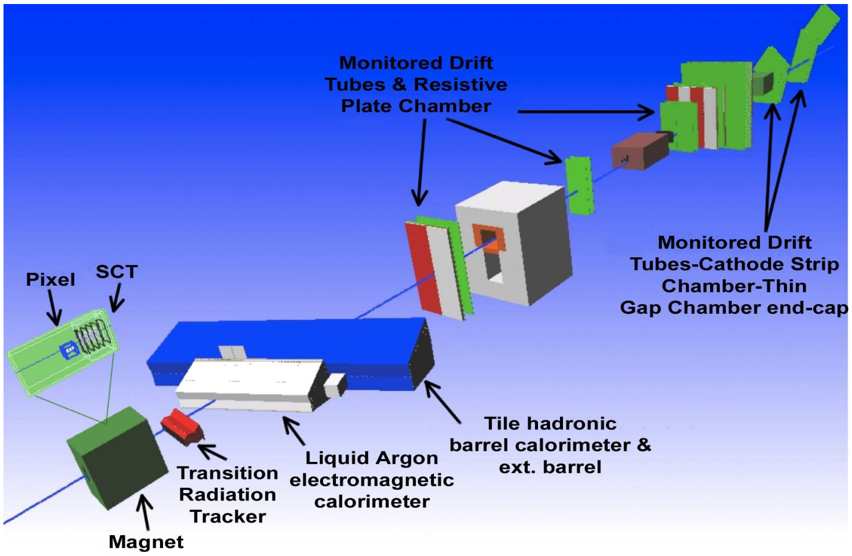

Figure 6.10: Schematic outline of the various sub-detectors on the H8 beamline as viewed by Geant4.

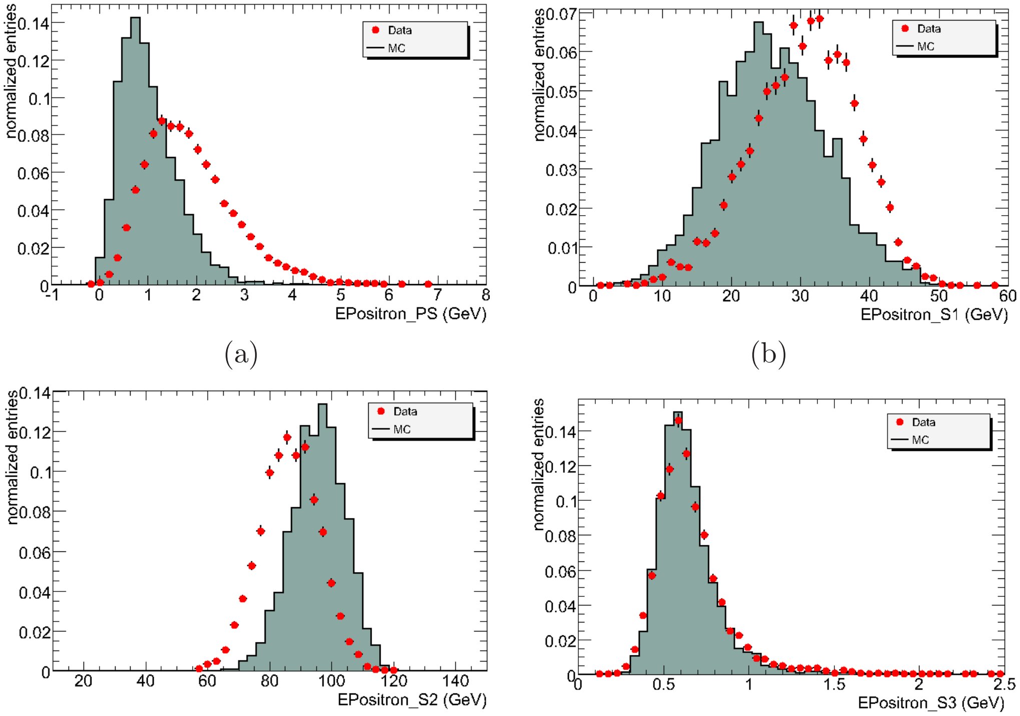

(a) (b)

(c) (d)

Figure 6.11: Energy deposited in the EMB samplings by a 120 GeV positron .

contribute about $1.5X_0$. What is not known exactly is the amount of LAr between the presampler and the cryostat walls although an estimate of 2 ± 0.5 cm has been obtained through simulation.

The reconstruction of the positron and photon in the EM calorimeter technically consists in summing the energies deposited in the cells contained in a given cluster. However, not all the energy of a particle is contained in the cluster. Energy is lost in the dead material in front of the EM calorimeter and when the particles shower extend into the Tile calorimeter. Typically, a 3×3 cluster only contains about 95% of the shower energy. The cross-talk between neighboring cells in the Strips and Middle layers, resulting in an overestimation of the physics signal in the data was corrected using the OFC method.

6.5 Conclusion

Fig. 6.11, 6.12, 6.13 show an obvious mismatch of Data and MC for the positron, despite recent efforts to improve the MC description and simulation

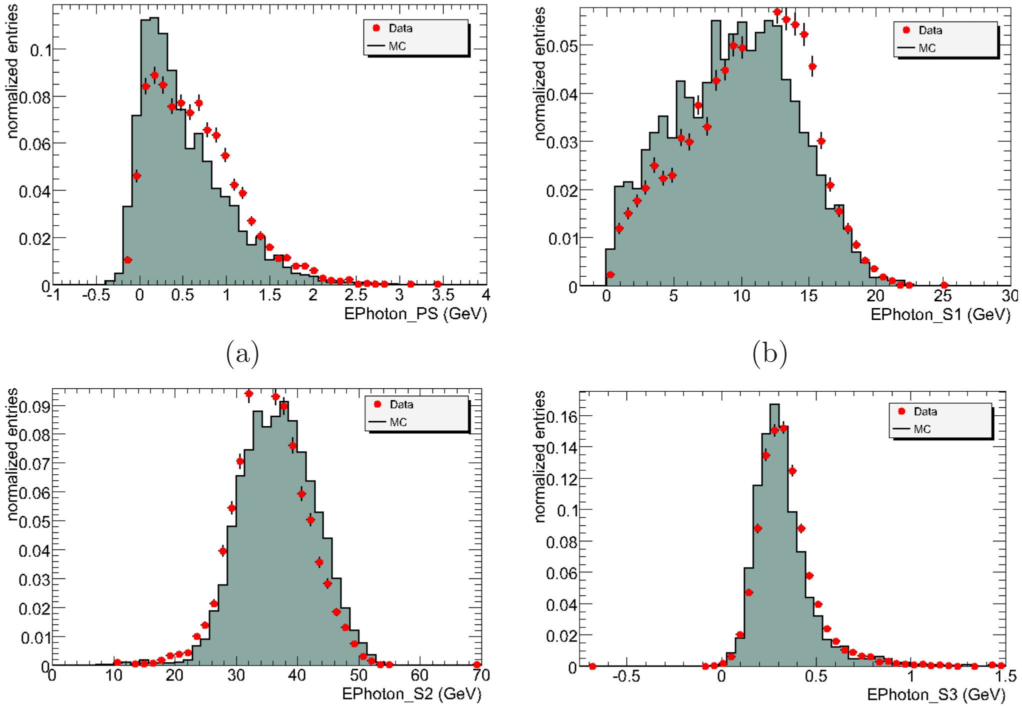

(a) (b)

(c) (d)

Figure 6.12: Energy deposited in the EMB samplings by a 50 GeV photon .

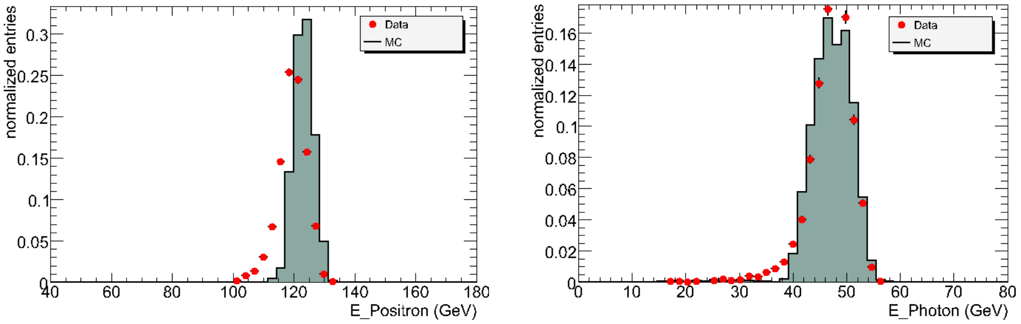

(a) (b)

Figure 6.13: Total Positron cluster energy (a), Total Photon cluster energy (b).

of the H8 setup. Its is likely that material present on the beamline during data taking was not included in the simulation. Furthermore it is also feared that the positron scraped the top of the ID magnet and the top of the TRT detector on its way to the EM calorimeter module. Finally it is also possible that material other than the argon excluder was present in the cryostat. Some discrepancy between data and MC has already been identified in another photon run study and solved by tuning the MC to match the data [55]. Some of the adjustable correction factors used in the above cited study include:

- Because the electric field was only simulated to cover 11 mm of the 13 mm argon-filled gap of the presampler, the presampler energy should be rescaled by a factor proportional to 11/13.
- The Energy scale of the beam is known to about 1% or ($\sim$ 2 GeV). This uncertainly affects solely the photon. Therefore, the photon energy scale should be adjusted accordingly.
- Finally the MC versus Data comparison for the total energy may be off by up to 3 to 4 % due to LAr temperature effects.

Bibliography

[1] ATLAS Collaboration
The Large Hadron Collider Technical Design Report.
CERN/AC/95-05, CERN, 1995.

[2] P. Higgs. Phys. Lett., **12**:132, 1964.

[3] L. Carminati
SEARCH FOR A STANDARD MODEL HIGGS BOSON
IN THE $H \rightarrow \gamma\gamma$ *CHANNEL WITH THE ATLAS DETECTOR.*
Acta Physica Polonica B, Vol. 38 (2003).

[4] ALICE Collaboration
ALICE Technical Proposal.
CERN/LHCC/95-71, 1995.

[5] CMS Collaboration
CMS Technical Proposal.
CERN/LHCC/94-43, 1994.

[6] LHCb Collaboration
LHCb Technical Proposal.
CERN/LHCC/98-04, 1998.

[7] ATLAS Collaboration
ATLAS Technical Proposal.
CERN/LHCC/94-43, 1994.

[8] ATLAS Collaboration
Detector and Physics Performance Technical Design Report.
CERN/LHCC/99-14/15, 1999.

[9] ATLAS Collaboration
The ATLAS Experiment at the CERN Large Hadron Collider.
submitted to JINST, December 2007.

[10] ATLAS Collaboration
Inner Detector Technical Design Report.
CERN/LHCC/97-16, 1997.

[11] ATLAS Collaboration
Muon Spectrometer Technical Design Report.
CERN/LHCC/97-22, 1997.

[12] *The RPC LV1 Trigger System of the Muon Spectrometer of the ATLAS Experiment at LHC.*
IEEE Transactions On Nuclear Science, Vol.51, No. 4, 08/2004.

[13] *HLT/Trigger jets*
http://indico.cern.ch/contributionDisplay.py?contribId=18&sessionId=3&confId=26943
4th ATLAS Hadronic Calibration Workshop, Tucson, Arizona, March 2008

[14] B. Aubert *et al*
Construction, assembly and tests of the ATLAS electromagnetic barrel calorimeter
CERN-PH-EP/2005-034, 2005.

[15] ATLAS Collaboration
The ATLAS experiment at the CERN Large Hadron Collider
CERN-PH-EP/2005-034, 2005.

[16] C. W. Fabjan and F. Gianotti
Calorimetry for particle physics
Reviews of Modern Physics, Vol 75, Oct. 2003.

[17] D. Axen *et al.*
Signal feedthroughs for the ATLAS barrel and endcap calorimeters
Rev. Sci. Instrum. **76** (2005) 063306.

[18] T. Carli *et al*
Energy Linearity and Resolution of the ATLAS Electromagnetic Barrel Calorimeter and Electron Test-Beam
Nucl. Instr. Methods **A** 568 (2006) 601-623.

[19] B. Botchev *et al.*, 2007 *JINST* **2** T10002

[20] ATLAS Collaboration
ATLAS Technical Proposal for a General-Purpose pp Experiment at the

Large Hadron Collider at CERN
CERN/LHCC/94-43, 15 Dec 1994.

[21] RD3 Collaboration
1991 Nucl. Instr. Methods **A** 309 438; *ibid.* 1992 **A** 321 467

[22] ATLAS Collaboration
ATLAS Liquid Argon Calorimeter Technical Design Report
CERN/LHCC 96-41, 15 Dec 1996.

[23] Perkins J.R.
HV wiring and Connector Systems
Chapter 6 of *Handbook of Wiring, Cabling and Interconnecting for Electronics*
Charles E. Harper editor, McGraw-Hill, 1972.

[24] ASTM
Standard Test Method for Detection and Measurement of Partial Discharge (Corona) Pulses in Evaluation of Insulation Systems
ASTM D1868-93, 1998

[25] Druyvesteyn M.J. and Penning F.M.
1940 *Rev. Mod. Phys.* **12** 88

[26] Penning F.M. and Addink C.C.
1934 *Physica* **1** 1007

[27] The GEANT4 Collaboration (S. Agostinelli *et al*)
GEANT4 - *A Simulation Toolkit*
Nucl. Instr. Methods, NIM **A** 506 (2003), 250-303.

[28] ATLAS Collaboration
ATLAS Calorimeter Performance Technical Design Report
CERN/LHCC/1996-40, January 1997.

[29] W-M Yao *et al*
PASSAGE OF PARTICLES THROUGH MATTER
2006 *J. Phys. G: Nucl. Part. Phys.* **3**3 1

[30] R.K.Bock *et al*
The Particle Detector Briefbook
http://rd11.web.cern.ch/RD11/rkb/titleD.html, 1999.

[31] ATLAS Collaboration
ATLAS Detector and Physics Performance Technical Design Report
CERN/LHCC-1999-14 and CERN/LHCC-1999-15, June 1999.

[32] ATLAS Collaboration
AthenaFramework
https://twiki.cern.ch/twiki/bin/view/Atlas/AthenaFramework

[33] T. Sjostrand *et al.*
PYTHIA
http://home.thep.lu.se/ torbjorn/Pythia.html

[34] G. Corcella, I.G. Knowles, G. Marchesini, S. Moretti, K. Odagiri, P. Richardson, M.H. Seymour and B.R. Webber
HERWIG 6.5
JHEP 0101 (2001) 010 [hep-ph/0011363]; hep-ph/0210213

[35] J. Boudreau
GEOMETRY KERNEL CLASSES
http://atlas.web.cern.ch/Atlas/GROUPS/DATABASE/detector_description, 2003.

[36] J. Boudreau and V. Tsulaia
THE GEOMODEL TOOLKIT FOR DETECTOR DESCRIPTION
Proceedings of the Conference on Computing in High Energy and Nuclear Physics
(CHEP2004), Interlaken, Switzerland, Sept. 2004.

[37] J. Boudreau *et al*
The V-Atlas Event Visualization Program
Proceedings of the Conference on Computing in High Energy and Nuclear Physics
(CHEP 2006), TIFR Mumbai, India, Feb. 2006.

[38] ATLAS Collaboration
ATLAS Computing Technical Design Report
CERN/LHCC-2005-022, July 2005.

[39] E. Barberio *et al*
The Geant4-Based Atlas Fast Electronmagnetic Shower Simulation
ATL-SOFT-CONF-2007-002; ATL-SOFT-CONF-2007-014.-Geneva: CERN, 2007.

[40] ATLAS Collaboration
Evaporative Cooling Piping
EDMS: https://edms.cern.ch/file/545589/1/Evaporative_cooling_system.v4(18.05.05).xls,
ATL-IC-EP-0025 v.4, January 2005.

[41] ATLAS Collaboration
Monophase Cooling System Pipework, EDMS: https://edms.cern.ch/file/545592/1/Monophase_Cooling_System_Pipework(24.01.05).xls
ATL-IC-EP-0028 v.2, January 2005.

[42] ATLAS Collaboration
Tube assemblies for installation on calorimeter up to z=0
EDMS: https://edms.cern.ch/cedar/plsql/doc.info?cookie=6764557&document_id=571053&ve
ATL-IC-EP-0030 v.1, October 2006.

[43] ATLAS Collaboration
ID global service inventory
EDMS: https://edms.cern.ch/cedar/plsql/doc.info?cookie=6764557&document_id=382001&ve
ATL-IC-EP-0033 v.1, September 2006.

[44] ATLAS Collaboration,
List of cables and cable cooling tubes per sector routed over the cryostat flange and then along the tile barrel outer surface (In Work)
EDMS: https://edms.cern.ch/cedar/plsql/doc.info?cookie=6764557&document_id=685481&ve
ATL-IC-EP-0033 v.1, September 2006.

[45] ATLAS Collaboration
Inner Detector Services Integration-Along Cryostat Flange
EDMS: https://edms.cern.ch/cdd/plsql/c4w.save_subject_code?cookie=1111182&p_subject_co
ATLICSIF0244, October 2006.

[46] ATLAS Collaboration
Inner Detector Services Integration-Along Cryostat Flange
EDMS: https://edms.cern.ch/cdd/plsql/c4w.save_subject_code?cookie=1111182&p_subject_co
ATLICSIF0290, October 2006.

[47] ATLAS Collaboration
ATLAS Inner Detector Services, Parameters describing the orientation naming and layout of Inner Detector Services
ATL-IC-EP-0017, December 2005.

[48] ATLAS Collaboration
ATLAS Barrel Combined Run in 2004, Test Beam Setup and its evolutions
EDMS Note: ATC-TT-IN-0001, EDMS ID: 406980, Feb. 2005.

[49] ATLAS Collaboration
Beamline instrumentation in the 2004 Combined ATLAS testbeam.
ATL-TECH-PUB-2005-001; ATL-COM-TECH-2005-001.- Geneva : CERN, 2005.

[50] M. Aharrouche *et al*
Energy Linearity and Resolution of the ATLAS Electromagnetic Barrel Calorimeter in an Electron Test-Beam
Nucl. Instrum. Meth. A 568 (2006) 601-623

[51] I. Efthymiopoulos
Measurement of the Beam Energy in the 2004 TB.
http://indico.cern.ch/contributionDisplay.py?contribId=s1t4&confId=a05895, 2005

[52] I. Efthymiopoulos
Evaluation of the bending power of the MBN spectrometer magnets of H8.
CERN SL/EA/IE Internal Note, Geneva, Switzerland, March 2002.

[53] W.E. Cleland and E.G. Stern
Signal processing considerations for liquid ionization calorimeters in a high rate environment
Nucl. Instrum. Meth. A 338 (1994) 467-497.

[54] H. Hakobyan *et al*
Selection of electron events from Testbeam 2004 data for H8 setup
http://indico.cern.ch/conferenceDisplay.py?confId=a05895

[55] K. F. Loureiro
Measuring the Photon Energy Scale Through Test Beam Data.
PhD thesis, CERN-THESIS-2006-040

[56] S. Viret
Atlas Electromagnetic barrel photon testbeam response compared to GEANT4
ATLAS Internal Note, 2004.